

8-1-2017

Instrumentation and Measurement of Thermoelectric and Structural Properties of Binary Chalcogenides and Half-Heusler Alloys at Extreme Conditions Using a Paris-Edinburgh Press

Jason Lee Baker

University of Nevada, Las Vegas, bakerj@physics.unlv.edu

Follow this and additional works at: <https://digitalscholarship.unlv.edu/thesesdissertations>

 Part of the [Condensed Matter Physics Commons](#)

Repository Citation

Baker, Jason Lee, "Instrumentation and Measurement of Thermoelectric and Structural Properties of Binary Chalcogenides and Half-Heusler Alloys at Extreme Conditions Using a Paris-Edinburgh Press" (2017). *UNLV Theses, Dissertations, Professional Papers, and Capstones*. 3070.

<https://digitalscholarship.unlv.edu/thesesdissertations/3070>

This Dissertation is brought to you for free and open access by Digital Scholarship@UNLV. It has been accepted for inclusion in UNLV Theses, Dissertations, Professional Papers, and Capstones by an authorized administrator of Digital Scholarship@UNLV. For more information, please contact digitalscholarship@unlv.edu.

INSTRUMENTATION AND MEASUREMENT OF THERMOELECTRIC AND
STRUCTURAL PROPERTIES OF BINARY CHALCOGENIDES AND HALF-HEUSLER
ALLOYS AT EXTREME CONDITIONS USING A PARIS-EDINBURGH PRESS

By

Jason Lee Baker

Bachelor of Science – Physics
University of Nevada, Las Vegas
2003

Master of Science – Physics
University of Nevada, Las Vegas
2012

A dissertation submitted in partial fulfillment
of the requirement for the

Doctor of Philosophy – Physics

Department of Physics and Astronomy
College of Sciences
The Graduate College

University of Nevada, Las Vegas
August 2017



Dissertation Approval

The Graduate College
The University of Nevada, Las Vegas

July 25, 2017

This dissertation prepared by

Jason Lee Baker

entitled

Instrumentation and Measurement of Thermoelectric and Structural Properties of Binary Chalcogenides and Half-Heusler Alloys at Extreme Conditions Using a Paris-Edinburgh Press

is approved in partial fulfillment of the requirements for the degree of

Doctor of Philosophy – Physics
Department of Physics and Astronomy

Andrew Cornelius, Ph.D.
Examination Committee Co-Chair

Kathryn Hausbeck Korgan, Ph.D.
Graduate College Interim Dean

Ravhi Kumar, Ph.D.
Examination Committee Co-Chair

Changyong Park, Ph.D.
Examination Committee Member

Michael Pravica, Ph.D.
Examination Committee Member

Rama Venkat, Ph.D.
Graduate College Faculty Representative

Abstract

Understanding the high-pressure behavior of transport properties has been a driving force in the study of materials under extreme conditions for well over a century being pioneered by P.W. Bridgman in the early 20th century. Research dedicated to the study of these properties leads to a variety of important applications: exploration of insulator to semi-conductor to metal, structural, and electronic phase transitions, correlation of pressure-induced structural phase transitions and the electronic properties along phase boundaries, identifying electronic topological transitions, testing the validity of theoretical models and providing input parameters for calculations at high-pressure and high-temperature conditions, exploration of sample synthesis and behavior of electronic structure at extreme conditions, understanding the effects of chemical pressure when compared to chemical substitution, among a slew of other applications. This work's main goal was the design and development of a specialized sample cell assembly for use with a Paris-Edinburgh press capable of performing high-pressure and high-temperature (HPHT) electrical resistance, Seebeck coefficient, thermal conductivity measurements alongside energy-dispersive X-ray diffraction and X-ray radiography imaging up to 6 GPa and 500°C to fully characterize the electrical, thermal, and structural properties of materials simultaneously at extreme conditions. This system has been installed at Argonne National Laboratory at the Advanced Photon Source at the Sector 16 BM-B beamline of the High-Pressure Collaborative Access Team and is now available to general users as a measurement technique. The results for pure elemental bismuth and the classical thermoelectric material PbTe are presented to demonstrate the capabilities of the system. With this system, we have also measured the electrical, thermal, and structural properties of SnTe and Mn-doped SnTe thermoelectric materials and the half-Heusler compounds TiNiSn and TiCoSb.

Acknowledgements

I would like to acknowledge the aid and support of the following people:

1. My co-advisors Dr. Ravhi Kumar and Dr. Andrew Cornelius for taking a chance on me as an undergraduate student almost 10 years ago and allowing me to remain as a graduate student pursuing a Master's degree and PhD. The assistance, advice, knowledge, and patience has allowed me to complete my dissertation and become a scientist.
2. Dr. Changyong Park for both his willingness to serve as a member of my dissertation committee, and the countless hours spent aiding me with experiments at the beam-line with trouble-shooting and brainstorming ideas. Also, I greatly appreciate always lending an ear and providing technical and scientific advice without hesitation.
3. Curtis Kenney-Benson for the many, many discussions, technical advice, hours of aid with experiments and equipment set-up. I am forever grateful for always machining any cell parts that were required for completing experiments and his incredible patience.
4. My committee members Dr. Michael Pravica and Dr. Rama Venkat for their time taken out of their busy schedules to attend committee meetings and providing advice.
5. My wife, Nicole Arellano-Baker, for her incredible patience and understanding with the ups and downs of this pursuit, dedication to ensuring I strive to always push forward, and the endless times of listening to descriptions of experiments, presentations, posters, scientific papers, etc. And most of all, thank you for believing in me.
6. All faculty/staff of the Department of Physics and Astronomy at UNLV and HiPSEC faculty/staff, graduate and undergraduate students both new and old.
7. My family and friends for always supporting my endeavors and being amazing people.

Table of Contents

Abstract	iii
Acknowledgements	iv
Table of Contents	v
List of Tables	xi
List of Figures	xii
Chapter I – Introduction & Background	1
Overview	1
Optimizing Electrical Transport	4
Reduction of the Thermal Conductivity	6
Pressure as Tool to Study Transport Properties	8
Dissertation Contents and Organization	10
Chapter II – Experimental Details & Techniques	12
Overview	12
High-Pressure Thermoelectric Apparatus	12
Paris – Edinburgh Press	12
Thermoelectric Cell Assembly: Description of Cell Assembly	14
Thermoelectric Cell Assembly: Assembly Process	18
High-Pressure Thermoelectric Measurements	22
Radiography Imaging: Sample Thickness Measurements	22

High-Pressure Electrical Resistance/Resistivity Measurements	23
High-Pressure Seebeck Coefficient Measurements	24
High-Pressure Thermal Conductivity Measurements	25
High-Pressure Dimensionless Figure of Merit, ZT Measurements	27
Pressure Determination: Paris-Edinburgh Press	27
Raw High-Pressure Thermoelectric Data	28
High-Pressure Angle-Dispersive X-ray Diffraction Measurements	29
Diamond Anvil Cell	29
Pressure Determination: Ruby Fluorescence	30
Powder X-ray Diffraction and Bragg's Law	31
High-Pressure Powder X-ray Diffraction Measurements	32
Equation of State	33
Chapter III – Sample Results: Bismuth	35
Overview	35
High-Pressure Thermoelectric Measurements	36
Radiography Sample Thickness Measurements	36
Isobaric Seebeck Coefficient Measurements	36
High-Pressure Electrical Resistance Measurements	38
High-Pressure Isothermal Seebeck Coefficient Measurements	39
High-Pressure Thermal Conductivity Measurements	40

High-Pressure Dimensionless Figure of Merit	40
Conclusions.....	41
Chapter IV – Sample Results: PbTe	42
Overview.....	42
High-Pressure Thermoelectric Measurements.....	43
Isobaric Seebeck Coefficient of PbTe.....	43
High-Pressure Electrical Resistivity Measurements	43
High-Pressure Seebeck Coefficient Measurements	44
High-Pressure Thermal Conductivity Measurements	45
High-Pressure Dimensionless Figure of Merit, ZT.....	45
Conclusions.....	46
Chapter V – Sample Results: SnTe.....	47
Overview.....	47
Sample Synthesis	48
High-Pressure Thermoelectric Measurements.....	49
Energy-Dispersive X-ray Diffraction	49
Radiography Sample Thickness Measurements	50
High-Pressure Electrical Resistivity Measurements	50
High-Pressure Seebeck Coefficient Measurements	52
High-Pressure Thermal Conductivity Measurements.....	52

High-Pressure Dimensionless Figure of Merit, ZT.....	53
Conclusions.....	54
Chapter VI – Sample Results: $\text{Sn}_{1-x}\text{Mn}_x\text{Te}$ ($x = 12\%$).....	55
Overview.....	55
Sample Synthesis	55
High-Pressure Structural Measurements.....	56
High-Pressure Powder X-ray Diffraction	56
Equation of State Analysis.....	58
High-Pressure Thermoelectric Measurements	59
Radiography Sample Thickness Measurements	59
High-Pressure Electrical Resistivity Measurements	60
High-Pressure Seebeck Coefficient Measurements	60
High-Pressure Thermal Conductivity Measurements	61
High-Pressure Dimensionless Figure of Merit, ZT.....	62
Conclusions.....	62
Chapter VII – Sample Results: TiCoSb	64
Overview.....	64
Ambient Crystal Structure	66
Sample Synthesis	66
High-Pressure Structural Measurements.....	67

High-Pressure Powder X-ray Diffraction	67
Equation of State Analysis.....	68
High-Pressure Thermoelectric Measurements	69
Radiography Sample Thickness Measurements	69
High-Pressure Electrical Resistivity Measurements	70
High-Pressure Seebeck Coefficient Measurements	70
High-Pressure Thermal Conductivity Measurements	71
High-Pressure Dimensionless Figure of Merit, ZT.....	71
Conclusions.....	72
Chapter VIII – Sample Results: TiNiSn	73
Overview.....	73
Ambient Crystal Structure	75
Sample Synthesis	75
High-Pressure Structural Measurements.....	76
High-Pressure Powder X-ray Diffraction	76
Equation of State Analysis.....	78
High-Pressure Thermoelectric Measurements	79
Radiography Sample Thickness Measurements	79
High-Pressure Electrical Resistivity Measurements	79
High-Pressure Seebeck Coefficient Measurements	80

High-Pressure Thermal Conductivity Measurements	80
High-Pressure Dimensionless Figure of Merit, ZT.....	81
Conclusions.....	82
Chapter IX – Conclusions.....	83
Appendix A – Figures.....	91
Appendix B – Tables ..	174
References	182
Curriculum Vitae	194

List of Tables

Table 1. PbTe – Raw Thermoelectric Data.....	174
Table 2. PbTe – Calculated Thermoelectric Data.....	175
Table 3. $\text{Sn}_{1-x}\text{Mn}_x\text{Te}$ ($x = 12\%$) – Unit Cell Parameters, Volume, and Pressure Data	176
Table 4. $\text{Sn}_{1-x}\text{Mn}_x\text{Te}$ ($x = 12\%$) – 2 nd -order BM-EOS Fit Parameters	177
Table 5. TiCoSb – Unit Cell Parameters, Volume, and Pressure Data.....	178
Table 6. TiCoSb – 3 rd -order BM-EOS Fit Parameters.....	179
Table 7. TiNiSn – Unit Cell Parameters, Volume, and Pressure Data	180
Table 8. TiNiSn – 3 rd -order BM-EOS Fit Parameters	181

List of Figures

Figure 1. ZT vs. Time 1950 – 2000	91
Figure 2. ZT vs Time: 2000 – Present	92
Figure 3. Paris-Edinburgh Photograph	93
Figure 4. Thermoelectric Cell Assembly Schematic	94
Figure 5. Cell Assembly Step #2	95
Figure 6. Cell Assembly Step #3	96
Figure 7. Cell Assembly Step #4	97
Figure 8. Cell Assembly Step #5	98
Figure 9. Cell Assembly Step #6	99
Figure 10. Cell Assembly Step #7	100
Figure 11. Cell Assembly Step #8	101
Figure 12. Cell Assembly Step #9	102
Figure 13. Cell Assembly Step #10	103
Figure 14. Cell Assembly Step #11	104
Figure 15. Cell Assembly Step #12	105
Figure 16. Cell Assembly Step #14	106
Figure 17. Example Radiography Image	107
Figure 18. Example Intensity Profile	108
Figure 19. Electrical Resistivity Set-Up Schematic.....	109
Figure 20. Seebeck Coefficient Set-Up Schematic.....	110
Figure 21. Thermal Conductivity Set-Up Schematic.....	111
Figure 22. Princeton symmetric type diamond anvil cell [81].....	112

Figure 23. Diamond Anvil Cell Schematic.....	113
Figure 24. Example Ruby Fluorescence Spectrum.....	114
Figure 25. Bragg's law. [87].....	115
Figure 26. Example Powder XRD	116
Figure 27. XRD Spectra Example	117
Figure 28. Bi – Phase Diagram.	118
Figure 29. Bi – Radiography Images	119
Figure 30. Bi – Sample Thickness vs Pressure	120
Figure 31. Bi – Seebeck Coefficient vs Temperature	121
Figure 32. Bi – Normalized Electrical Resistance vs Pressure	122
Figure 33. Bi – Seebeck Coefficient vs Pressure	123
Figure 34. Bi – Normalized Thermal Conductivity vs Pressure	124
Figure 35. Bi – Normalized ZT vs Pressure	125
Figure 36. PbTe – P-T Pathways	126
Figure 37. PbTe – Thermoelectric EMF vs Temperature	127
Figure 38. PbTe – Seebeck Coefficient vs Temperature	128
Figure 39. PbTe – Normalized Electrical Resistivity vs Pressure	129
Figure 40. PbTe – Seebeck Coefficient vs Pressure	130
Figure 41. PbTe – Normalized Thermal Conductivity vs Pressure	131
Figure 42. PbTe – Normalized ZT vs Pressure.....	132
Figure 43. SnTe – Ambient XRD Spectrum.....	133
Figure 44. SnTe – EDXRD Spectra vs Pressure.....	134
Figure 45. SnTe – Radiography Image	135

Figure 46. SnTe – Sample Thickness vs Pressure	136
Figure 47. SnTe – Normalized Electrical Resistance vs Pressure	137
Figure 48. SnTe – Seebeck Coefficient vs Pressure	138
Figure 49. SnTe – Normalized Thermal Conductivity vs Pressure	139
Figure 50. SnTe – Normalized ZT vs Pressure.....	140
Figure 51. $\text{Sn}_{1-x}\text{Mn}_x\text{Te}$ ($x = 12\%$) – Ambient XRD Spectrum	141
Figure 52. $\text{Sn}_{1-x}\text{Mn}_x\text{Te}$ ($x = 12\%$) – XRD Spectra vs Pressure	142
Figure 53. $\text{Sn}_{1-x}\text{Mn}_x\text{Te}$ ($x = 12\%$) – Lattice Parameters vs Pressure.....	143
Figure 54. $\text{Sn}_{1-x}\text{Mn}_x\text{Te}$ ($x = 12\%$) – Unit Cell Volume vs Pressure	144
Figure 55. $\text{Sn}_{1-x}\text{Mn}_x\text{Te}$ ($x = 12\%$) – Radiography Images.....	145
Figure 56. $\text{Sn}_{1-x}\text{Mn}_x\text{Te}$ ($x = 12\%$) – Sample Thickness vs Pressure.....	146
Figure 57. $\text{Sn}_{1-x}\text{Mn}_x\text{Te}$ ($x = 12\%$) – Normalized Electrical Resistivity vs Pressure	147
Figure 58. $\text{Sn}_{1-x}\text{Mn}_x\text{Te}$ ($x = 12\%$) – Seebeck Coefficient vs Pressure	148
Figure 59. $\text{Sn}_{1-x}\text{Mn}_x\text{Te}$ ($x = 12\%$) – Normalized Thermal Conductivity vs Pressure.....	149
Figure 60. $\text{Sn}_{1-x}\text{Mn}_x\text{Te}$ ($x = 12\%$) – Normalized ZT vs Pressure	150
Figure 61. TiCoSb – Ambient Crystal Structure	151
Figure 62. TiCoSb – Ambient XRD Spectrum.....	152
Figure 63. TiCoSb – XRD Spectra vs Pressure	153
Figure 64. TiCoSb – Lattice Parameter vs Pressure	154
Figure 65. TiCoSb – Unit Cell Volume vs Pressure.....	155
Figure 66. TiCoSb – Radiography Images	156
Figure 67. TiCoSb – Sample Thickness vs Pressure	157
Figure 68. TiCoSb – Normalized Electrical Resistivity vs Pressure	158

Figure 69. TiCoSb – Seebeck Coefficient vs Pressure	159
Figure 70. TiCoSb – Normalized Thermal Conductivity vs Pressure	160
Figure 71. TiCoSb – Normalized ZT vs Pressure.....	161
Figure 72. TiNiSn – Ambient Crystal Structure	162
Figure 73. TiNiSn – Ambient XRD Spectrum.....	163
Figure 74. TiNiSn – XRD Spectra vs Pressure.....	164
Figure 75. TiNiSn – XRD Spectra vs Pressure: High-Pressure Phase	165
Figure 76. TiNiSn – Lattice Parameter vs Pressure.....	166
Figure 77. TiNiSn – Unit Cell Volume vs Pressure.....	167
Figure 78. TiNiSn – Radiography Images	168
Figure 79. TiNiSn – Sample Thickness vs Pressure	169
Figure 80. TiNiSn – Normalized Electrical Resistivity vs Pressure	170
Figure 81. TiNiSn – Seebeck Coefficient vs Pressure.....	171
Figure 82. TiNiSn – Normalized Thermal Conductivity vs Pressure	172
Figure 83. TiNiSn – Normalized ZT vs Pressure	173

Chapter I – Introduction & Background

Overview

The effects of thermoelectricity were first observed in the early 19th century when Thomas Johann Seebeck reported an observation in 1821 of the deflection of a compass needle occurring within the vicinity of a closed loop formed of two dissimilar conductors when a heat gradient was applied [1]. Seebeck explained this behavior as a magnetic phenomenon relating the Earth's magnetism to the temperature difference, which was erroneous. This effect is instead governed by the movement of charge carriers within these dissimilar metals due to the temperature difference creating a voltage difference. Despite his erroneous explanation of the observed phenomenon, Seebeck measured this property for a vast array of materials. Another 12 years later in 1834, a related phenomenon was discovered by Jean Charles Athanase Peltier when he observed temperature gradients being produced in the vicinity of a junction of dissimilar metals when a current was passed [2]. Both of these effects hold potential for clean and renewable sources of energy conversion, but even though their discovery was almost two centuries ago, large-scale application of their potential is very limited due to a lack of conversion efficiency.

Since the demand for power consumption world-wide is continually increasing, it is imperative to find clean and renewable sources of fuel. Much research has been dedicated to identifying new cleaner energy sources which encompass fuels such as nuclear, solar, wind, and geo-thermal [3]. An additional problem all energy sources encounter is the inevitable loss of some amount of energy as wasted heat through exhaust gasses, heat conduction, convection and radiation as well as other means [3]. It is estimated that industrial processes lose between 20 -

50% of potential output energy as reported by the Department of Energy [3]. Thus, it is important not only to explore alternative energy sources, but additionally, it is significant to identify means to convert lost waste heat into useable electrical energy. Thermoelectricity is one such means to convert waste heat into electrical energy directly via solid-state means. Through the use of thermoelectric materials, thermoelectric devices are developed with no moving parts that can either convert heat into electricity via the Seebeck effect or use electricity to transfer heat from low temperature to high temperature or high temperature to low temperature via the Peltier and Thompson effects. Applications of such devices range from the development and use of radioisotope thermoelectric generators (RTGs) on NASA missions such as Cassini and various satellites and some terrestrial RTGs [4], commercial refrigeration, to potential uses in the automobile industry [5]. However, the promise of large-scale applications for these materials has not come to fruition due to issues with their generally low efficiency and technical challenges [6].

Thus, it becomes important to understand how thermoelectric efficiency behaves in a variety of conditions. The efficiency of thermoelectric materials can be described by a dimensionless figure of merit ZT , as defined in **Equation 1**.

$$ZT = \frac{\alpha^2 \sigma}{\kappa} T \quad \text{Equation 1}$$

where α is the Seebeck coefficient, σ is the electrical conductivity, κ is the thermal conductivity, and T is the temperature of the material in measurement or application conditions. Materials with larger ZT values are considered more efficient at the conversion of waste heat into useable energy. Upon examination of **Equation 1**, it is easily observed that an ideal thermoelectric material would have a large Seebeck coefficient and electrical conductivity and a small thermal

conductivity. Ideally, it should then be simple to fine-tune these three parameters to obtain an efficient thermoelectric material, but the complicated interdependence of all three parameters significantly increases the difficulty in producing an efficient material. For example, changes to the doping concentration of a semiconductor is a means to optimize **ZT**; however, while an increase to the doping concentration can lead to an increase in the electrical conductivity this can also decrease the Seebeck coefficient and increase the thermal conductivity [6 – 11]. Additionally, an example of the complex relationships of these parameters is described by the Wiedemann-Franz Law, which is a relation between the electronic contribution to the thermal conductivity, the electrical conductivity, and the temperature. This relation states that the ratio of the electrical conductivity and the electronic contribution to the thermal conductivity is proportional to the temperature, leading of increase in the thermal conductivity when the electrical conductivity increases [12].

Figure 1 is a plot of the **ZT** value of various thermoelectric materials from the 1950s to 2000 adapted from Heremans *et al* [11]. Throughout the early years of thermoelectric materials in the 1950s and 1960s, very few highly efficient thermoelectric materials were uncovered and the overall **ZT** value remained below 1, which is typically the lowest cutoff value for application purposes. MnTe, ZnSb, and PbTe were discovered during this time period and yielded a maximum **ZT** value of 0.5. With more dedicated research in the 1970s, a few materials were discovered with **ZT** values drifting above 1, specifically Bi₂Te₃ in applications for Peltier cooling. Between the 1970s and the 1990s there was very little enhancement to the thermoelectric efficiency as it remained fairly stable near a maximum **ZT** of 1.0 [11]. A separate depiction of the last two decades of thermoelectric efficiency as a function of time is displayed in **Figure 2** adapted from Zhang *et al* [7]. Approximately two decades ago, another resurgence in

thermoelectric research began to take shape as several methods to enhance **ZT** emerged such as modifying the band structure [13,14], band convergence [15,16], quantum confinement effects and electron energy barrier filtering to increase the Seebeck coefficient [17,18], nanostructuring and hierarchical architecturing to reduce thermal conductivity [19,20] among a variety of other techniques [20-24]. These methods have lead to the large increase in **ZT** noticed over the last two decades as researchers have continued to explore these techniques.

Optimizing Electrical Transport

As discussed in the previous section, one very significant method of increasing the efficiency of thermoelectric materials is through optimization of its electronic properties. The Seebeck coefficient and the electrical resistivity combine as the numerator of **Equation 1** to make the power factor ($\alpha^2\sigma$) which governs the electrical transport properties of a thermoelectric material. In general, the power factor can be optimized by modifying carrier concentration through chemical doping and alloying possibly leading to an increased Seebeck coefficient and a decreased electrical resistivity and thus an increased electrical conductivity [7-11,13-21].

Some of the first approaches to enhance the power factor and thus the overall electrical transport of thermoelectric materials focused on the quantum confinement effect which was proposed by Hicks and Dresselhaus [17,18]. This is an effect that occurs in low-dimensional materials due to an asymmetric density of states (DOS) near the Femi level (E_F). If E_F is located at an ideal position a high power factor is expected, yet it is difficult to experimentally produce these materials due to the very small size structures required. However, thermoelectric efficiency enhancement has been observed in some materials including PbTe/Pb_{1-x}Eu_xTe and SrTi_{0.8}Ni_{0.2}O₃ due to quantum confinement effects [25,26]. The observations by Hicks and Dresselhaus were

the ones with the large factors that lead to the resurgence in thermoelectric research in the 1990's and the marked increase in **ZT** values in the late 1990's and throughout the 2000's are **Figure 1** and **Figure 2** depict.

Another approach to optimizing the electrical transport properties of thermoelectric materials through increasing the power factor is to identify and explore novel band structures through chemical alloying and doping to influence band degeneracy and effective mass. For example, the thermoelectric efficiency of PbTe can be enhanced through doping with Na due to a lighter hole effective mass and the **ZT** value of $\text{PbTe}_{1-x}\text{Se}_x$ can be increased by influencing the band structure of the material [14]. Another example of influencing the band structure of materials to enhance their thermoelectric properties is through resonant doping in Tl-doped PbTe, In-doped SnTe, as well as others [13,14,27]. Additionally, direct enhancement of the Seebeck coefficient has been observed by tuning energy offsets between light and heavy bands in PbTe [7]. Specifically, Mn and Mg alloyed PbTe, lead to an enhancement of the Seebeck coefficient through influencing band structure [28,29]. These enhancements have lead to very high **ZT** values for alloyed PbTe of 1.6 at 700 K [29] and 2.0 at 873 K [28].

Furthermore, interfacial engineering may also be used to enhance the power factor through increased carrier mobility. An accumulation of charge carriers confined to a 2D or 1D space charge regime is formed and potentially leads to an enhancement of the power factor. Examples of this engineering technique being applied to thermoelectric materials include the use of Ge-Si core-shell nanowires used hole gas confined between un-doped Ge and doped Si to increase the mobility [30].

Reduction of the Thermal Conductivity

Thermal conductivity plays a large role in the thermoelectric efficiency due to the need for a large temperature difference across a material to produce a useable voltage via the Seebeck effect. Thus a reduction of the thermal conductivity is extremely important to optimizing **ZT** values of thermoelectric materials. Thermal conductivity can be described as a combination of the electronic contribution and the lattice contribution given by:

$$\kappa = \kappa_{lat} + \kappa_{el} \quad \text{Equation 2}$$

where κ_{lat} represents the lattice contribution to the thermal conductivity and κ_{el} represents the electronic contribution to the thermal conductivity. One of the largest issues with reducing the thermal conductivity is the strong correlation between κ_{el} and the electrical conductivity through charge carriers. The Wiedemann-Franz Law, as mentioned briefly earlier, quantifies this relationship and is given by:

$$\frac{\kappa_{el}}{\sigma} = LT \quad \text{Equation 3}$$

where κ_{el} and σ represent the electronic contribution to the thermal conductivity and electrical conductivity as previously defined. **L** represents a proportionality constant called the Lorentz number which has a theoretical value of $2.44 \times 10^{-8} \text{ W } \Omega \text{ K}^{-2}$. This empirical law discovered in 1853 describes a proportional relationship between the thermal conductivity and the electrical conductivity where the ratio of κ and σ is the same value for different metals [12]. Thus due to this strong correlation, methods to reduce thermal conductivity focus on reducing the κ_{lat} due to its independence on carrier concentration unlike κ_{el} .

κ_{lat} can be defined as

–

Equation 4

where C_v represents the heat capacity at constant volume, v represents the phonon velocity and l represents the mean free path (MFP). Methods to reduce κ_{lat} include the introduction of point defects through doping and alloying and when these defects are of similar dimension of the MFP of the phonons, scattering can occur. Specifically the reduction effect of point defects can be described in terms of the Callaway model [31] which accounts for mass differences and interatomic coupling force differences between the impurity atom and the host lattice [7,32,33]. There are many examples of the use of this method to reduce the thermal conductivity are in the existing literature such as the additions of nano-inclusions [34,35], dispersal of oxidized nanoparticles [36] and introduction of endotaxial nanoprecipitates through nucleation and growth of a secondary phase [7,28,37-39].

Materials with intrinsically low thermal conductivity due to complicated crystal structures in addition to anisotropic bonding [26,31] and anharmonicity [22,40,41] among other explanations are also used for reduction of the thermal conductivity of thermoelectric materials [42-45]. One very recent and extremely important example of intrinsically low thermal conductivity leading to a large ZT value is SnSe single crystals [40]. Thermal conductivity has been observed to be as low as 0.34 W/mK at 973K decreasing from the room temperature value of 0.70 W/mK along the b axis resulting in a ZT value of 2.6 [40]. Large anharmonicity of the chemical bonds may be an explanation for the thermal conductivity observed for SnSe [7,40]. Related materials such as SnS have gathered significant attention as well. Parker and Singh calculated the band structure of SnS concluding that it has a high Seebeck coefficient and low

thermal conductivity [7,46]. Experimental work has validated the thermoelectric properties of SnS reporting a very low thermal conductivity of 0.5 W/mK at 873 K with Ag doping [47].

Pressure as Tool to Study Transport Properties

Pressure tuning has the potential to provide insight into the effect of structure and volume change on **ZT**, which can be used for reverse engineering development of new and improved thermoelectric materials [48]. In order to characterize and better understand these materials, the physical properties related to thermoelectric efficiency must be studied in detail. Electrical resistivity, Seebeck coefficient, and thermal conductivity are important variables connected to the thermoelectric efficiency [49] and high-pressure experiments measuring the thermal and electrical properties both individually and simultaneously are imperative due to the interplay of these properties.

X-ray diffraction (XRD) measurements have been and continue to be the most widely used technique for studying material properties at high-pressure-temperature (P-T) conditions. Based on XRD measurements one can directly determine P-V-T conditions as well as detect the structural phase transitions as a function of P-T. Although XRD techniques provide valuable information about structural phase transformations and even detection of solid-melt transition, detection of many associated property changes, such as variation in thermal and electrical conductivity, change in magnetic ordering, etc., requires development of new experimental probes. To truly understand any changes in physical properties at high-pressures, it is imperative to correlate the properties to volume and/or structural changes.

PW Bridgman was first to introduce electrical resistance measurements in high P-T experiments with opposed anvil type pressure apparatus [50]. Bridgman also made the first

attempts at measuring thermal properties of materials at high- pressure conditions [51]. Errandonea *et al* in addition to others have utilized this opposed anvil design as developed by Bridgman to understand the behavior of transport properties at high-pressure such as the Hall-effect, electrical resistivity, and thermopower measurements performed on CdTe, InSe, GaSe and ZnTe samples in addition to others [52-54]. However, these opposed anvil designs are not easily compatible with X-ray diffraction techniques and simultaneous XRD and transport property measurements could not be performed.

With the development of diamond anvil cells (DACs) and evolution of X-ray sources, the methods applied by Bridgman were further improved. Both higher pressure ranges and simultaneous structural, thermal, and electrical measurements were developed and a large variety of experiments have been performed. Shchennikov *et al.* and Ovsyannikov *et al.* performed high-pressure electrical resistivity and thermopower measurements on PbTe, PbSe, and ZnTe and Fe₃O₄ single crystals [55-58]. Ke *et al.* explored the electrical transport properties of SnS using specialized microcircuits on the surface of their DACs [59]. Additionally, techniques dedicated to measuring the high-press and high-temperature thermal conductivity of metals using laser heating techniques have recently provided great insight for materials above 3000 K [60,61].

However, the drawbacks of using DACs are the very small sample volume (on the order of 10^{-4} mm³) and difficulties in maintaining a substantial thermal gradient across the anvils during thermal property measurements. Alternatively, large volume presses allow for use of larger sample volumes for both electrical resistance and thermal transport experiments. Recently, initial attempts at simultaneous measurement of the thermal diffusivity/conductivity and the Seebeck coefficient were made by Jacobsen *et al* [62] and Yuan *et al.* [63] using large volume multi-anvil press apparatus, with sample volume on the order of mm³. With larger sample

volume and evolution of multi-anvil apparatus, other experimental probes have also been introduced, such as ultrasonic interferometric sound velocity and electrical conductivity measurements [63-66]. In addition to the greatly increased sample volume, the easily recoverable samples also allows for continued analysis after the compression experiments.

Dissertation Contents and Organization

This dissertation will discuss the design and development of a new technique with great importance to the advancement of thermoelectric materials and understanding the correlation between transport properties and structural properties. A specially designed cell assembly is described with capabilities to measure electrical resistance, Seebeck coefficient and relative variation in the thermal conductivity as a function of pressure alongside the ability to obtain X-ray radiography imaging for determination of sample dimensions and energy-dispersive X-ray diffraction to probe structural properties. The technique is designed for use with a Paris-Edinburgh press and was developed in conjunction with the High-Pressure Collaborative Access Team (HPCAT) located at Argonne National Laboratory (ANL) as part of the Advanced Photon Source (APS) in Chicago, IL. The end goal of this project has been to establish this technique as an option for the general user of the BM-B Sector 16 beamline to study transport properties of materials at extreme conditions. The abilities of this technique to simultaneously measure transport properties including relative changes in the thermal conductivity and structural properties makes it unique among other experimental set-ups designed for high-pressure transport properties [62-67].

As part of this dissertation, the technique was utilized to probe the thermoelectric behavior of binary and ternary compounds at high-pressure conditions correlating the electronic

and thermal properties with structural measurements. Specifically, the thermoelectric behavior of Bi, PbTe, SnTe, $\text{Sn}_{1-x}\text{Mn}_x\text{Te}$ ($x = 12\%$), TiNiSn, and TiCoSb will be discussed in this dissertation. This dissertation will be separated into several chapters. Chapter II will present the design and development of the thermoelectric cell assembly, measurement techniques, and the necessary information to understand the use of diamond-anvil cells, X-ray diffraction, and other important experimental techniques. Chapters III – VIII will present and discuss the sample results. And finally, Chapter IX will draw conclusions about the system developed and the samples measured.

Chapter II – Experimental Details & Techniques

Overview

This chapter will encompass a detailed discussion of both the designed and developed and the commercially available experimental set-ups used for the measurements performed in this thesis as well as the preparation and characterization of the samples studied. A thorough discussion of the sample cell design for the Paris-Edinburgh press developed to conduct high-pressure and high-temperature electrical, thermal, radiographic sample monitoring, and structural measurements *in-situ* will be presented. Within this discussion of the sample cell design, a description of the equipment and techniques used to measure the electrical and thermal properties will be discussed. Finally, a discussion of diamond-anvil cells (DACs) and high-pressure angle-dispersive powder X-ray diffraction will be presented as several of the samples were studied with this method.

High-Pressure Thermoelectric Apparatus

Paris – Edinburgh Press

The Paris-Edinburgh (PE) press originally was developed for use in neutron experiments at high-pressure conditions as described originally by Besson *et al* in 1992 [68]. Although other means of application of high-pressure existed such as diamond-anvil cells (DACs), the small sample volume on the order of 10^{-4} mm^3 was much too small for neutron diffraction type experiments. The PE type press designed by Besson *et al* utilizes sample volumes on the order of 1 mm^3 which is significantly more adequate for neutron diffraction type experiments [68]. The PE type press utilizes a toroidal anvil arrangement which is compressed through use of a

hydraulic press assembly. The pressure application is uniaxial and is typically applied to a sample cell assembly which is extremely adaptable. The cell assembly associated with the PE cell has been adapted to regularly perform X-ray scattering experiments exploring high pressure and temperature phases of materials. Additionally, development of the cell assembly has led to the ability to measure ultrasonic properties at extreme temperatures and pressures. Other adaptations of the sample cell assembly allowed measurement of viscosity of materials by using X-ray radiography imaging at extreme conditions. Furthermore, due to the large sample volume and high pressures and temperatures available to the PE press, new materials and new phases of existing materials have been synthesized at these extreme conditions. Very recently, electrical resistance measurements have been performed with the PE press by further modifications to the sample cell assembly [67-72].

The PE type press at the High-Pressure Collaborative Access Team (HPCAT) Sector 16 BM-B beamline located at Argonne National Laboratory (ANL) at the Advanced Photon Source (APS) is shown in **Figure 3(a)**. This experimental set-up utilizes a pair of tungsten slits to collimate a white X-ray beam (direction is depicted in **Figure 3(a)**) from the synchrotron. This X-ray beam interacts with the sample located within in the sample cell assembly and the resulting diffracted signal from the sample is collected by a Ge solid state detector (Ge-SSD) which is labeled in **Figure 3(a)**. Precise control of the 2θ angle is attained by use of a large Huber stage which holds the Ge-SSD which allows for the collection of energy-dispersive X-ray diffraction patterns. The detector channel - energy calibration is performed by use of NIST Co⁵⁷ and Cd¹⁰⁹ radioactive sources and the 2θ position is calibrated using ambient P-T condition unit-cell parameters of MgO and Pt standard [73,74].

Figure 3(b) is a zoomed in photograph of the local environment around the sample cell assembly. Pressure is attained by applying oil pressure via a series of hydraulic pumping mechanisms which presses against the bottom anvil (labeled in **Figure 3b**). Temperature is measured by use of K-type thermocouples as will be described in greater detail shortly. Also in this image are the electrodes which attach to the power supply for supplying power to the graphite heater within the cell assembly.

Thermoelectric Cell Assembly: Description of Cell Assembly

As previously mentioned, the sample cell assembly for the PE type press is extremely adaptable. Thus, by modifying the cell assembly originally designed for high-pressure melt structural measurements, a cell assembly designed and developed for high-pressure/high-temperature electrical and thermal measurements has been completed. The capabilities of this newly designed cell assembly for the PE press have been described in great detail previously. [75,76]. The individual parts and their purposes will be described in this section. The assembly process, as there are many steps, will be discussed in a future section.

The individual parts required for assembly of the sample cell are as follows:

1. 1 – ZrO₂ Cap: 2.7 mm height, 11 mm diameter bottom, 2 mm diameter top
2. 1 – ZrO₂ Cap: 2.7 mm height, 11 mm diameter bottom, drilled 2 mm diameter hole
3. 1 – Al Cylinder: 2 mm diameter 2.7 mm height (can be composited by Al foil)
4. 1 – Boron-Epoxy Gasket: 14 mm outer diameter, 6 mm inner diameter, 3 mm thickness
5. 1 – Lexan Ring: 14 mm inner diameter, 15 mm outer diameter, 3 mm thickness
6. 1 – MgO Ring: 6 mm outer diameter, 2 mm inner diameter, 2.5 mm thickness
7. 2 – K-Type Thermocouples: 0.125 mm diameter wire

8. 2 – Alumel Coils: 0.125 μm diameter wire, 0.270 mm ID of coil, 0.400 mm OD of coil
9. 2 – Chromel Coils: 0.125 mm diameter wire, 0.270 mm ID of coil, 0.400 mm OD of coil
10. 1 – Sample Pellet: 2 mm diameter, varying thickness (typical – 500 to 700 μm)
11. 2 – Single-crystal diamond disc: 2 mm diameter, 0.5 mm thickness
12. 1 – Graphite Disc: 5.5 mm diameter, 0.150 mm thickness, edge flattened
13. 1 – Al Disc: 2 mm diameter, 0.600 – 0.700 mm thickness, pressed Al foil
14. 2 – Molybdenum Foil: 0.05 mm thickness, shaped as described
15. 2 – Mica Disc, 6 mm diameter, 0.120 mm thickness
16. 4 – Insulating Sheaths for Thermocouples
17. 2 – K-type Thermocouple Connectors

Figure 4 is a scaled schematic of the thermoelectric sample cell assembly designed for electrical resistance, Seebeck coefficient, and thermal gradient measurements. Located at the top and bottom of the cell assembly are zirconia (ZrO_2) caps [Part #1 and #2] which act as electrical and thermal insulators due to the low thermal conductivity of ZrO_2 (1.7 – 2.7 W/mK) and the very high electrical resistance ($10^{18} \Omega$) [77]. Both caps have identical dimensions, except that the bottom ZrO_2 cap has a 2 mm hole drilled through the center. This hole is drilled in order to make room for an aluminum cylinder [Part #3] which acts as a heat sink to the bottom tungsten-carbide anvil of the PE press. Between each of these caps, there is a boron-epoxy (BE) gasket [Part #4] which is made by mixing amorphous boron powder and a hardening epoxy after which it is then baked to harden the mixture. In more recent experiments, this BE gasket has been manufactured and purchased as a regular use part at the beamline. Around the BE gasket is a Lexan plastic ring [Part #5] which acts as an outer containment for the gasket as it flows during compression. An MgO ring [Part #6] is located at the center of the BE gasket which is necessary for containment

and support of the sample column. Additionally, this MgO ring is used as a pressure marker during the experiments which will be described in more detail later. Furthermore, the BE gasket, and the MgO ring act to provide thermal and electrical insulation in addition to support of the sample column.

The BE gasket, MgO ring, and Lexan ring have four 600 μm aligned holes drilled through them in the radial direction in order to make room for insertion of the K-type thermocouples [Part #7] and the thermocouple coils [Part #8 and #9]. Each pair of holes is staggered in placement to make a height difference between the top and bottom thermocouple. The K-type thermocouples are purchased from Omega Engineering with pre-made junctions of bare alumel and chromel wires which are compressed between two flat tungsten-carbide surfaces using a hand-press to flatten the thermocouple junction and reduce the size. These thermocouples act as both the thermal probe and the electrical probe for the measurements performed with this set-up. In order to minimize potential shearing and breaking of the wires during compression, the thermocouple coils [Part #8 and #9], which are made of the same alumel and chromel materials as the thermocouple wires, are slid over the bare thermocouples and inserted into the 600 μm aligned holes drilled through the Lexan ring, BE gasket, and MgO ring. They provide protection to the fragile bare thermocouple wires by elongating as the cell assembly is compressed and absorbing this shear stretching as the BE gasket flows.

The flattened K-type thermocouples junctions are located directly above and below the sample [Part #10] inside the sample column as depicted in **Figure 4**. The thermocouples and the sample are sandwiched between a pair of single-crystal diamond discs [Part #11] (Almax EasyLab). In earlier designs of the cell assembly, polycrystalline CVD diamond discs were used, but for several reasons, it was determined that this experimental set-up requires the use of single-

crystal diamond discs. Among these reasons for switching from polycrystalline to single-crystal diamond discs, was the polycrystalline diamond discs were determined not to last for many experiments due to severe cracking and breaking after completion of the experiment. Additionally, the thermal and electrical properties of single-crystal diamond is far superior when compared to the polycrystalline diamonds, and as such, the single-crystal diamonds are recommended for use for the sample cell assembly and were used in the experiments described throughout this thesis. The single-crystal diamond discs provide optimal heat flow due to the very high thermal conductivity of diamond ($>2000 \text{ W/mK}$) and excellent electrical isolation due to the very large electrical resistance of diamond ($>100 \text{ G}\Omega\text{m}$). This combination of physical properties is necessary for the experimental set-up in order to electrically isolate the sample and thermocouple from the graphite heater [Part #12] while allowing for the optimal heat flow through the sample column and into the bottom tungsten-carbide anvil acting as heat sink. This stack of diamond disc and sample are located within the center of the MgO ring, and at the very bottom of this sample stack an Al disc [Part #13] is situated which also aids with the heat flow through the sample stack to the heat sink. Additionally, this Al disc also acts as a spacer in order to ensure the sample disc is located near the center of the cell assembly so as to allow for X-ray diffraction and radiography imaging measurements.

The sample column fills the entire space within the center of the MgO ring totaling 2.5 mm in height after accounting for the thickness of the sample, diamond discs, Al disc, and the thermocouple junctions. This leaves a 0.5 mm space unfilled above the MgO ring, yet still within the larger diameter BE gasket. Placed within this 0.5 mm space is first the graphite heater which is in direct contact with the top diamond disc as depicted in **Figure 4**. Additionally, two molybdenum foils [Part #14] make contact with the graphite heater and the top and bottom

tungsten-carbide anvils of the PE press which act as the electrical leads for the power source of the heater. One of the foils is between the bottom ZrO_2 cap and the BE gasket as shown in **Figure 4**. This foil has a “long arm” that lies between the MgO ring and the BE gasket with only a small tab reaching the top which will make contact with the graphite disc. The other foil lies between the top ZrO_2 cap and the BE gasket. This foil does not have an arm and instead only has a small tab which is bent such that it makes contact with the edge of the graphite heater as depicted in **Figure 4**. Since the molybdenum foil is placed on top of the graphite heater, it is necessary to ensure that only the edges of the graphite heater make contact with the foils. To achieve electrical isolation for the majority of the graphite heater, two thin discs of mica [Part #15] are punched out of a mica sheet. They are glued to the bottom portion of the top molybdenum foil exposing only the tab to make contact with the heater. Once the mica discs are glued to the molybdenum, this piece can be glued to the top of the cell assembly covering the 6 mm hole with the graphite heater and other cell assembly parts. Placed directly on top of this molybdenum piece in the center will be the top ZrO_2 cap [Part #1], which is glued into place as well. Once the parts are all in place, the thermocouple sheaths and thermocouple connectors are placed in order to connect the cell assembly to electrical connections at the PE press. The full assembly process is described in great detail in the following section.

Thermoelectric Cell Assembly: Assembly Process

The assembly of the thermoelectric cell has been refined throughout the duration of this project. Presented in this thesis is the existing process of assembly which is separated into two sections. The first will describe in detail the procedure for preparation of a few sample cell parts that need particular care such as sanding, flattening, etc. The second section will describe the procedure to assemble the thermoelectric cell. It should be noted that this is of course only a

guide for the reader or future experimenter wishing to assemble a cell and the order of assembly may have some flexibility depending on the particular sample or other conditions for the future experiment.

Pre-Assembly Steps:

Step #1: Weigh enough powder of sample to produce a 2 mm diameter and 0.6 mm thick cylindrical pellet using a 2 mm pellet die pressed with a hand-press to produce Part #10.

Step #2: Press multiple 2 mm diameter Al pellets using Al foil using with a 2 mm pellet die and hand-press to produce Part #3 and Part #13.

Step #3: Prepare alumel and chromel spring coils of the proper diameter to produce Part #8 and Part #9.

Step #4: Ensure all parts are of the proper thickness especially the graphite heater. If they are not, sand them with fine sandpaper until they have reached the proper thickness.

Assembly Steps:

Step #1: Place the BE gasket [Part #4] with attached Lexan ring and bottom molybdenum foil upon a flat surface and secure with small pieces of tape.

Step #2: Insert the Al disc [Part #4] within the center of the MgO ring pushing it to the bottom of the 2 mm hole ensuring it lies flat against bottom surface. This can be achieved through use of the flat-end of a drill-bit with diameter less than 2 mm or another flat surfaced tool with diameter less than 2 mm. Clean out 2 mm chamber with air duster to ensure no MgO flakes have fallen inside the chamber. The result of this step is displayed in **Figure 5**.

Step #3: Insert the bottom diamond disc [Part #11] in the same fashion as Step #2. After insertion of the diamond disc, again clean the chamber to avoid MgO flakes from remaining in the hole. The result of this step is depicted in **Figure 6**.

Step #4: Insert one of the flattened thermocouples through the bottom set of holes drilled into the Lexan ring/Be gasket/MgO ring. Pull the wire through carefully so as not to damage the junction. Once the junction reaches the center of the BE gasket, rotate the wires until the junction sits flat against the diamond disc. It may be necessary to press on the thermocouple junction with the flat-end of a drill bit with less than 2 mm diameter. The result of this step is depicted in **Figure 7**.

Step #5: Determine which wire is alumel and which wire is chromel. Over each wire, place the corresponding “spring coil” [Part # 8 and #9] and slide it along until reaching near the hole in the BE gasket. Once near the hole of the gasket, it is recommended to tape down the thermocouple wire to ensure proper alignment of the junction is not disturbed. With the wire secured, insert the “spring coil” all the way into the BE gasket and MgO ring. Glue in place with superglue. An example of this step is displayed in **Figure 8**.

Step #6: Insert sample carefully into the chamber on top of the bottom thermocouple as placed in Step #5. The result of this step is shown in **Figure 9**.

Step #7: If the sample stack sits slightly below the edge of the top hole, it may be possible to insert the top thermocouple in a similar fashion as done in Step #4. However, if the sample sits too high, the thermocouple junction may become stuck in the MgO ring. If this occurs, slight pressure can be applied to the sample in order to tilt it either down or up, rocking it on the bottom thermocouple until enough of the top hole is unhindered so as to pull the junction through. If this approach does not work, the top thermocouple can be inserted from the top by

individually threading the alumel and chromel wires through and maneuvering the thermocouple junction such that it lays flat against the sample. **Figure 10** shows the result of placing the thermocouple on top of the sample.

Step #8: Repeat Step #5 with the other pair of “spring coils” available. A depiction of the sample cell assembly at this stage is displayed in **Figure 11**.

Step #9: Insert the top diamond disc into the 2 mm sample chamber. In order to ensure the sample stack is as compact as possible it is recommended to press on this top diamond disc with the flat-end of a drill bit. The insertion of the top diamond disc is displayed in **Figure 12**.

Step #10: Place the flattened end (sanded previously) of the graphite heater underneath the molybdenum tab and allow it to sit flat against the diamond disc and MgO ring. Carefully ensure the graphite heater is sitting flat by applying slight pressure to it. Once it has been placed and is set flat against the diamond disc and MgO ring, very carefully bend the molybdenum tab down towards the graphite heater and allow it to make slight contact. A picture depicting the result of this step is displayed in **Figure 13**.

Step #11: Place two small spots of superglue on the top surface of the BE gasket on each side of the 6mm inner hole. Then, take the pre-constructed top molybdenum foil with mica discs attached under the tab and place it tab-side down onto the BE gasket covering the 6 mm hole. The orientation is critical in this step. The top molybdenum foil must be oriented such that the tab is on the opposite side of the 6 mm hole as the tab for the already placed molybdenum foil. Once the top molybdenum foil is in place, hold it until the superglue has dried. This step is displayed in **Figure 14**.

Step #12: Again place a few spots of superglue on the BE gasket, and also in the center of the top molybdenum foil. Place the ZrO_2 cap with no hole drilled onto the top of the cell assembly and hold until the glue has completely dried. This step is displayed in **Figure 15**.

Step #13: Turn the entire cell assembly over, preferably placing it into a holder than can accommodate the shape of the ZrO_2 cap. Place a few spots of glue around the center 2 mm hole (the sample stack from bottom), but ensure that the glue is not too close to the center to avoid glue entering the sample chamber. Place the bottom ZrO_2 with a 2 mm hole drilled through it on the BE gasket surface centering the 2 mm hole with respect to the 2 mm sample stack hole. Hold until the glue has dried.

Step #14: Apply a small amount of silver paint to the bottom surface of the one or two Al discs [Part #3] and insert the Al discs into the hole in the ZrO_2 to fill the space. A depiction of this step is shown in **Figure 16**.

Step #15: The final step to completing the cell assembly process requires the thermocouple sheaths be placed over the thermocouple wire to ensure insulation when the cell assembly is placed on the PE press anvil.

High-Pressure Thermoelectric Measurements

Radiography Imaging: Sample Thickness Measurements

The sample thickness is monitored throughout the entire pressure range by collecting X-ray radiography imaging at each pressure increase and an example radiography image is displayed in **Figure 17**. By pre-measuring a standard with known dimensions, a length scale can be determined which for all experiments performed has been measured as $0.95 \mu\text{m}/\text{pixel}$ [70].

With this length scale, the thickness of the sample can be obtained by plotting the absorption intensity as a function of pixels as displayed in **Figure 18** which corresponds to the arrow path in **Figure 17**. From this plot profile, the number of pixels between the top and bottom edge of the sample can be determined and this number can then be converted to a thickness in μm using the pre-determined length scale. The location of the top and bottom edge are determined by calculating the half-intensity point for each side of the absorption intensity plot and finding the pixel number that corresponds to this midpoint. Then, the larger pixel number is subtracted from the smaller pixel number, thus giving the difference between the top and bottom edge. This thickness measurement is extremely important in determining the relative changes in thermal conductivity as pressure is increased and is very valuable as it is a direct measurement of this dimension of the sample.

High-Pressure Electrical Resistance/Resistivity Measurements

Figure 19 depicts a schematic of the generalized experimental set-up for the electrical resistance measurements performed with this technique. A U3606B Agilent multimeter with low-resistance mode enabled is used for the electrical resistance/resistivity measurements in this study. Typically in an electrical resistance measurement, the V_+ and V_- leads of the Agilent multimeter is connected to the alumel wires, and the I_+ and I_- leads are connected to the chromel wires. However, although this is a typical connection set-up, the opposite connections will provide the same output. Also, a typical convention that has been followed for all of the measurements of electrical resistance is the (+) connection for both the current and voltage leads is attached to the top thermocouple wires and the (-) connection is attached to the bottom thermocouple wires. Thus, by applying Ohm's Law $\mathbf{V = IR}$, the electrical resistance given an

input current can easily be measured. From this measured resistance, the electrical resistivity can be calculated by use of

$$\rho = \frac{RA}{L} \quad \text{Equation 5}$$

where **R** representing the electrical resistance measured, **A** representing the cross-sectional area, and **L** being the distance between the top and bottom thermocouple (or sample thickness). These dimensions are measured by use of radiographic imaging as mentioned previously. The sample thickness, **L**, in **Equation 5** and depicted in **Figure 18** can be determined and the sample diameter, **D**, is 2 mm, which can be used to calculate cross-sectional area. From **Equation 5**, a calculation of the electrical resistivity can be obtained once the electrical resistance is measured using the schematic and accounting for the sample dimensions.

High-Pressure Seebeck Coefficient Measurements

The Seebeck coefficient can be defined as the ratio of the thermoelectric voltage to the temperature difference across a material as given by **Equation 6**:

$$\alpha_S = \frac{\Delta V}{\Delta T} \quad \text{Equation 6}$$

where ΔV is the thermoelectric voltage as measured from the hot-side to the cold-side and ΔT is the temperature difference. A simple method is described by Polvani *et al.* [78] to determine the Seebeck coefficient using thermocouples with known Seebeck coefficient as electrical leads independent of the environmental temperature. In our setup, the thermoelectric voltage is measured from the top thermocouple to the bottom thermocouple. Specifically, our experimental set-up uses K-type thermocouples with chromel and alumel wires as previously mentioned.

Equation 7 describes the Seebeck coefficient of the sample independent of ΔT , solely relying on the voltage measurements:

$$\alpha_S = \frac{\alpha_A - r \alpha_C}{1 - r} \quad \text{Equation 7}$$

where r is the ratio of the alumel-alumel and chromel-chromel voltage differences ($r = \frac{\Delta V_{AA}}{\Delta V_{CC}}$) and $\alpha_A = -18.3 \mu V/K$ and $\alpha_C = 22.2 \mu V/K$ are the Seebeck coefficient of alumel and chromel, respectively. **Figure 20** gives a schematic view of the cell assembly depicting the voltage measurement in our experiment.

An important discussion is the pressure effect on K-type thermocouples which has been reported by Bundy *et al.* [79] to be at most 2 °C per 100 °C ΔT over the pressure range of 0 - 6 GPa. Additionally, more recent work performed by Nishihara *et al* [80] reports maximal changes in the Seebeck coefficient of alumel and chromel single wires as 2.5 $\mu V/K$ at 900°C and 2 GPa. Nishihara *et al.* [80] also reports a temperature correction between 0 – 3 °C throughout the entire pressure range of 0 - 8 GPa. As such, within the typical error of K-type thermocouples, which is on the order of approximately 2 °C, the pressure effect is negligible.

High-Pressure Thermal Conductivity Measurements

Thermal conductivity can be determined by measuring the precise power input from the graphite heater (**P**), the sample thickness (**Δx**), having knowledge of the cross-sectional area of the heat path (**A**), and measurement of the change in temperature across the top to bottom thermocouples (**ΔT**) as **Equation 8** implies.

$$k = \frac{P \Delta x}{A \Delta T} \quad \text{Equation 8}$$

Figure 21 depicts these parameters and their relationship to the sample cell assembly schematically.

The power input from the graphite heater is controlled via a PID feedback loop by changing the voltage and current to attain a user input power value. The sample thickness can be accurately measured as discussed in the previous section. Knowledge of the cross-sectional area is attainable by strict use of a 2 mm pellet die and machining the MgO disc inner diameter to 2 mm. However, the proper cross-sectional area of heat flow is a ratio of cross-sectional areas of the graphite heater (5.5 mm diameter) as compared to the 2 mm diameter diamond disc and sample stack in direct contact with the heater. Despite the ability to determine the dimensions of the sample accurately and obtain a measurement of the input power from the graphite heater, a severe issue arises when calculating an absolute thermal conductivity of the sample. Although the power input from the heater is known, the absolute heat loss to the surrounding environment is not. This heat loss, without extensive thermal modeling, makes it extremely difficult to ascertain the precise input power from the graphite heater that reaches the sample, which is the quantity of vital importance to accurate determination of the thermal conductivity as **Equation 8** states. However, if the power loss remains constant with pressure per a given cell configuration, a relative change in the thermal conductance can be extracted and then utilized to determine the relative variation in the figure of merit for any measured sample. It is this quantity, the relative change in the thermal conductivity as a function of pressure which is reported throughout this dissertation. This relative change is determined by calculating the thermal conductivity value at the lowest pressure measured for each sample, and obtaining the ratio of each data point to this lower pressure value.

High-Pressure Dimensionless Figure of Merit, ZT Measurements

The dimensionless figure of merit, ZT , has been defined previously in **Equation 1**. This quantity is calculated from the measurement of the electrical resistivity, Seebeck coefficient, thermal conductivity, and absolute temperature as discussed in the previous sections. As this technique has focused on obtaining high-pressure trends in the thermoelectric behavior of materials due to issues with determining the absolute thermal conductivity and electrical resistivity, only relative changes in ZT will be discussed throughout this dissertation. The relative changes in ZT are determined by calculating the absolute ZT from the measurements and normalizing the ZT values to the lowest pressure value measured. This method allows for an assessment of the thermoelectric behavior as a function of pressure as a trend in a self-consistent manner.

Pressure Determination: Paris-Edinburgh Press

As depicted in **Figure 4**, an MgO ring is located directly in contact with the sample along the edge. This MgO ring has the mechanical importance of providing a sturdy retaining structure for the sample stack, and also provides a material to use as a pressure marker. Through use of the equation of state described in detail by Kono *et al* [74], the pressure can be determined from calculating the peak location of the X-ray diffraction peaks for MgO. Since the measurement of the pressure is taken at the edge of the sample, as this is where the MgO ring lies, the pressure at this point is different than the pressure at the center of the sample. Initial measurements performed on MgO samples by themselves revealed an approximate 0.1 GPa to 0.2 GPa maximum deviation from the center of the sample to the edge. As the sample studied have differing bulk moduli, this pressure deviation may increase or decrease depending on the

material studied. However, it is likely this value does not exceed a few tenths of a GPa. In addition, there is likely some inherent error to using the peaks of MgO to determine the pressure, but the deviation from the edge to the center of the sample is likely larger than these inherent errors.

Raw High-Pressure Thermoelectric Data

Table 1 displays an example thermoelectric data set as taken at the beamline. Each oil pressure is recorded in **P (psi)** of this table. As discussed previously, power input to the heater is increased to increase the temperature and the wattage input to the graphite heater is displayed in **Power (W)**. Also documented in this **Table 1** is the raw voltage difference values measured to determine the Seebeck coefficient (**Ch1-Ch2** & **Al1-Al2**). Only two voltage differences are required for the determination of the Seebeck coefficient as **Equation 7** implies since only the voltage difference across the top chromel to bottom chromel and top alumel to bottom alumel wires is necessary. The other two voltage combinations refer to cross-wires that are not relevant to the thermoelectric measurements. **Table 1** also documents the electrical resistance value (**R (Ohms)**) measured at each pressure and temperature and alongside the sample thickness as determined by radiography images as described previously, the electrical resistivity can be calculated. The temperature is also logged for both the top and bottom K-type thermocouple and the difference is calculated (**T1** & **T2**).

Table 2 displays all calculated values as determined from the collected raw data as depicted in **Table 1**. The first column (**P (GPa)**) indicates the determined pressure in GPa corresponding to each oil pressure and calculated by analyzing the EDXRD patterns for MgO as discussed previously. **ΔT (K)** of **Table 2** depicts the temperature difference as calculated from

the individual measurements of the thermocouples situated above and below the sample. The next column, **Avg T (K)**, is the calculated average temperature performing a statistical average of the temperature readings of the top and bottom thermocouples from the data displayed in **Table 1**. The electrical resistivity is displayed in **ρ (ohm-m)** of **Table 2** and is calculated based on **Equation 5** discussed previously using the electrical resistance from **Table 1** in **R (ohms)** and the sample thickness. The Seebeck coefficient tabulated in **α ($\mu\text{V/K}$)** of **Table 2** is calculated based on **Equation 7** as mentioned in a previous section using the voltages from **Ch1-Ch2** and **Al1-Al2** from **Table 1**. **κ (W/mK)** displays the calculated thermal conductivity using **Equation 8** using **Power (W)** for the power input to the graphite heater and **Δx (m)** for the sample thickness. Finally, the dimensionless figure of merit can be calculated using the thermoelectric properties measured and the average temperature of the sample from **ZT** from **Table 2**.

High-Pressure Angle-Dispersive X-ray Diffraction Measurements

Diamond Anvil Cell

The high-pressure angle-dispersive powder X-ray diffraction measurements were performed using diamond anvil cells (DACs) of the Princeton symmetric type design which is depicted in **Figure 22** [81]. A DAC generally operates according to **Figure 23** where pressure is applied to the sample through use of two opposing diamond anvils of the sample diameter where the force is supplied typically through the tightening of a series of screws [82,83]. A metallic gasket is placed between the opposing anvils to provide an environment for the sample chamber by providing strength enough to retain the pressures being applied. The gasket is usually pre-indented by placing it between the diamonds and compressing it from a starting thickness of $\sim 250\mu\text{m}$ to $\sim 20 - 50\mu\text{m}$. This pre-indented gasket is then either centered under an electric

discharge machine (EDM) or a laser-drilling system to drill a hole in the center of the pre-indent creating the sample chamber. The diameter of this hole is highly dependent on the culet diameter of the diamonds being used in the experiments. For instance, a 300 μm diamond culet diameter will usually have an associated drilled hole in the gasket of 80 – 120 μm , while a 150 μm diamond culet diameter is have a gasket hole of 40 – 50 μm . A typical aspect ratio between the hole diameter and the diamond culet diameter is approximately 1:3. Once the hole has been drilled in the pre-indented gasket, the gasket is cleaned and placed upon one of the two diamonds in the DAC. Finely ground sample, a ruby sphere, and a pressure transmitting media (PTM) of some kind are introduced to the sample chamber. For the measurements in this study, a gas-loading system located at GSECARS was used to load the DACs with Ne PTM. [84]

Pressure Determination: Ruby Fluorescence

Ruby spheres are used as an *in-situ* pressure marker by measuring the spectral shift of the R_1 fluorescence line of ruby excited by a 542 nm laser and an example spectrum of the ruby fluorescence is depicted in **Figure 24**.

In this spectrum, two emission peaks are observed corresponding to two separate energy levels in the ruby energy diagram. Studies have been performed to establish a relationship between the spectral shift of these emission lines and the pressure applied to the ruby through hydrostatic compression [85,86]. The pressure can then be determined by

$$P = \frac{A}{B} \left[1 + \left(\frac{\Delta\lambda}{\lambda_0} \right) \right]^B \quad \text{Equation 9}$$

where P represents the pressure, $\Delta\lambda$ represents the wavelength shift of the R_1 fluorescence line, λ_0 represents the initial wavelength of the R_1 line at ambient pressure, and A and B are constants

determined as fit parameters [85]. Mao *et al.* reported these values as **A** = 19.04 Mbar and **B** = 7.665 [85].

Powder X-ray Diffraction and Bragg's Law

Powder X-ray diffraction (XRD) is a well-established and widely used technique to understand the crystal structure of solids. Commercial laboratory size systems are capable of performing XRD to characterize crystal structure of synthesized materials while the use of synchrotrons such as the Advanced Photon Source at Argonne National Laboratory have an extremely high flux which allows for study of the extremely small samples contained within DACs. Commercial systems typically use a copper or molybdenum source bombarded with electrons to produce X-rays at very specific wavelengths governed by the energy levels of the source material. In the case of Cu, Cu K- α radiation is emitted at a wavelength of 1.54 Å. Since the wavelength of these X-rays is near the separation distance of planes within a crystalline lattice, when these monochromatic X-rays hit the sample, diffraction occurs and obeys Bragg's Law defined as

$$2d \sin \theta = n \lambda \quad \text{Equation 10}$$

where **d** is the separation distance between lattice planes, **θ** is the scattering angle, **n** is a positive whole number, and **λ** is the wavelength of the incumbent X-rays interacting with the sample [87].

Figure 25 depicts this process with a schematic of a set of crystalline lattice planes and the interaction of the X-rays with these lattice planes. For the high-pressure XRD experiments utilizing the DACs, the wavelength is kept constant while the angle is allowed to vary and is measured. Thus, according to **Equation 10** there will only be a signal at particular angles.

High-Pressure Powder X-ray Diffraction Measurements

The angle-dispersive high-pressure x-ray diffraction (HPXRD) measurements were performed at Argonne National Laboratory at the Advanced Photon Source. The data for all samples studied in this dissertation was collected at the BM-D beamline at Sector 16 of the High-Pressure Collaborative Access Team (HPCAT) using the previously discussed Princeton symmetric type DACs. An incident monochromatic X-ray beam was focused down to a $20 \times 20 \mu\text{m}^2$ onto the sample using Kickpatrick-Baez mirrors with a wavelength of 0.30655 \AA . A MAR-345 image plate is used in the experiments to obtain high quality powder X-ray diffraction patterns and the detector distance was calibrated using a CeO_2 standard. The diffracted signal from the sample leaves the DAC as a series of cones a schematic of which is depicted in **Figure 26(a)** [88]. **Figure 26(b)** is an example of the raw data collected as a MAR-345 image showing the Debye-Scherrer rings occurring at very specific diameters from the center of the detector corresponding to specific 2θ angles as presented in **Figure 26(a)**.

These rings can then be integrated using the calibrated X-ray wavelength, detector distance, and other calibration parameters determined by use of the CeO_2 standard as mentioned into an integrated intensity as a function of two-theta angle plot. This integration is carried out using FIT2D and Dioptas software [89,90]. Additionally, these MAR-345 images are corrected for distortions and spurious diamond diffraction peaks with use of these software. An example of a distortion corrected and integrated XRD pattern is depicted in **Figure 27**.

As mentioned previously, only very particular angles give rise to a diffraction signal corresponding to specific lattice planes of the crystal structure of the material. After distortion correction and integration, structural refinements to determine the lattice parameters, bond

lengths, atomic positions, and other parameters can be performed on the XRD pattern displayed in **Figure 27** using MDI JADE 2010 software and Rietica (LHPM) software packages [91,92].

Equation of State

An equation of state (EOS) is mathematical description of the relationship between various thermodynamic variables such as pressure, volume, temperature, or internal energy. These equations can describe the properties of gases, mixtures, solids, and other states of matter. Such equations that describe gaseous materials are the ideal gas law, van der Waals' EOS, among others and various equations describe the properties of solid materials. Specifically important to this dissertation are the Birch-Murnaghan EOS, and the Rose-Vinet EOS. These EOS describe the relationship between volume and pressure. From the refinements as discussed in the previous section, several parameters can be determined corresponding to the crystal structure of materials. The lattice parameters can be used to calculate the unit-cell volume of the crystal structure of the sample and if the unit-cell volume is tracked with increasing pressure, a determination of the compressibility of the material is obtainable. Compressibility is defined as

$$\beta = -\frac{1}{V} \left(\frac{\partial V}{\partial P} \right)_T \quad \text{Equation 11}$$

where **V** represents the volume, **P** represent the pressure, and **T** represents the temperature [93].

The inverse of the compressibility is defined to be the bulk modulus and is given by

$$B = -V \left(\frac{\partial P}{\partial V} \right) \quad \text{Equation 12}$$

where **V** and **P** represent the volume and pressure, respectively [93]. The bulk modulus is a measure of the incompressibility of a material as it is the inverse of the compressibility. It quantifies the change in volume of a material as pressure is increased and can be determined by

measurement of XRD at various pressures. With a collected set of data between the unit-cell volume and the pressure corresponding to each unit-cell volume, this data can be fit to the Birch-Murnaghan EOS and the Rose-Vinet EOS to determine the bulk modulus. The 3rd – order Birch-Murnaghan EOS (BM-EOS) is defined as:

$$P(V) = \frac{3B_0}{2} \left[\left(\frac{V_0}{V} \right)^{\frac{7}{3}} - \left(\frac{V_0}{V} \right)^{\frac{5}{3}} \right] \left\{ 1 + \frac{3}{4} (B'_0 - 4) \left[\left(\frac{V_0}{V} \right)^{\frac{2}{3}} - 1 \right] \right\} \quad \text{Equation 13}$$

where \mathbf{B}_0 represents the bulk modulus, \mathbf{V}_0 represents the ambient pressure initial unit-cell volume, \mathbf{V} represents the unit-cell volume, and \mathbf{B}'_0 is the pressure derivative of the bulk modulus [94]. For consistency, another EOS that can be used to determine the bulk modulus and compare the values between each is the Rose-Vinet EOS which is defined as:

$$P(V) = 3 B_0 \left(\frac{1-\eta}{\eta^2} \right) e^{\frac{3}{2}(B'_0-1)(1-\eta)}; \eta = \sqrt[3]{\frac{V}{V_0}} \quad \text{Equation 14}$$

where \mathbf{B}_0 , \mathbf{V}_0 , \mathbf{V} and \mathbf{B}'_0 represent the same quantities as described for the BM-EOS [95]. These EOS will be utilized throughout this dissertation for the understanding of the high-pressure behavior of various materials.

Chapter III – Sample Results: Bismuth

Overview

This chapter will discuss the results of our measurements with the system on elemental Bi samples. Bi has several well known structural phase transitions in the pressure and temperature range available to our apparatus [50,51,96-98]. These well known structural phase transitions correspond to significant changes to the electrical and thermal properties of the material [50,51]. A detailed discussion of electrical resistivity, Seebeck coefficient, thermal conductivity, dimensionless figure of merit **ZT**, energy-dispersive X-ray diffraction, and radiography imaging measurements will be presented comparing, where possible, these results to the existing literature.

As a test sample, high purity (99.99%) Bi powder purchased from Sigma Aldrich was pressed into 2 mm diameter and 500 μm thick pellets using a tungsten carbide pellet die (from Hamasho Corporation). A phase diagram of bismuth reported by Chen *et al.* is shown in **Figure 28** as reference [96]. Experiments were performed over a wide range of temperature and pressure conditions to ensure consistency, reliability, and to identify the ideal working conditions for our apparatus. In **Figure 28**, arrows are shown to indicate the pathways taken in each experiment. Isobars were taken at varying pressures to determine the Seebeck coefficient as a function of temperature, and an isothermal measurement was also performed over the pressure range 1 GPa to 3.1 GPa to determine the pressure dependence of the Seebeck coefficient.

High-Pressure Thermoelectric Measurements

Radiography Sample Thickness Measurements

Using the technique described in the previous chapters in analyzing the radiographic images obtained at each pressure, the sample thickness can be determined as a function of increasing pressure. **Figure 29** depicts a series of radiographic images with indicated pressure aligned to the far edge in order to make the visualization more clear. Clearly obvious from **Figure 29** is a continually decreasing trend in the thickness of the sample as is expected with increasing pressure. A quantitative representation of this data is depicted in **Figure 30** as the sample thickness as a function of pressure calculated from the technique mentioned in **Chapter II (Figure 17 and Figure 18)**. The large initial decrease in sample thickness within the first 0.5 GPa compression may be due to relatively large variations in the cell part dimensions especially with the thickness of the BE gasket. This enforces re-settling of all cell parts with sample at the center while compressibility of the sample would not be changed in the applied pressure range at all based on the known phase diagram. After this initial sharp decline in sample thickness, the variation becomes much more consistent as would be expected from a well compressed sample pellet.

Isobaric Seebeck Coefficient Measurements

Figure 31 shows the results of the isobaric measurements of the Seebeck coefficient performed on the Bi sample. **Figure 31(a)** and **Figure 31(b)** represent the plots of the Seebeck coefficient as a function of temperature corresponding to the paths labeled A and C, respectively in **Figure 28**. We have collected isobars, the first at 0.8 GPa and the second at 1.1 GPa, which both lie in a region with no known phase transition in order to understand the behavior of the

Seebeck coefficient in these conditions. Also, **Figure 31(a)** and **Figure 31(b)** show no significant change in the Seebeck coefficient over the temperature range studied at these pressures. **Figure 31(a)** has a small temperature range of only 305 K to 325 K and over this temperature window there is almost no change in the Seebeck coefficient as portrayed in the plot. The temperature for this experiment was kept low because an isotherm was taken at 325 K to obtain the Seebeck coefficient as a function of pressure for Bi. **Figure 31(b)** has a temperature range of 325 K to 425 K which was chosen to give a large enough temperature range to see changes in the Seebeck coefficient and was kept low enough to ensure the experiment stayed well below the liquid phase which occurs near 500 K at this pressure as shown in **Figure 28** [96]. Over the temperature range of 320 K to 360 K a slight variation in the average value of the Seebeck coefficient is observed, and upon further increasing the temperature the Seebeck coefficient stays constant. Due to the large size of standard errors, however, the variations look insignificant.

On comparing the Seebeck coefficient in our measurements at 0.8 GPa and 1.1 GPa near 300 K with the measurements performed by Ferdin *et al.* [99], we found a difference in absolute values. Our measurements give a value of approximately $-34 \pm 4 \mu\text{V/K}$ at 1.1 GPa and 325 K and Ferdin *et al.* measurements yield approximately $-60 \mu\text{V/K}$ [99]. This difference may be contributed by the sensitivity of electronic properties of Bi to small impurities and the different sample forms with powder pellet and single crystal, respectively. Chandrasekhar *et al.* performed Seebeck measurements on single crystal Bi samples and conclude a significant difference in the Seebeck coefficient caused by changing the orientation of the three-fold symmetry of the Bi crystal [100]. The polycrystalline nature of our samples alleviates the significance of orientation; however, if any preferred orientation is introduced when pressurizing the sample, it may

contribute to the variations. Although there is a significant difference in the values between our measurements and the Ferdin *et al.* [99], the values shown in **Figure 31(a)** and **Figure 31(b)** are from separate experimental runs and thus provide evidence for consistency for our apparatus when measuring the Seebeck coefficient in the given experimental conditions.

High-Pressure Electrical Resistance Measurements

Figure 32 displays the results of two measurements of the electrical resistance as a function of increasing pressure for Bi. Both of these measurements are separate experimental runs of Bi performed to provide feasibility and reproducibility of the electrical measurements. Both experiments reveal significant changes to the electrical resistance as pressure is increased. For experiment #1 and #2, there is a slight increase in electrical resistance from 2.2 GPa to 2.7 GPa followed by a significant decrease reaching a minimum for both experiments. The minimum for experiment #1 is attained at a pressure of 2.9 GPa and the minimum for experiment #2 is attained at 3.0 GPa. The onset decrease in the electrical resistance for both experiments agree well with each other and correlate very well to the Bi – I to Bi – II pressure-induced structural phase transition as indicated in the Bi phase diagram displayed in **Figure 28**. Upon attaining a minimum value for electrical resistance, it increases in both experiments and reaches a plateau. For experiment #1, this plateau is reached at 3.0 GPa and for experiment #2, it is reached at 3.2 GPa. Again, both experiments agree with each other within 0.2 GPa and this plateau correlates with the Bi – II to Bi – III structural phase transition. This qualitative behavior for both experiments agrees extremely well with previously published literature on the high-pressure electrical resistance behavior of Bi [50,96-98].

High-Pressure Isothermal Seebeck Coefficient Measurements

Figure 33 displays the results of isothermal Seebeck coefficient measurements on the Bi sample over the pressure range of 1.1 GPa to 3.1 GPa both for compression and decompression cycles. These measurements correspond to the path labeled **B** in **Figure 28** that crosses the Bi – I to Bi – II phase boundary approximately at 2.5 GPa. The significant change and polarity change in the Seebeck coefficient from a value of $-24 \pm 2 \mu\text{V/K}$ to a value of $+19.3 \pm 0.3 \mu\text{V/K}$ with increasing pressure from 2 GPa to 2.7 GPa coincides well with the phase boundary. The same trend is also observed in the decreasing pressure data shown in **Figure 33**; however, there is a significant hysteresis within Bi – I phase during the decompression cycle. The observed hysteresis could be due to unreported cell dynamics upon decompressing, but as the polarity cross-over reproduces the consistent phase boundary around 2.5 GPa, we do not rule out the possibility that the result may indicate an intrinsic thermoelectric hysteresis with pressure, which requires further studies to fully understand. Upon complete decompression, the Seebeck coefficient recovers its initial value observed prior to the Bi – I to Bi – II phase transition.

Measurements performed by Ferdin *et al.* show a similar trend for the Seebeck coefficient as a function of pressure [99]. Although the trend agrees, there is a difference between the values as measured in our experiment when compared to those reported by Ferdin *et al.* [99] comparing our value of $-34 \pm 4 \mu\text{V/K}$ and the published value of Ferdin of $-60 \mu\text{V/K}$. As discussed for the results of the temperature measurements, the differences between the two measurements may be attributed to different experimental conditions.

High-Pressure Thermal Conductivity Measurements

Figure 34 plots the relative change in the thermal conductance as the sample is compressed. Although there is some scatter in the measured data below 2.3 GPa, it seems to follow a linear, generally increasing trend as pressure is increased. The relative thermal conductance is observed to reach a maximum at approximately 2.3 GPa, and then it slowly decreases from the maximum value. This maximum in the relative thermal conductance corresponds reasonably well with the beginning of the phase transition and the onset of the change observed in the Seebeck coefficient measurement as shown in **Figure 34**. Also, the slower decrease observed after 2.5 GPa corresponds with the Bi – I to Bi – II to Bi – III phase transition boundaries. Although these measurements only observe the relative change in the thermal conductance, the correlation with the Seebeck measurements and the phase diagram of Bi imply there may be a change in the thermal behavior of the material as it transitions from the Bi – I through Bi – III phases.

High-Pressure Dimensionless Figure of Merit

Figure 35 is a plot of the calculated dimensionless figure of merit normalized by the largest value as mentioned previously. **ZT** seems to generally decrease in the Bi – I phase (below 2.5 GPa); however, at the Bi – I to Bi – II phase boundary, the relative value for **ZT** seems to increase suddenly. This sudden increase correlates to the changes observed in the Seebeck coefficient, thermal conductivity and resistance measurements and infers that the Bi – II phase may have an increased thermoelectric efficiency as compared to the Bi – I phase at elevated pressures.

Conclusions

The electrical resistance measurements on Bi reveal excellent repeatability and reproducibility of the qualitative behavior of the electrical resistance as pressure is increased. Both the Bi – I to Bi – II and the Bi – II to Bi – III phase boundaries correlate very well with the changes observed in the electrical resistance measurements and the trend in these measurements agrees very well with previously published results. Our measurements on Bi sample show a gradual decrease in the absolute value of the Seebeck coefficient with pressure, in agreement with a similar trend reported in the literature previously. Also, the trend observed in the Seebeck coefficient measurements performed with increasing pressure for the Bi sample across the Bi – I to Bi – II phase boundary agrees well with the reported behavior of bismuth with increasing pressure. The relative change in the thermal conductance as the sample is compressed corresponds well with the phase boundary and the observations made in the Seebeck coefficient measurements. A change in slope is observed in the relative thermal conductance measurement, which also appears in the relative change in the dimensionless figure of merit near and across the phase boundary.

Chapter IV – Sample Results: PbTe

Overview

This chapter will discuss the results of our measurements with the system on the classic thermoelectric material PbTe. PbTe has been proven to be an incredibly important thermoelectric material due to the ability to optimize its thermoelectric properties for power generation. The PbTe system was chosen as a prime candidate for further study to test the capabilities of our system. PbTe has shown significant promise for increased thermoelectric efficiency in thermoelectric materials [101], and as such, we wanted to explore the properties of this material using our apparatus.

A small piece of an ingot of PbTe was ground finely into a powder using an agate mortar and pestle. After grinding the ingot of PbTe, the powder was put into the same 2 mm pellet die as used for the Bi experiments and a 2 mm diameter and approximately 500 μm thick pellet of PbTe was produced to be used as the sample. The Seebeck coefficient of PbTe was explored over the range shown in **Figure 36** where arrows indicate the temperature and pressure pathways taken in the measurements.

Figure 37 displays the voltages measured for the PbTe sample in a region devoid of a phase transition. The slight curvature at temperature below 315 K is likely due to the small temperature difference across the sample creating very small voltages. After 315 K, the voltages follow a linear trend similar to the Bi measurements. With these voltage measurements, the Seebeck coefficient can be calculated using **Equation 7**.

High-Pressure Thermoelectric Measurements

Isobaric Seebeck Coefficient of PbTe

Figures 38(a) and **Figure 38(b)** display the isobaric Seebeck coefficient measurements performed on the PbTe sample at 1.0 GPa and 2.1 GPa which correspond to the pathways indicated in **Figure 36** labeled **E** and **F**, respectively. The gradual increase in the absolute value of the Seebeck coefficient agrees with the trend reported in literature for PbTe and no phase transition is expected at these pressures and temperatures. The hysteresis observed in the PbTe sample is similar to the hysteresis previously mentioned in the Bi sample.

The softening of the boron epoxy gasket with increasing temperature possibly leads to a small variation in pressure or stress state of the sample as temperature is then decreased. The scatter observed in both measurements below 310 K is due to the small ΔT across the sample yielding a small voltage across the sample. This smaller voltage has a larger error and this leads to a larger scattering of the data points.

High-Pressure Electrical Resistivity Measurements

The result of electrical resistivity measurements as a function of increasing pressure is depicted in **Figure 39** from 2 GPa to 5.5 GPa at 325 K. The electrical resistivity has a distinct decreasing trend which is favorable for the thermoelectric efficiency for this material as a decreasing electrical resistivity directly implies an increasing electrical conductivity. Measurements upon decompression were not available since the thermocouples failed at the highest pressure (~5.5 GPa). As PbTe is known to undergo a phase transition at 6 GPa, higher pressure measurements would have been ideal, but due to limitations of the thermocouples, it can

be difficult to reach higher pressures [75,76]. However, the measurements can be compared to the published results of Ovsyannikov *et al* which reports a similar trend in the electrical resistivity measurements [101]. The overall decrease in the measurements of Ovsyannikov *et al*. is larger, yet the continual decrease in electrical resistivity as pressure is increased is similar between both measurements.

High-Pressure Seebeck Coefficient Measurements

The results of the isothermal measurement of the Seebeck coefficient from 2 GPa up to 5.5 GPa at 325 K is depicted in **Figure 40**. The Seebeck coefficient measurements can be directly compared to the reported results of Ovsyannikov *et al* [101]. The trend observed in both cases is a gradual decrease in the absolute value of the Seebeck coefficient from 2.0 GPa to 5.0 GPa. Ovsyannikov *et al* observed a turn-over in the Seebeck coefficient after 5.0 GPa and a gradual increase in the absolute value possibly correlating with the known structural phase transition to an orthorhombic crystal structure near 6 GPa [101]. Our measurements of the Seebeck coefficient do not observe this turn-over trend reported in the literature. It is possible due to different compression conditions (ie. hydrostatic vs. non-hydrostatic) that the phase transition is delayed in our measurements. However, further measurements of this sample at pressures greater than 6 GPa would certainly be highly desired.

Also, the absolute value as measured by Ovsyannikov *et al*. at 2.5 GPa is approximately -100 $\mu\text{V/K}$ with a 20% relative error reported compared with our value of $-62 \pm 1 \mu\text{V/K}$ [101]. Although the values differ significantly, the error reported by Ovsyannikov is about 20% on their Seebeck coefficient measurements is larger than the error on our measurements, which are typically 5% or less. It should be noted that the samples studied by Ovsyannikov were single

crystals and the measurements performed in this study were on polycrystalline samples, which may lead to differences in the absolute measurements of the Seebeck coefficient [101].

High-Pressure Thermal Conductivity Measurements

The relative changes in the thermal conductivity measured as a function of pressure from 2.0 GPa to 5.5 GPa at 325K is displayed in **Figure 41**. A linear increasing trend is observed over the entire pressure range. While this increasing trend is not favorable for the thermoelectric efficiency, it is not a surprising trend. As there are no known structural phase transitions in PbTe below 6 GPa, this monotonic trend of increasing thermal conductivity is reasonable. The observations of a possible turn-over in the Seebeck coefficient after 5.0 GPa – 6.0 GPa by Ovsyannikov *et al* indicating possibly favorable thermoelectric behavior in the high-pressure phase of this material may indicate a possibility the thermal conductivity could respond more favorably in that region when compared to the measurements observed in this study [101]. The overall increase observed in the thermal conductivity is approximately 25%.

High-Pressure Dimensionless Figure of Merit, ZT

Combining the measurements of the thermoelectric properties of PbTe as discussed in the previous sections and using them to calculate **ZT** as given in **Equation 1** allows determination of the high-pressure behavior of the thermoelectric efficiency for PbTe. Again, the values have been normalized to the lowest pressure value due to the difficulties obtaining proper values of thermal conductivity at high-pressures, and the relative changes in the **ZT** value of PbTe as a function of increasing pressure is plotted in **Figure 42**. It is clear there is a very steady increase in the relative **ZT** value as pressure is increased despite the increase in thermal conductivity and decrease in absolute Seebeck coefficient for PbTe. The strong decrease in the electrical

resistivity of this material leads to a significant rise in the thermoelectric efficiency. This trend correlates well with the observed increase in power factor as described by Ovsyannikov *et al* [101]. The inclusion of the behavior of the thermal conductivity at high-pressure conditions while still obtaining an increase in **ZT** indicates great promise for PbTe at these conditions. It is also important to note that a pressure-induced structural phase transition occurs near 6 GPa for PbTe and future endeavors should possibly focus on the high-pressure phase of this material.

Conclusions

The measurements of the high-pressure thermoelectric properties of PbTe are an important check of the system's capabilities to measure these properties on proper thermoelectric materials. As PbTe is among some of the more important thermoelectric materials and has received a great deal of research [13,28,55,101], this material was a proper choice for establishing feasibility of this system alongside the measurements on elemental bismuth. Measurements of the Seebeck coefficient as temperature is increased revealed an increase in the absolute value as is expected based on literature at both 1.1 GPa and 2.1 GPa and the absolute value of the Seebeck coefficient as a function of increasing pressure is observed decreasing. The electrical resistivity is observed to decrease, thus increasing the electrical conductivity as pressure is increased. Measurement of the relative changes in the thermal conductivity result in an observation of a steady increase in thermal conductivity as pressure is increased. Thus, the electrical conductivity leads to a favorable effect on the thermoelectric efficiency as the relative change in **ZT** value is observed to increase over the entire pressure range. Overall, these measurements are extremely favorable for the effectiveness of this system in measuring thermoelectric properties at high-pressure and high-temperature conditions.

Chapter V – Sample Results: SnTe

Overview

This chapter and the next will discuss the results on the thermoelectric material SnTe and Mn-doped SnTe ($\text{Sn}_x\text{Mn}_{1-x}\text{Te}$). As briefly discussed in the introduction to this dissertation, lead chalcogenides are one of the leading classes of TE materials. However, there are significant concerns with toxicity of lead chalcogenides especially in consideration in large-scale commercial applications. One such alternative is SnTe which crystallizes in the same cubic $Fm-3m$ structure [102-106] and has a similar band structure to PbTe suggesting promising TE behavior [107-111]. However, pure SnTe has poor TE performance because of intrinsic Sn vacancies which lead to a high thermal conductivity and a low Seebeck coefficient [112]. In recent years, chemical doping and alloying have been attempted to enhance the performance, which have yielded ZT values as high as 1.4 [27,113-118]. Tan *et al* alloyed MnTe and SnTe observing a very large increase in the Seebeck coefficient reaching a value of 230 $\mu\text{V/K}$ at 900 K [118]. Pure SnTe undergoes a pressure-induced structural phase transition to an orthorhombic phase [102-106], which has received more attention in recent years attempting to clarify the convoluted mixture of phases that have been observed [106]. We report a drastic increase of the Seebeck coefficient of SnTe over 200% with application of pressure up to 4.5 GPa at 330 K. This large increase in thermopower corresponds with a known pressure-induced structural phase transition from the ambient $Fm-3m$ cubic crystal structure to a complex mixed phase consisting of a $Cmcm$, $Pnma$, and a GeS-structure [106]. In addition to the huge increase in the Seebeck coefficient, an increase in the electrical resistance and a decrease of the thermal conductivity were also observed above 3 GPa. Despite the increase in electrical resistance, the dramatic

increase in the Seebeck coefficient eventually leads to a giant increase in **ZT** up to 350% because its squared contribution.

Sample Synthesis

SnTe was synthesized using solid-state reaction methods and annealing processes. Appropriate stoichiometric quantities of high-purity elemental powders purchased from Sigma Aldrich (99.99%) of the constituents were weighed and finely ground with an agate mortar and pestle to ensure thorough mixing. This powdered mixture was then made into pellets using a 6 mm die-press. The sample was then placed into a quartz tube which had been evacuated to 10^{-5} torr and flushed several times with high-purity Ar gas and then sealed with a propane-oxygen torch. The sealed quartz tubes were placed into a computer controlled muffle furnace which heated the sample to 1150 °C in 12 hours. After 24 hours at 1150 °C, the sample was removed from the furnace and immediately cooled to room temperature using a liquid nitrogen bath to quench the quartz tube. The ingot was then removed from the quartz tube and ground with an agate mortar and pestle again in order to create a fine powder useable for powder X-ray diffraction measurements. The phase purity of the resultant compounds was examined with a Bruker D-8 Advance powder X-ray diffractometer with a Cu K- α X-ray source ($\lambda = 1.5416 \text{ \AA}$) with a Ni filter installed. The lattice parameter as determined by performing a LeBail refinement on SnTe is $a = 6.292 \text{ \AA}$. The sample was confirmed to be single-phase with $Fm-3m$ symmetry which agrees with the literature [102-106]. The results of these XRD patterns are displayed in **Figure 43**.

High-Pressure Thermoelectric Measurements

Energy-Dispersive X-ray Diffraction

The evolution of the energy-dispersive X-ray diffraction patterns obtained *in-situ* throughout our measurements are displayed in **Figure 44**. The MgO EDXRD spectra at each pressure are shown as a reference to indicate small MgO peaks in the sample EDXRD patterns. Due to the diameter of the sample (2 mm), EDXRD patterns cannot be obtained at the center of the sample due to signal attenuation. Instead, the EDXRD patterns are obtained by focusing on the sample edge in order to minimize attenuation and maximize sample signal. Pressure determination is also performed near the edge of the sample by focusing on the MgO ring surrounding the 2 mm diameter sample. A consequence of collecting the EDXRD data at the edge of the sample is the MgO ring situated around the sample contributes diffraction peaks to the spectra as is observed in our SnTe EDXRD patterns. Since the MgO pressure and sample EDXRD are collected at the sample edge there is a small 0.1 GPa to 0.3 GPa pressure differential across the 2 mm diameter of the sample leading to a slightly lower pressure at the sample edge when compared to the center of the sample.

There is little change in the EDXRD pattern for the sample below 3.5 GPa; however, at 3.7 GPa, the appearance of small shoulder peaks is observed indicating the evolution of a secondary phase. These small peaks are indicated by diamonds **Figure 44**, and as pressure is increased past 3.7 GPa, more peaks develop. The pressure of 3.7 GPa corresponds very well with the range of pressures discussed in the literature as the onset pressure for structural transformation for this material and correlates well with the electrical and thermal property measurements performed simultaneously to our EDXRD as discussed in the main text.

Radiography Sample Thickness Measurements

Sample thickness as a function of pressure is determined by use of radiography imaging, an example of which is depicted in **Figure 45(a)**. From determining the number of pixels between the top and bottom edge of the sample, a measurement of the thickness is calculated by using a pre-calibrated 0.95 $\mu\text{m}/\text{pixel}$ conversion. An example intensity plot as a function of pixels is shown in **Figure 45(b)** which corresponds to a thickness of 570 μm for the sample at 2.2 GPa. A plot of the sample thickness as determined by this technique is displayed in **Figure 46**. As is expected, there is a continuous decrease in the sample thickness for SnTe with increasing pressure and these values are used in determination of the electrical resistivity and thermal conductivity.

High-Pressure Electrical Resistivity Measurements

The results of the electrical resistance measurement as a function of pressure is shown in **Figure 47**. The electrical resistance is observed to decrease steadily up to 3.2 GPa at which it reaches a minimum value with a decrease of approximately 12% from the 1 GPa value. A calculation of the resistivity based on the electrical resistance measured and a determination of the sample dimensions through use of radiography imaging yields a value at 1 GPa of $8.3 \times 10^{-4} \Omega - \text{cm}$. An example radiography image taken at 2.2 GPa is displayed in **Figure 45(a)** along with the intensity profile in **Figure 45(b)** which is used to determine the sample thickness. Sample thickness as measured from the radiography imaging as pressure is increased is depicted in **Figure 46**. Ambient pressure and temperature measurements in the literature have reported values of $1 \times 10^{-4} \Omega - \text{cm}$ [27,113-118]. This difference may be attributable to the lack of an

ideal 4-probe electrical resistivity measurement set-up with this apparatus. A total increase of near 15% from the minimum at 3.2 GPa is observed at 4.2 GPa.

As SnTe is expected to undergo a pressure-induced structural phase transition between 1.8 GPa and 4.1 GPa [102-106], this marked change in the electrical resistance correlates very well with this structural transition. Energy-dispersive X-ray diffraction (EDXRD) data obtained *in-situ* provides corresponding evidence of this structural phase transition. **Figure 44** displays selected EDXRD spectra and the appearance and disappearance of several peaks from 3.7 GPa to 4.5 GPa indicates the pressure-induced structural transformation. Since the sample EDXRD is measured at the edge of the sample, the slight variation in onset pressure when comparing the *in-situ* EDXRD patterns to the electrical resistance response is likely because of pressure difference between the center of the sample and the edge.

The mechanism for the decrease in electrical resistance in the cubic $Fm-3m$ crystal structure is possibly caused by a decrease in the band-gap as is expected for binary chalcogenides such as PbTe, PbS, and others [20,38,107,108,119-123]. Whereas, the subsequent increase observed in our experiments may be directly correlated to the structural phase transition as related materials such as PbTe reveal positive effects to thermopower with compression [101].

A similar trend in the electrical resistance has been previously reported indicating a decrease below 1.8 GPa, and then an increase by almost 300%. After this rise, the electrical resistance was observed to again decrease as pressure was applied further [103]. We do not observe this decrease above 3 GPa nor quite as significant of a rise in the resistance. However, these discrepancies may be attributed to different compression conditions between both experiments.

High-Pressure Seebeck Coefficient Measurements

Seebeck coefficient for SnTe is plotted as a function of pressure in **Figure 48**. Between 1 GPa and 3.2 GPa, the Seebeck coefficient increases by a small amount from a value of 38 ± 3 $\mu\text{V/K}$ at 0.9 GPa to 40 ± 2 $\mu\text{V/K}$ at 3.0 GPa as depicted in **Figure 48**. Upon crossing the phase boundary near 3.2 GPa, the Seebeck coefficient begins to dramatically increase from a value of 40 ± 2 $\mu\text{V/K}$ in the ambient phase to a value of 91 ± 2 $\mu\text{V/K}$ near 5 GPa. This is an increase of 230% in the thermopower of SnTe in the mixed intermediate phase. The gigantic increase in the Seebeck coefficient may be understood based on calculations performed which predict a sharp increase in the Seebeck coefficient below 3 GPa, which is then expected to decrease with further application of pressure for both n-SnTe and p-SnTe [124]. It is important to note that these calculations do not take into account the structural phase transition which may contribute to the pressure ranges not matching precisely [124].

High-Pressure Thermal Conductivity Measurements

The results of the measurement of relative changes in the thermal conductivity are shown in **Figure 49**. The thermal conductivity is observed to steadily increase below 3.5 GPa and upon further compression, decrease. This turnover in the trend correlates well with the behavior observed in the other TE properties and the known structural phase transition. It is known that alloying and chemical doping typically results in a decrease in the thermal conductivity of SnTe, which may also be related to direct changes to the lattice by means of applying chemical pressure. In addition, upon undergoing structural phase transition, SnTe tends towards a more complicated structure and the hindering of the lattice contribution to thermal conductivity in this

less symmetric crystal structure may lead to the decreasing trend observed above 3.2 GPa [40,119,120].

High-Pressure Dimensionless Figure of Merit, ZT

Figure 50 depicts the relative changes in the ZT as a function of pressure. In **Figure 50**, it is observed that ZT remains steady below 3 GPa and starts to increase above 3 GPa, correlating with the property changes observed in the measured TE properties. The increase continues until the maximum pressure reached in the present study, 4.2 GPa. The increase in the value is almost 350% mostly due to the very large increase in the Seebeck coefficient, which is squared for its contribution to the ZT . Based on the marked slope of this increase, it is possible to anticipate this trend may continue well into the SnTe – II phase according to the results of Kafalas *et al*, where the electrical resistance decreases upon further pressure increase into the high-pressure phase of SnTe [103]. Additionally, the calculations of Xu *et al* discuss the high-pressure behavior of ZT and conclude modest pressure below 5 GPa may be favorable to TE efficiency [124]. An important note is in their calculation of ZT , a constant thermal conductivity value corresponding to the value for PbTe of 2 W/mK is used in their ZT calculations [124]. No attempt is made to account for changes in thermal conductivity due to pressure [124]. Although absolute ZT values of pure SnTe are typically very low when compared to state of the art TE materials such as SnSe [40], doped lead chalcogenides [20,38,119,122,123], and others, the drastic relative increase in ZT is promising for alloyed SnTe materials with higher starting ZT values and possibilities in quenching this high-pressure phase.

Conclusions

In conclusion, we have performed simultaneous measurement of the high-pressure electrical resistance, Seebeck coefficient, relative changes in the thermal conductivity, overall behavior of the dimensionless figure of merit, **ZT**, and structural behavior of SnTe for the first time. We report a giant pressure-induced increase in the Seebeck coefficient of greater than 200% which leads to a massive enhancement in the trend of **ZT** with an increase of 350% being observed. These results correlate directly with the known pressure-induced structure phase transition in SnTe from the cubic $Fm-3m$ ambient pressure crystal structure to an orthorhombic symmetry discussed throughout the literature and observed in our *in-situ* EDXRD spectra. Although this phase transition is reversible, identifying potential methods of quenching the high-pressure orthorhombic phase of SnTe may be a promising route to further increasing the potential applications of SnTe as a replacement for the more toxic lead chalcogenides. If this high-pressure phase can be quenched to ambient pressure and temperature conditions, it may be beneficial to explore doping and alloying processes already undertaken with cubic SnTe as further enhancements to the TE properties that have been already identified with these processes.

Chapter VI – Sample Results: $\text{Sn}_{1-x}\text{Mn}_x\text{Te}$ ($x = 12\%$)

Overview

This chapter will discuss the sample synthesis and results of the measurements performed on $\text{Sn}_{1-x}\text{Mn}_x\text{Te}$ ($x = 12\%$). As discussed in the previous chapter, SnTe is a promising alternative to lead-based chalcogenide thermoelectric materials, but due to issues with low Seebeck coefficient at ambient conditions in its purest form, studies of its alloyed and chemically doped forms are imperative. With the promising results observed in pure SnTe as described in the last chapter, it is only fitting to attempt similar measurements on alloyed forms of SnTe. As such, this chapter discusses the high-pressure structural, and thermoelectric measurements of $\text{Sn}_{1-x}\text{Mn}_x\text{Te}$ ($x = 12\%$).

Sample Synthesis

$\text{Sn}_{1-x}\text{Mn}_x\text{Te}$ was synthesized using solid-state reaction methods and annealing processes similarly to the pure SnTe sample. Appropriate stoichiometric quantities of high-purity elemental powders (Sn, Mn, Te) purchased from Sigma Aldrich (99.99%) of the constituents were weighed and finely ground with an agate mortar and pestle to ensure thorough mixing. The process of mixing, quartz-tube sealing, heating process, and sample preparation for XRD measurements is described in the previous chapter and is identical to the process for pure-SnTe. The phase purity of the resultant compound was examined with a Bruker D-8 Advance powder X-ray diffractometer with a Cu K- α X-ray source ($\lambda = 1.5416 \text{ \AA}$) with a Ni filter installed. The lattice parameter as determined by performing a LeBail refinement on $\text{Sn}_{1-x}\text{Mn}_x\text{Te}$ is $a = 6.2676 \text{ \AA}$. The sample was confirmed to be single-phase with $Fm-3m$ symmetry which agrees with the literature [102-106]. The results of these XRD patterns are displayed in **Figure 51**. As evidenced by the

plot displayed in **Figure 51**, it is evident that there is excellent agreement between the calculated LeBail refinement and the observed XRD diffraction data by comparing the lines representing the calculated and observed data. In addition, the bottom solid line represents the difference between the calculated and observed data, and this line reveals minimal deviation between these.

High-Pressure Structural Measurements

High-Pressure Powder X-ray Diffraction

The evolution of the XRD patterns with increasing pressure is displayed in **Figure 52**. The measurements were carried out from 0.32 GPa to 30.7 GPa and there is clear evidence of a pressure-induced structural phase transition as pressure is increased. The XRD patterns between 0.32 GPa and 5.06 GPa have no indication of structural phase transition and remain in the ambient *Fm-3m* crystal structure. This ambient *Fm-3m* crystal structure phase for $\text{Sn}_{1-x}\text{Mn}_x\text{Te}$ ($x = 12\%$) remains stable until slightly higher pressures than pure-SnTe which has been observed to undergo a pressure-induced structural phase transition near 4 GPa as previously discussed in the previous chapter. Both the EDXRD measurements presented in the previous chapter displayed in **Figure 44**, and previously published literature by Zhou *et al* and others have clearly observed a structural phase transition to an orthorhombic crystal structure between 2 GPa and 4 GPa [106]. The increase in onset pressure for this phase transition as observed in our measurements is may be related to the introduction of Mn into the SnTe lattice. As Mn has a smaller atomic radius than Sn, this causes the unit-cell volume to decrease with the introduction of Mn. This difference in atomic size and reduction of the unit-cell volume indicates a positive chemical pressure imposed on the sample. Thus, it would be expected if the reduction in unit-cell volume is the only factor, the onset pressure for this transition may be lower. We observe an increase in the onset pressure

of the structural phase transition, thus another mechanism may be playing an important role with the introduction of Mn into the SnTe lattice.

With further increase of pressure past 5.06 GPa, it is very clear a significant change in the XRD pattern takes place. Several peaks appear between 6° and 8° two-theta in addition to many peaks appearing after 8° two-theta as is clearly visible in **Figure 52**. This structure seems to remain stable up to the maximum pressure of 30.7 GPa, as there only very small changes in the XRD patterns up to this pressure. Using the lattice parameters and crystal structure suggested by Zhou *et al*, the subsequent XRD patterns above 30.7 GPa were fit to a *Pnma* crystal structure [106]. For each XRD pattern over the entire pressure range, a LeBail refinement was performed. For the XRD patterns corresponding to pressures between 0.32 GPa and 5.06 GPa, the refinement performed fits the observed data to the ambient *Fm-3m* crystal structure. For the XRD patterns corresponding to pressures above 5.06 GPa, the refinement performed fits the observed data to the *Pnma* crystal structure as observed in pure-SnTe discussed at length in the literature [106].

From these LeBail refinements, the unit-cell parameters **a**, **b**, and **c**, are extracted for both the low pressure and high pressure phases and these values are displayed in **Table 3**. A plot of the lattice parameters as a function of increasing pressure for the low pressure phase is plotted in **Figure 53(a)** and the lattice parameters as a function of increasing pressure for the high pressure phase is plotted in **Figure 53(b)**. The expected decreasing trend is observed for both the low pressure and high pressure phases. For the high pressure *Pnma* phase, the rate of decrease for each lattice parameter can be compared by using the values in **Table 3**. For the lattice parameter, **a**, a $\sim 7.5\%$ decrease is observed over the pressure range for the *Pnma* phase. For the **b** axis, an $\sim 5.9\%$ decrease is observed and for the **c** axis, an $\sim 5.0\%$ decrease is observed. As is clearly

evident from a comparison of these percent decreases over the pressure range, the **a** axis decreases at a larger rate than the other two axes.

Equation of State Analysis

For both the low and high pressure phases, the unit-cell volume can be calculated from the lattice parameters displayed in **Table 3**. To calculate the unit-cell volume for the low pressure ambient *Fm-3m* crystal structure, the lattice parameter is cubed and this value for each corresponding pressure is displayed in **Table 3**. For the high pressure phase, the unit-cell volume for *Pnma* is calculated by the product of the three lattice parameters as displayed in **Figure 54**. The result of this calculation for the unit-cell volume of the *Pnma* crystal phase is displayed in **Table 3**. As discussed previously, valuable information can be extracted from a comparison of the unit-cell volume as pressure is increased via use of the BM-EOS to determine the bulk modulus and the change in the bulk modulus as pressure is increased. **Equation 13** describes this EOS in detail and the parameters that are fit to the observed data are V_0 , B_0 , and B'_0 . A plot of the unit-cell volume as a function of increasing pressure for both the low and high pressure phases is displayed in **Figure 54** with fits to a 2nd-order BM-EOS displayed as well for each phase. A 7% volume decrease is observed at the onset of the pressure-induced phase transition at 6.9 GPa. This volume collapse is larger than for pure-SnTe which has been observed as an approximate 3% decrease in volume at 4.1 GPa [106]. However, this larger volume collapse may be related to the higher onset pressure for the phase transition observed for the Mn-doped SnTe when compared to the pure-SnTe.

The fit parameters for the 2nd-order BM-EOS for the $\text{Sn}_{1-x}\text{Mn}_x\text{Te}$ sample are displayed in **Table 4**. The fitting yields values for the low pressure *Fm-3m* of $V_0 = 244 (4) \text{ \AA}^3$, $B_0 = 48 (14)$

GPa, and \mathbf{B}_0 is fixed at 4 for the 2nd-order BM-EOS. These values compare fairly well with literature values of $\mathbf{V}_0 = 253 \text{ \AA}^3$ and $\mathbf{B}_0 = 50 \text{ GPa}$ for pure-SnTe with a smaller unit-cell volume being observed for the Mn-doped SnTe as expected. For the high pressure *Pnma* phase, the fitting to the 2nd-order BM-EOS yields values of $\mathbf{V}_0 = 228 (3) \text{ \AA}^3$ and $\mathbf{B}_0 = 59 (5) \text{ GPa}$ which compare fairly well with literature values for pure-SnTe in the high pressure phase which are $\mathbf{V}_0 = 244 \text{ \AA}^3$ and $\mathbf{B}_0 = 50 \text{ GPa}$. The lower initial volume parameter in our measurements is expected as the volume collapse observed in our experimental data was larger than for pure-SnTe and the bulk modulus in our experiments is observed to be larger indicating less compressibility of the Mn-doped SnTe sample when compared to pure-SnTe.

High-Pressure Thermoelectric Measurements

Radiography Sample Thickness Measurements

Figure 55 displays the evolution of the sample thickness through a series of radiography images taken for the Mn-doped SnTe sample. The images are at the left edge of the sample which is chosen for these images because it is simplest for direct visual comparison. By performing the analysis as described in previous sections, the sample thickness can be extracted from these radiographic images. These measurements are imperative to understand the evolution of the electrical resistivity and the thermal conductivity in order to eliminate geometric influences on these parameters. **Figure 56** displays the determined sample thickness for $\text{Sn}_{1-x}\text{Mn}_x\text{Te}$ ($x = 12\%$) as a function of increasing pressure. There is a generally decreasing trend in the sample thickness as pressure is increased. The fairly consistent slope over the entire pressure range indicates a fairly well compressed and densified sample pellet within the sample cell assembly.

High-Pressure Electrical Resistivity Measurements

Figure 57 depicts the results of the high pressure electrical resistivity measurements performed on the Mn-doped SnTe sample. In contrast to the results discussed for pure-SnTe, the electrical resistivity is observed to continually decrease over the pressure range measured in these experiments. A slight deviation is observed near 3.5 GPa which does correlate well with the known structural phase transition in pure-SnTe. However, as previously discussed in this chapter, the XRD data for the Mn-doped SnTe does not indicate this phase transition occurring until higher pressure (6.92 GPa). It is possible this slight deviation is an indication that the beginning of the structural phase transition is in progress, but additional measurements would be required to confirm this possibility. As the structural phase transition does not reveal itself readily in the XRD patterns until higher pressures as discussed in the previous sections, it is unlikely this may be the cause. Nonetheless, the behavior of the electrical resistivity for $\text{Sn}_{1-x}\text{Mn}_x\text{Te}$ ($x = 12\%$) is vastly different than the behavior observed for pure-SnTe. The overall decrease is fairly large over the pressure range measured as it is more than a two-fold decrease in the electrical resistivity which is very favorable for the thermoelectric efficiency of this material.

High-Pressure Seebeck Coefficient Measurements

The Seebeck coefficient variation as a function of increasing pressure is depicted in **Figure 58** for the Mn-doped SnTe sample. A fairly steady increase in the Seebeck coefficient is observed over the pressure range from 2 GPa to 5 GPa with a slight slowing of the increase near 4.5 GPa. Comparing this behavior to that of pure-SnTe, it is vastly different. The Seebeck coefficient of pure-SnTe was observed to remain very constant from 1 GPa to 3 GPa and then increase drastically as the sample underwent a structural phase transition as discussed previously;

whereas, the Mn-doped SnTe increases fairly monotonically with a small slowing of the increase. The significant difference in Seebeck coefficient between the pure-SnTe and the Mn-doped SnTe is likely correlated to the higher onset pressure for structural phase transition observed for the Mn-doped sample. Despite the lack of similar response to pressure for the Seebeck coefficient, the lower pressure phase, *Fm-3m*, for Mn-doped SnTe seems to respond favorably to pressure significantly more than for pure-SnTe indicating that Mn doping is favorable at both ambient pressures as reported in existing literature [106] and at high-pressure as observed in our experiments. The Seebeck coefficient for the high-pressure phase, *Pnma*, has an unknown response for the Mn-doped sample.

High-Pressure Thermal Conductivity Measurements

Figure 59 displays the results of the thermal conductivity measurements with increasing pressure normalized to the lowest pressure value for $\text{Sn}_{1-x}\text{Mn}_x\text{Te}$ ($x = 12\%$). A clear increase in the thermal conductivity is observed over the entire pressure range measured. Unlike with pure-SnTe, there is no indication of a decrease in thermal conductivity past 3.5 GPa corresponding to the structural phase transition. As the structural phase transition is not observed to occur until higher pressure for the Mn-doped SnTe sample, this may be a reason the decrease is not observed for this sample. The increase observed is a 35% increase from 2 GPa to 5 GPa. As **Equation 1** suggests, this trend in the thermal conductivity is unfavorable for the overall thermoelectric performance of this material at high pressure conditions. However, this increase is significantly smaller than the change observed in the electrical resistivity, which may indicate an overall favorable effect on the thermoelectric performance due to pressure.

High-Pressure Dimensionless Figure of Merit, ZT

Figure 60 depicts the normalized dimensionless figure of merit as a function of increasing pressure for the Mn-doped SnTe sample. As discussed in previous chapters, ZT is calculated by use of **Equation 1** using the values obtained in each of the previously described measurements. A large increase in ZT is observed over the pressure range studied. The increase over the pressure range of 2 GPa to 5 GPa is observed to be over 250% when comparing the highest pressure value to the lowest pressure value. As the thermal conductivity shown in **Figure 59**, increases over the entire pressure range, this increase in ZT is definitely correlated to the increase in Seebeck coefficient and the decrease in the electrical resistivity. The increase of 14% in the Seebeck coefficient over this pressure range significantly aids the ZT value as the Seebeck coefficient has a squared contribution to ZT as **Equation 1** details. However, the decrease of over a factor of two for the electrical resistivity shown in **Figure 57** is the leading physical property leading to the large ZT increase observed. As Mn doping has been established as a viable method to increase the thermoelectric efficiency of SnTe as describe by Tan *et al* [118], it is valuable to further understand the behavior of this material at extreme pressure conditions.

Conclusions

We have performed synthesis and high-pressure XRD measurements to understand the high-pressure structural properties of $\text{Sn}_{1-x}\text{Mn}_x\text{Te}$ ($x = 12\%$). In addition, we have performed high-pressure thermoelectric property measurements using the PE thermoelectric cell assembly as described in previous sections. A single-phased high quality sample was synthesized using solid state reaction means and characterized by use of ambient pressure and temperature XRD measurements. These measurements verified an $Fm-3m$ crystal structure similar to pure-SnTe as

discussed previously. High-pressure XRD measurements were performed up to 30.7 GPa and a pressure-induced structural phase transition was observed from the ambient $Fm-3m$ crystal structure to $Pnma$ crystal structure at 6.92 GPa. This onset pressure for the structural transition is at a higher pressure than for pure-SnTe which has been reported to undergo a structural phase transition between 2 – 4 GPa [102-106]. Both the ambient and high-pressure phases were analyzed and the lattice parameters and unit-cell volume was determined for all pressures. This data was then fit to a 2nd-order BM-EOS yielding values for the bulk modulus similar, yet less compressible than for pure-SnTe [106].

The high-pressure thermoelectric property measurements revealed a large increase in ZT over the pressure range measured (2 – 5 GPa). This increase is directly related to the large decrease in electrical resistivity observed over this pressure range easily counteracting the increase observed in the thermal conductivity. The Seebeck coefficient was also observed to increase over the pressure range quite differently than for pure-SnTe. The thermoelectric properties of the Mn-doped SnTe did not seem correlated to any structural phase transition due to the higher onset pressure of the expected structural transition.

Chapter VII – Sample Results: TiCoSb

Overview

This chapter and the next chapter will discuss the results on the half-Heusler thermoelectric materials TiCoSb and TiNiSn. Half-Heusler compounds are of significant interest to the thermoelectric community due to their typically very large Seebeck coefficient and good electrical conductivity leading to exceptionally large power factors (α^2/ρ) [125-129]. Studies of the band-structure of half-Heusler type materials reveal an energy gap ranging from 0.1 – 0.9 eV suggesting the large Seebeck coefficient may arise as a consequence of this narrow band gap [130-135]. However, these materials also tend to have large thermal conductivity (10 – 20 W/mK) which limits their effectiveness as an ideal thermoelectric material [136,137]. In addition to methods focusing on the reduction of thermal conductivity through chemical substitution and alloying, other methods have focused on optimizing the Seebeck coefficient and electrical conductivity [125-129].

One half-Heusler compound of particular interest because of its very large Seebeck coefficient at ambient temperature conditions and good electrical conductivity is TiCoSb. TiCoSb belongs to a family of half-Heusler alloys with the general chemical formula MCoSb (M = Ti, Hf, Zr). This class of thermoelectric materials has received a great deal of recent interest due to their exceptionally high power factors as previously mentioned and their robust structural properties [138-142]. Specifically, TiCoSb both doped and un-doped have reached values as large as $-500 \mu\text{V/K}$ at 300 K for lightly Sb rich samples while the pure TiCoSb sample reported to have a value of $-265 \mu\text{V/K}$ [140]. Theoretical studies have attempted to identify optimal doping concentrations to increase the thermoelectric efficiency of TiCoSb and TiNiSn [141].

Studies such as these can high-light particular pathways for synthesis of half-Heusler alloys with better thermoelectric efficiency. Several researchers have explored the method of alloying and doping in half-Heusler compounds with favorable results. Kawaharada *et al* reported a positive effect on the thermoelectric performance of TiCoSb via niobium and antimony substitution leading to a maximum **ZT** value of 0.11 at 963 K [142]. Since the significant drawback of half-Heusler compounds is typically the thermal conductivity being large when compared to state-of-the-art thermoelectric materials, reduction of the thermal conductivity is extremely important. Sekimoto *et al.* doped the Sb site of TiCoSb with Sn and observed a decrease in the thermal conductivity with an increase in Sn content [139]. The maximum **ZT** value obtained in these experiments was 0.030 at 988 K with 5% Sn doping [139].

The high-pressure structural and TE behavior of TiCoSb has not been explored previously, and as high-pressure plays an important role in the structural and TE properties of materials, determining the effect of pressure on this material is imperative to a full understanding of structure-property relations. Some theoretical results have been published on the high-pressure thermoelectric behavior of TiCoSb by Xu *et al* concluding that although the Seebeck coefficient is predicted to decrease with increasing pressure a rapid increase in the electrical conductivity as pressure is increased may be promising for thermoelectric efficiency [143]. Additionally, theoretical results on the structural properties of TiCoSb at high-pressure have been published which quantify the parameters for a 3rd-order BM-EOS [141]. In order to better understand the structural and thermoelectric behavior at high-pressure conditions, we have performed synthesis, structural characterization, high-pressure powder X-ray diffraction (HPXRD) and high-pressure electrical and thermal measurements on TiCoSb. Specifically, in the HPXRD measurements, we studied the crystal structure of TiCoSb up to 115 GPa. We observed stability of the MgAgAs

type crystal structure of TiCoSb over the entire pressure range. In the high-pressure electrical and thermal experiments we measured the electrical resistance, Seebeck coefficient, relative change in the thermal conductivity, and relative changes to the dimensionless figure of merit, **ZT**, of TiCoSb up to 5 GPa observing an overall negative effect on the thermoelectric efficiency over this pressure range.

Ambient Crystal Structure

Half-Heusler compounds crystallize in the MgAgAs type structure with a typical chemical composition of XYZ, where X and Y are transition metals and Z is an sp-valent element [138,139,144-146]. The crystal structure of TiCoSb consists of three interpenetrating face centered cubic (*fcc*) sub-lattices. Ti and Sb form two sub-lattices which combine to form a rock-salt sub-structure while the third sub-lattice containing Co is displaced by one-fourth of a unit cell along the body diagonal of the rock-salt structure as depicted in **Figure 61**.

Sample Synthesis

TiCoSb was synthesized using arc-melting technique and annealing processes. Appropriate stoichiometric quantities of high-purity elemental powders of the constituents purchased from Sigma Aldrich (99.9%) were weighed and finely ground with an agate mortar and pestle to ensure thorough mixing. This powdered mixture was then made into a pellet using a die-press, which was then placed into a copper hearth and inserted into the chamber of an arc-melting furnace. The chamber was evacuated and re-filled with high-purity Ar gas several times before performing the synthesis. The pellet was reacted several times by creating a high-temperature arc between a tungsten tip and the copper hearth and allowing this arc to melt the pellet for several seconds. The resulting ingot was removed from the copper hearth, re-ground

and re-pelletized. This new pellet was then placed into a quartz tube which had been evacuated to 10^{-5} torr and flushed several times with high-purity Ar gas and then sealed with a propane-oxygen torch. The sealed quartz tube was placed into a muffle furnace at 800 °C for a week. The quartz tube was removed and quickly cooled by placing it into a bath of liquid nitrogen. The phase purity of the resultant compound was examined with a Bruker D-8 Advance powder X-ray diffractometer with a Cu K- α X-ray source ($\lambda = 1.5416 \text{ \AA}$) with a Ni filter installed. The sample was confirmed to be single-phase with the ambient MgAgAs structure which agrees with the literature [138,139,144-146].

Figure 62 depicts the XRD pattern collected at ambient pressure and temperature conditions in a capillary. A full profile Rietveld refinement was performed on the data as indicated in **Figure 62**. The spectrum reveals a single-phase structure which can be indexed to the ambient cubic structure with $F-43m$ (No. 216) space group accounting for all the peaks in the XRD pattern. The Rietveld refinement performed shows good agreement between the observed XRD pattern and the Rietveld modeling as evidenced by the small differences shown in **Figure 62** beneath the XRD pattern. The refined structural unit cell parameters for TiCoSb are $a = b = c = 5.8897(1) \text{ \AA}$, which agrees well with the literature values [144-146]. Atomic positions for all atom locations in the unit cell for the MgAgAs crystal structure are fixed.

High-Pressure Structural Measurements

High-Pressure Powder X-ray Diffraction

The evolution of the XRD diffraction patterns with increasing pressure is depicted in **Figure 63**. An expected shift of the diffraction peaks towards higher two-theta angles is observed as pressure is increased from 1.62 GPa to 115 GPa. Examining the evolution of the

XRD patterns in **Figure 63**, it is observed that all diffraction peaks remain intact with no apparent splitting and no new peaks appear throughout the entire pressure range. As such, each XRD pattern throughout this large pressure range can be indexed well to the ambient pressure and temperature *F-43m* crystal structure indicating the absence of any pressure-induced structural phase transition in TiCoSb up to 115 GPa.

With each XRD pattern indexed to the MgAgAs ambient crystal structure, Le Bail refinement has been performed on the XRD corresponding to all pressures shown in **Figure 63**. From these refinements, the lattice parameter corresponding to each pressure was extracted and is presented in **Table 5**. A plot of the variation in pressure of the lattice parameter is displayed in **Figure 64**, which depicts a smooth decrease in the lattice parameter of TiCoSb over the entire pressure range indicating a reduction in the volume of the unit cell of the MgAgAs crystal structure.

Equation of State Analysis

For the cubic MgAgAs crystal structure, the unit cell volume can be calculated by simply cubing the lattice parameter, **a**, from **Table 5**, which leads to the unit-cell volume parameters displayed in **Table 5**. The unit-cell volume as a function of pressure was fitted to the BM-EOS (**Equation 13**) and the Rose-Vinet EOS (**Equation 14**) to determine the initial volume parameter, the bulk modulus, and the derivative of the bulk modulus as described in a previous section. Variable parameters in **Equation 13** and **Equation 14** are B_0 , V_0 , and B'_0 and are obtained by fitting the collected unit-cell volume versus pressure data. Optimal values obtained by fitting the data in **Table 5** to both EOS are displayed in **Table 6** for both the BM-EOS and the Vinet EOS.

The initial volume parameter as determined from the fit to the BM-EOS and the Vinet EOS, $V_0 = 203 (8) \text{ \AA}^3$ and $V_0 = 203 (2) \text{ \AA}^3$ agree very well with the experimentally determined initial volume extracted from the ambient pressure and temperature XRD pattern displayed in **Figure 65**. A determination of the bulk modulus parameter for both EOS is given in **Table 6** as $B_0 = 166 (6) \text{ GPa}$ for the BM-EOS and $B_0 = 168 (6) \text{ GPa}$ for the Vinet EOS. Experimental measurements of high-pressure structural properties for TiCoSb have not been performed and as such, direct comparisons of the fit parameters obtained from the 3rd order BM-EOS and the Vinet EOS are difficult. However, a few theoretical studies have been performed to predict electrical and thermal behavior of TiCoSb and other half-Heusler alloys at high-pressure conditions as well as a determination of the high-pressure structural behavior of these compounds [141]. Wang *et al* predicts a bulk modulus of 150 GPa for TiCoSb which is lower than our observed value of 166 (6) GPa for the 3rd order BM-EOS and 168 (6) GPa for the Vinet EOS [141]. However, this is a fair agreement between theoretical calculation and experimental results.

High-Pressure Thermoelectric Measurements

Radiography Sample Thickness Measurements

Figure 66 depicts the evolution of the sample thickness as a function of pressure as a series of radiographic images. The images are at the left edge of the sample which is chosen for these images because it is simplest for direct visual comparison. By performing the analysis as described in previous sections, the sample thickness can be extracted from these radiographic images. These measurements are imperative to understand the evolution of the electrical resistivity and the thermal conductivity in order to eliminate geometric influences on these parameters. **Figure 67** displays the determined sample thickness for TiCoSb as a function of

increasing pressure. As is expected, there is a general decreasing trend in the sample thickness as pressure is increased. The fairly consistent slope over the entire pressure range indicates a fairly well compressed and densified sample pellet within the sample cell assembly.

High-Pressure Electrical Resistivity Measurements

The relative variation in the electrical resistivity of TiCoSb as a function of pressure is displayed in **Figure 68**. A sharp decrease in the resistivity of 17.5% is observed between 0.6 GPa and 2.3 GPa with an upturn corresponding to a near 10% increase from the lowest resistivity value between 2.3 GPa and 4 GPa. These values indicate a fairly beneficial response with regards to the TE efficiency of TiCoSb up to 2.3 GPa with a degrading benefit with further pressure application. Theoretical calculations performed by Xu *et al* have predicted an increase in the electrical conductivity as pressure is increased, which initially agrees with our experimental observations [143]. The increase in resistivity as pressure is further increased as 3 GPa may imply a deviation from the theoretical prediction. It is important to note that the pressure specifically calculated in Xu *et al* are much larger than the pressures measured in our experimental study as discussed [143]. The abrupt change in the electrical resistivity does not correlate with any structural phase transition as indicated by the high-pressure XRD data presented in this study. Further studies are required to identify repeatability of this abrupt change in electrical resistivity and to understand it fully.

High-Pressure Seebeck Coefficient Measurements

The high-pressure behavior of the Seebeck coefficient for TiCoSb is depicted in **Figure 69**. It is apparent that there is little to no change in the Seebeck coefficient over the pressure range studied. A slight increase in the absolute value is observed from a value of $-190 \pm 3 \mu\text{V K}^{-1}$

¹ at 0.6 GPa to a value of $-203 \pm 5 \mu \text{ V K}^{-1}$ which corresponds to an approximate 7% increase in the absolute value. Theoretical calculations by Xu *et al* predict a significant decrease in the Seebeck coefficient as pressure is increased up to 30 GPa [143]. As the increase observed in our results is quite small, it is very possible with further application of pressure this predicted theoretical trend would become apparent.

High-Pressure Thermal Conductivity Measurements

Figure 70 depicts the pressure dependence on the thermal conductivity plotted as a normalized (to the lowest pressure data point) thermal conductivity. This normalized plot allows for important information about the trend of the thermal conductivity as pressure is increased. As is very clearly evident in **Figure 70**, the thermal conductivity is observed to increase significantly as pressure is increased over the entire pressure range. However, although the thermal conductivity increases steadily over the entire pressure range, there is a change in the rate of increase over the pressure range. Between 0.6 GPa and 2.3 GPa, the thermal conductivity increases by over 60%, and upon further increase from 2.3 GPa to 4 GPa, only an increase of 20% is observed. This may indicate that with further compression of the TiCoSb sample, the thermal conductivity may reach a maximum value. Despite this slowing in the increase of the thermal conductivity, it is detrimental to the overall TE efficiency of this material.

High-Pressure Dimensionless Figure of Merit, ZT

When the electrical resistivity, Seebeck coefficient, and thermal conductivity measurements are combined, a determination of the dimensionless figure of merit **ZT** is possible through use of **Equation 1**. Due to the lack of absolute value measurements of the electrical resistivity and thermal conductivity as limitations of the experimental set-up, only a normalized

trend in the dimensionless figure of merit is calculated as previously mentioned. **Figure 71** depicts these normalized **ZT** values as a function of pressure for the TiCoSb sample. A small increase in the TE efficiency is observed with a small increase in pressure. However, after this small increase, a generally decreasing trend is observed until the highest pressure measured. Overall, this decrease in **ZT** for TiCoSb is approximately 30% over the 4 GPa pressure range.

Conclusions

We have performed high-pressure angle-dispersive X-ray diffraction measurements on TiCoSb for the first time up to 115 GPa. Additionally, we have performed high-pressure electrical resistance, Seebeck coefficient, relative changes in the thermal conductivity, and overall behavior of the dimensionless figure of merit, **ZT** on TiCoSb up to 4 GPa. We report no evidence of a pressure-induced structural phase transition up to 115 GPa with the *F-43m* ambient crystal structure remaining stable through the entire pressure range measured. The electrical resistance is observed to initially decrease in a favorable fashion until approximately 2.5 GPa. After 2.5 GPa, there is observed a small increase in the electrical resistance possibly indicating changes to the electronic structure not observed in the structural measurements. The Seebeck coefficient remains very flat over the entire pressure range and the thermal conductivity is observed to increase quite rapidly up to 2 GPa and then increase slower. The overall dimensionless figure of merit, **ZT**, is observed to decrease fairly rapidly due to the increase in the thermal conductivity and little change to the Seebeck coefficient with application of pressure.

Chapter VIII – Sample Results: TiNiSn

Overview

This chapter will discuss the results for the half-Heusler compound TiNiSn as discussed briefly in the introductory paragraph in the previous chapter. High-pressure transport property measurements and high-pressure structural measurements were performed on the TiNiSn sample with the described PE sample cell assembly and DACs.

Another important half-Heusler compound for thermoelectric application is TiNiSn. TiNiSn exists as part of a class of interesting intermetallics with a general formula of MNiSn (M = Zr, Hf, Ti) [125-129,147-150]. All of these compounds crystallize in the MgAgAs structure, the same as TiCoSb, and are closely related to the full Heusler alloys MNi₂Sn which are metals. The removal of the Ni atoms produces an ordered lattice of vacancies creating the half-Heusler structure which tend to have small band gaps and semiconductor type behavior [149].

The MNiSn family of half-Heusler alloys has been extensively studied in effort to increase their **ZT** value [141,147,150,151]. These materials exhibit very high thermopower at room temperature conditions reaching values of over -200 μVK^{-1} [147-151]. Bhattacharya *et al* identified an increase in the power factor with small amounts of Sb doping in the Sn site of TiNiSn through a large decrease in the electrical resistivity despite a decrease in the thermopower [147]. This power factor, at the time of the study, was one of the highest in any material [147]. Other studies have observed a strong effect on the thermoelectric properties during the synthesis process when performing spark plasma sintering (SPS) at various temperatures [151]. Kurosaki performed SPS on (Zr_{0.6}Hf_{0.4})_{0.7}Ti_{0.3}NiSn at 973, 1173, and 1373 K and observed optimal thermoelectric efficiency in the sample prepared at 1173 K. Even though a

decrease was reported in the power factor, a decrease of 70% in the thermal conductivity leads to a **ZT** value of 0.43 at 760 K [151]. Similarly to other half-Heusler compounds, MNiSn exhibit large thermal conductivity and without proper reduction of these large values, their applicability is limited.

The high-pressure structural and thermoelectric behavior of TiNiSn has not been explored experimentally. As mentioned, due to the importance of pressure as a method for tuning the transport properties of materials and identifying new phases of materials with potentially favorable thermoelectric properties, it is imperative to study this material at extreme conditions. Theoretical studies have been conducted by Wang *et al* and Hermet *et al*. Wang *et al* predicts values for the bulk modulus of TiNiSn utilizing the BM-EOS as a model [141]. In a comparison study of the full-Heusler TiNi₂Sn and half-Heusler TiNiSn, Hermet *et al* compares the mechanical and structural properties of these materials predicting Young's and shear moduli as well as the bulk modulus for these materials [152]. To this date, there are no theoretical studies of the high-pressure thermoelectric behavior of TiNiSn. In order to provide some information into the possible high-pressure behavior of this material, we have performed synthesis, structural characterization, high-pressure powder X-ray diffraction (HPXRD) and high-pressure electrical and thermal measurements on TiNiSn. HPXRD measurements were performed up to 50 GPa revealing a pressure-induced structural phase transition at 35 GPa. In the high-pressure electrical and thermal experiments, we measured the electrical resistance, Seebeck coefficient, relative change in the thermal conductivity, and relative changes to the dimensionless figure of merit, **ZT**, of TiNiSn up to 5 GPa observing an overall positive effect on the thermoelectric efficiency over this pressure range.

Ambient Crystal Structure

As previously described, half-Heusler compounds crystallize in the MgAgAs type structure with a typical chemical composition of XYZ, where X and Y are transition metals and Z is an sp-valent element [144]. The crystal structure of TiNiSn consists of three interpenetrating face centered cubic (fcc) sub-lattices similar to TiCoSb and other HH alloys. Ti and Sn form two sub-lattices which combine to form a rock-salt sub-structure while the third sub-lattice containing Ni is displaced by one-fourth of a unit cell along the body diagonal of the rock-salt structure as depicted in **Figure 72**.

Sample Synthesis

TiNiSn was synthesized using arc-melting technique and annealing processes. Appropriate stoichiometric quantities of high-purity elemental powders of the constituents purchased from Sigma Aldrich (99.9%) were weighed and finely ground with an agate mortar and pestle to ensure thorough mixing. This powdered mixture was then made into a pellet using a die-press, which was then placed into a copper hearth and inserted into the chamber of an arc-melting furnace. The chamber was evacuated and re-filled with high-purity Ar gas several times before performing the synthesis. The pellet was reacted several times by creating a high-temperature arc between a tungsten tip and the copper hearth and allowing this arc to melt the pellet for several seconds. The resulting ingot was removed from the copper hearth, re-ground and re-pelletized. This new pellet was then placed into a quartz tube which had been evacuated to 10^{-5} torr and flushed several times with high-purity Ar gas and then sealed with a propane-oxygen torch. The sealed quartz tube was placed into a muffle furnace at 800°C for a week. The quartz tube was removed and quickly cooled by placing it into a bath of liquid nitrogen. The

phase purity of the resultant compound was examined with a Bruker D-8 Advance powder X-ray diffractometer with a Cu K- α X-ray source ($\lambda = 1.5416$ angstrom) with a Ni filter installed. The sample was confirmed to be single-phase with the ambient MgAgAs structure which agrees with the literature [144].

Figure 73 depicts the XRD pattern collected at ambient pressure and temperature conditions in a capillary. A full profile Rietveld refinement was performed on the data as indicated in **Figure 73**. The spectrum reveals a single-phase structure which can be indexed to the ambient cubic structure with $F-43m$ (No. 216) space group accounting for all the peaks in the XRD pattern. The Rietveld refinement performed shows good agreement between the observed XRD pattern and the Rietveld modeling as evidenced by the small differences shown in **Figure 73** beneath the XRD pattern. The refined structural unit cell parameters for TiNiSn are $a = b = c = 5.933(1) \text{ \AA}$, which agrees well with the literature values [153]. Atomic positions for all atom locations in the unit cell for the MgAgAs crystal structure are fixed.

High-Pressure Structural Measurements

High-Pressure Powder X-ray Diffraction

Figure 74 depicts the evolution of the XRD patterns with increasing pressure. The expected shift to higher angles as pressure is increased is clearly visible throughout the entire pressure range. Below 39.3 GPa, it is clear that the sample remains in the ambient crystal structure as the only new peak becoming visible is due to the Ne PTM. This new peak begins to appear as a small asymmetry visible in the 13.6 GPa XRD pattern near the (220) XRD peak at approximately 8.5° two-theta marked with a black diamond in **Figure 74**. As pressure is further

increased this asymmetry becomes its own highly visible peak that is identifiable as the Ne PTM [153].

However, at 39.3 GPa, a small peak near 5° two-theta and an asymmetric shoulder peak to the left of the (220) peak both begin emerging becoming significantly more prevalent as pressure is increased to 50 GPa. In order to elucidate other smaller XRD peaks that begin to emerge after 39 GPa, **Figure 75** depicts the XRD patterns corresponding to 33.5, 39.3, 47.7, and 50 GPa separately in order to enhance visibility of smaller XRD peaks. **Figure 75** clearly reveals several new peaks appearing at 39 GPa up to 50 GPa which are marked by red diamonds in the plot. In the 39.3 GPa XRD pattern, 6 new peaks emerge, including two shoulder peaks as labeled in **Figure 76**. Upon further increase of pressure to 47.7 GPa, two more XRD peaks emerge and with the increase to 50 GPa all 8 new peaks corresponding to a new high-pressure structural phase are clearly visible. This slow evolution of XRD patterns indicates a fairly sluggish structural phase transition in TiNiSn with an onset pressure of approximately 39 GPa. Due to the largely mixed phase even at the highest pressure measured, it is difficult to definitively identify this high-pressure crystal structure. However, an attempt to index the 8 peaks corresponding to the new phase was made using the search-match capabilities of MDI Jade software. Possible space groups were identified, but due to the extremely small number of peaks from the new high-pressure phase, it is not possible to definitively determine the high-pressure phase from the available data.

Up to 33.5 GPa, the XRD patterns can be indexed well to the MgAgAs structure and as such Le Bail refinements have been performed on each XRD pattern to obtain the lattice parameters at each pressure. Once this refinement is performed on each XRD pattern corresponding to the entire pressure range for the MgAgAs ambient crystal structure, the lattice

parameter, **a**, can be extracted and is displayed in **Table 7**. The lattice parameter, **a**, is plotted as a function of increasing pressure in **Figure 76**. The smooth decrease in the lattice parameter with compression indicates a reduction in the unit-cell volume as expected for the TiNiSn sample.

Equation of State Analysis

From this lattice parameter, the unit-cell volume can be calculated similarly to TiCoSb by cubing the lattice parameter, **a**, from **Table 7**, which leads to the unit-cell volume parameters displayed in **Table 8**. As mentioned in the previous chapters, the pressure versus unit-cell volume data can be fit to the 3rd-order BM-EOS (**Equation 13**) and the Rose-Vinet EOS (**Equation 14**). These fits allow for a determination of the initial volume, bulk modulus, and derivative of the bulk modulus as fit parameters for both EOS. A plot of the unit-cell volume as a function of increasing pressure along with the fits to both the 3rd-order BM-EOS and the Rose-Vinet EOS is displayed in **Figure 77**. As clearly evident by the plot in **Figure 77**, there is an excellent agreement between the EOS fits and the collected pressure versus volume data for TiNiSn over the pressure range from ambient pressure to 33.5 GPa before the structural phase transition.

The initial volume parameter as determined from both the 3rd-order BM-EOS and the Vinet EOS are $V_0 = 208 (1) \text{ \AA}^3$ for both. This is in very good agreement with the unit-cell volume extracted from the ambient pressure XRD pattern displayed in **Figure 73**. The unit-cell volume from the ambient pressure XRD is $208.9 (1) \text{ \AA}^3$ as displayed in **Table 7** and it is clear that both the fitted unit-cell volume and the measured volume agree well. Values of the bulk modulus from the fit to the 3rd-order BM-EOS and the Vinet EOS are provided in **Table 8** as $B_0 = 128 (4) \text{ GPa}$ for both fittings. Similarly to the analysis of TiCoSb, there are no experimental

measurements of the high-pressure structural properties of TiNiSn making direct comparison of the bulk modulus impossible. However, a theoretical determination of a predicted value for the bulk modulus for TiNiSn was reported by Wang *et al* which is a value of 122 GPa [141,152]. This is in very good agreement with our experimentally determined value of 128 (4) GPa.

High-Pressure Thermoelectric Measurements

Radiography Sample Thickness Measurements

Figure 78 depicts radiography images of the TiNiSn sample as pressure is increased. As with the previous radiography image evolutions with pressure, these are taken at the edge of the sample to better visualize the change in thickness of the sample. As discussed in **Chapter II**, these radiography images can be analyzed and from the analysis the sample thickness can be determined. In doing so, a plot of the sample thickness as a function of increasing pressure for TiNiSn is obtained and is displayed in **Figure 79**. The large initial change in sample thickness from 0 GPa – 0.5 GPa is likely due to the large variation in the cell part dimensions in the vertical direction as mentioned before mainly due to the thickness of the BE gasket and better packing of the sample pellet. However, the significantly more consistent slope in the sample thickness as a function of pressure after this initial compression indicates the sample has reached a compressed and densified state.

High-Pressure Electrical Resistivity Measurements

Figure 80 displays the electrical resistivity data collected up to 4 GPa for TiNiSn. A generally decreasing trend is observed over the pressure range from 1 to 3 GPa with a small upturn after 3 GPa. The decrease in electrical resistivity is fairly large as it is a 25% decrease

from the value measured at 1 GPa. This decrease is very favorable for the thermoelectric efficiency of this material as the electrical conductivity increases by 25%. The small upturn in the electrical resistivity after 3 GPa corresponds to about a 5% increase and thus a 5% decrease in the electrical conductivity. As the HPXRD data does not show any change in the structure at these pressures, further measurements are required to fully understand this interesting behavior. It is useful to note that this upturn is similar to the trend in the electrical resistivity data for TiCoSb in **Figure 80**.

High-Pressure Seebeck Coefficient Measurements

The variation in the Seebeck coefficient as a function of pressure for TiNiSn is plotted in **Figure 81**. The Seebeck coefficient at 1 GPa is $-339 \pm 4 \mu\text{V/K}$ which is slightly larger in absolute value than TiNiSn measured at ambient pressure conditions in the literature [147]. This slightly larger value may indicate that the increasing trend in the Seebeck coefficient which is clearly evident in **Figure 81** may begin even before 1 GPa. The increasing trend in the absolute value of the Seebeck coefficient over the entire pressure range is very promising for the overall thermoelectric efficiency of TiNiSn. The highest pressure attained in the measurements on TiNiSn is 3.5 GPa which corresponds to a value of $-388 \pm 7 \mu\text{VK}^{-1}$. The overall increase in the absolute value of the Seebeck coefficient from the 1 GPa value to the 3.5 GPa value is an increase of 13%.

High-Pressure Thermal Conductivity Measurements

The behavior of the thermal conductivity normalized to the lowest pressure value as a function of increasing pressure is depicted in **Figure 82**. A steady large increase of approximately 60% is observed over the entire pressure range from 1 to 3.5 GPa as displayed in

Figure 82. There may be a small change in the rate of increase in the thermal conductivity between 1 to 2 GPa and 2 to 3.5 GPa. This large overall increase in the thermal conductivity is unfavorable for the thermoelectric efficiency as evidenced by **Equation 1** for **ZT**. Additionally, it is important to note that since the thermal conductivity of half-Heusler materials are typically quite high, these results indicate pressure may not be a sufficient approach to aid with this aspect of increasing thermoelectric efficiency. However, since the Seebeck coefficient and the electrical resistivity both respond favorably to increasing pressure, it may still lead to a favorable effect on **ZT**.

High-Pressure Dimensionless Figure of Merit, ZT

Combining the electrical resistivity, Seebeck coefficient, and thermal conductivity measurements the **ZT** value for TiNiSn can be calculated as a function of pressure using **Equation 1**. **Figure 83** plots **ZT** normalized to the lowest pressure value as a function of increasing pressure. An overall increase in **ZT** is observed over the pressure range from 1 to 3 GPa with a leveling out as pressure is increased further to 3.5 GPa. The initial increase in **ZT** value over the pressure range from 1 to 3 GPa is almost 15%. This 15% increase is despite the large increase in the thermal conductivity of over 60%, and is likely due to the fairly large increase in the absolute value of the Seebeck coefficient over this same pressure range in addition to the electrical resistivity decrease. As reduction of the thermal conductivity through doping has been greatly explored for half-Heusler type alloys, further exploration of doped alloys of TiNiSn at high-pressure conditions may be interesting to pursue. Nonetheless, measuring the properties of the pure TiNiSn alloys for an understanding of the pressure effect on the thermoelectric properties without distortions introduced through doping.

Conclusions

We have performed high-pressure angle-dispersive powder X-ray diffraction on TiNiSn up to 50 GPa for the first time and have observed stability of the ambient MgAgAs crystal structure up to 33.5 GPa. Above 33.5 GPa, there are distinct indications of a pressure-induced secondary crystal phase developing as pressure increases to 50 GPa evidenced by the emergence of several new diffraction peaks which become more apparent from 39 to 50 GPa. The coexistence of this new high-pressure phase and the MgAgAs ambient crystal structure makes identifying the new phase difficult, yet an attempt was made and identified possible crystal structures for this high-pressure phase. Systematic theoretical calculations for identifying the stable high pressure phase based on the experimental observation are under progress. Up to 33.5 GPa, the evolution of the unit-cell volume as a function of pressure was fit to both a 3rd-order BM-EOS and a Vinet EOS yielding a bulk modulus value of 128 (4) GPa which agrees fairly well with predicted values of the bulk modulus through theoretical modeling. Measurements of the thermoelectric properties at high-pressure conditions from 1 to 3.5 GPa were also conducted for the first time. A 25% decrease in the electrical resistivity, or increase in the electrical conductivity, a 13% increase in the absolute value of the Seebeck coefficient, and a 60% increase in the thermal conductivity were observed over this pressure range. By combining these measurements, the trend in **ZT** was determined with increasing pressure and an overall increase of almost 15% was observed over the pressure range. Although the large increase in the thermal conductivity is disappointing considering half-Heusler alloys typically have large thermal conductivity initially, the favorable response of the electrical properties lead to an increase in the thermoelectric efficiency with increasing pressure for this sample.

Chapter IX – Conclusions

The scientific goal of this project was to develop a system to measure high-pressure and high-temperature transport properties with access to synchrotron radiation to perform radiographic imaging to measure sample dimensions *in-situ* and X-ray diffraction measurements to correlate structural properties with transport properties at extreme conditions. It was developed with the end goal in mind of establishing this system as a technique to open for general users at the Sector 16 BM-B beamline at the High-Pressure Collaborative Access Team (HPCAT) at the Advanced Photon Source (APS) at Argonne National Laboratory (ANL). Overall, this project has been very successful with both of these goals as the high-pressure thermoelectric behavior of a variety of materials (PbTe, SnTe, TiNiSn, TiCoSb) have been explored with this system and it is beginning to open to general users at the synchrotron. Furthermore, although only thermoelectric materials have been studied within the scope of this dissertation, the generalized nature of the measurements being performed with this system allows extreme versatility with sample selection. This versatility allows for practically any material to be studied which can be very beneficial to the fundamental understanding of correlations between transport properties and structural properties.

The first measurements with this system involved a large number of experiments performed on elemental bismuth yielding highly repeatable measurement of the electrical resistance and the reproduction of the qualitative behavior of this property at high-pressures. It is, in fact, the well established behavior of the electrical resistance of Bi at high-pressure conditions that it was chosen as a reference material to allow an understanding of the cell assembly design. The early measurements of Bi as discussed within this dissertation and in a previously published scientific article by Baker *et al* provided a basic framework for the operation of this system [75].

As time went on, it was noticed that some issues arose with the measurements at particularly high-pressure and temperature conditions that required significant design changes to the sample cell assembly. Specifically, the use of single crystal diamonds, although more expensive than the polycrystalline counterpart, was found to be imperative to enable proper electrical isolation and thermal conduction. Later measurements of Bi as discussed within this dissertation and in a previously published scientific article by Baker *et al* established the parameters of use and acted as a proof of capabilities of the system [76]. The results of these measurements on Bi are highly interesting as Bi undergoes several phase transitions over the pressure ranges measured from 0 to 4 GPa. The electrical resistivity measurements reveal large changes correlating extremely well with the known structural phase transitions and the Seebeck coefficient and thermal conductivity were observed to respond along the boundaries of these phase transitions as well [76].

The next measurements that were performed with this system were on the classic thermoelectric material PbTe. PbTe and its related lead chalcogenides have been studied extensively as promising thermoelectric materials at both ambient and high-pressure conditions. Our measurements of PbTe were performed to establish further capabilities of this system in measuring thermoelectric properties of a proper thermoelectric material at extreme conditions. The electrical resistivity measurements performed on PbTe revealed a large decrease in value favorably effect the **ZT** value of PbTe over the pressure range of 2 to 5.5 GPa and this agreed quite well with previously reported literature by Ovsyannikov *et al* [102]. Both the isobaric behavior the Seebeck coefficient as temperature was increased was measured and the isothermal behavior as pressure was increased was measured for PbTe. The results of the isobaric measurements revealed an increase in the absolute value of the Seebeck coefficient with increasing temperature as is expected when compared with various reports. The absolute value of

the Seebeck coefficient as a function of increasing pressure for PbTe is observed to decrease over the pressure range measured. Finally, the relative changes in thermal conductivity for PbTe reveal an increase in thermal conductivity over the pressure range which is unfavorable for the overall thermoelectric efficiency of this material. Despite the behavior of the Seebeck coefficient and the thermal conductivity, an overall increase in **ZT** value is observed for PbTe over the pressure range measured which agrees well with the observations of large increase in the power factor by Ovsyannikov *et al* [102]. These results on PbTe were also published previously by Baker *et al* [76].

Measurements on another binary chalcogenide SnTe further establishes this system and provides very interesting scientific results. The electrical resistivity was observed to have very interesting behavior as pressure was increased. Below 3 GPa, the electrical resistivity is observed to decrease, and upon further compression, the electrical resistivity is observed to increase. This behavior qualitatively agrees with previously established literature on SnTe and correlates well with a pressure-induced structural phase transition from the ambient *Fm-3m* crystal structure to a complicated mixed phase above 3 GPa. The Seebeck coefficient of SnTe is observed to increase by over 200% with compression and this increase is correlated to a pressure-induced structural phase transition well established in the literature and observed in energy dispersive X-ray diffraction (EDXRD) measurements performed *in-situ*. The Seebeck coefficient of SnTe has been predicted to increase with pressure application by Xu *et al*; however, this increase is expected at slightly lower pressures than is observed in our experiments [124]. Despite this, as the predicted values do not account for the structural phase transition, some discrepancies in the pressure is possible. The thermal conductivity of SnTe was observed to increase from 1 GPa to 3 GPa, with a subsequent decrease as pressure was increased further. This again correlates very

well with the structural phase transition and the other thermoelectric property measurements performed at high-pressure. The combination of these thermoelectric properties lead to a 350% increase in ZT value for SnTe under compression as it undergoes a structural phase transition. This is a highly important experimental observation indicates the possibility of significantly enhanced thermoelectric properties in the high-pressure phase for SnTe.

As promising ambient pressure thermoelectric measurements reported enhanced properties of SnTe with the introduction of Mn to the Sn site [118], we studied the high-pressure thermoelectric and structural properties of $\text{Sn}_{1-x}\text{Mn}_x\text{Te}$ ($x = 12\%$) up to 5 GPa and 30.7 GPa, respectively. The high-pressure structural measurements revealed a pressure-induced structural phase transition from the ambient $Fm-3m$ phase to the high-pressure $Pnma$ phase at 6.9 GPa. This onset pressure is higher than the phase transition observed in pure-SnTe which occurs between 2 – 4 GPa [102-106]. The structural data obtained for Mn-doped SnTe indicates similar fit parameters to the 2nd-order BM-EOS, yet in the high-pressure phase there is less compressibility observed based on the bulk modulus value. The thermoelectric property measurements at high-pressure indicated very different behavior for Mn-doped SnTe when compared to pure-SnTe. The electrical resistivity of Mn-doped SnTe is observed to decrease significantly over the pressure range from 2 GPa to 5 GPa leading to a very favorable effect on the ZT value. Measurement of the Seebeck coefficient revealed a steady increase for the Mn-doped SnTe which while favorable to the overall ZT value did not behave similarly to pure-SnTe which remained at a steady value until 3 GPa when it increased drastically. The thermal conductivity was observed to increase over the pressure range for Mn-doped SnTe. Combining these measurements to calculate the ZT value for Mn-doped SnTe yielded a large increase in ZT over the pressure range of 250% mostly due to the large decrease in electrical resistivity.

Another important class of thermoelectric materials is the half-Heusler alloys. These alloys have typically very high Seebeck coefficient and low electrical resistivity as previously discussed throughout the dissertation. A significant issue with these materials tends to be the large thermal conductivity at ambient and elevated temperature leading to overall somewhat low **ZT** values. Exploration of chemical doping has lead to increased electrical properties and a reduction of the thermal conductivity, yet no understanding of the high-pressure behavior of these materials had been conducted previously. High-pressure thermoelectric property and structural measurements were performed on TiCoSb and TiNiSn half-Heusler alloys.

The results for TiCoSb lead to an observation of the electrical resistivity decreasing with increasing pressure up to 2 GPa followed by an upturn in the trend of the electrical resistivity up to the highest pressure measured. This behavior is highly interesting due to the lack of any structural phase transition over this pressure range as confirmed with XRD measurements performed separately with diamond anvil-cells (DACs). The Seebeck coefficient however shows almost no indication of changes over the pressure range measured. Instead, the value of the Seebeck coefficient remains extremely consistent with increasing pressure for TiCoSb only increasing by 6% over the pressure range. Whereas, the relative changes in thermal conductivity as pressure is increased for TiCoSb increasing significantly over the entire pressure range by almost 60%. When these results of the thermoelectric properties as a function of pressure are combined and **ZT** is calculated, it is observed that the relative value of **ZT** decreases over the pressure range measured for this material. In addition to the thermoelectric property measurements at high-pressure, high-pressure powder X-ray diffraction was performed on this material up to 115 GPa. No pressure-induced structural phase transition was observed and the *F-43m* ambient crystal structure was confirmed stable up to 115 GPa. These measurements enable

the determination of the compressibility of the material in the form of the bulk modulus by fitting the experimentally determined unit-cell volume versus pressure to an equation of state. Specifically, the data obtained for TiCoSb was fit to a 3rd-order BM-EOS and the Vinet EOS and the bulk modulus was determined to be 166 (6) GPa and 168 (6) GPa for both EOS, respectively. These values agree fairly well with predicted values calculated by Xu *et al* [143].

The results for the TiNiSn sample lead to an observation of an overall increase in thermoelectric efficiency as pressure is increased. The electrical resistivity determined as a function of increasing pressure is observed to decrease from the lowest pressure value of 1 GPa to approximately 3 GPa. With further compression past 3 GPa, the electrical resistivity has a small upturn indicating the potential for intriguing behavior if pressure was increased even further. The initial decrease in electrical resistivity is promising for the overall thermoelectric efficiency of this material; whereas, the upturn in electrical resistivity after 3 GPa may be detrimental to the efficiency at much higher pressures. The Seebeck coefficient behavior as a function of increasing pressure was observed to increase steadily in absolute value with an increase of ~13% over the pressure range measured. No indication of correlation between the behavior of the electrical resistivity and the Seebeck coefficient at the upturn at 3 GPa in the electrical resistivity is observed. From the measurements of the relative changes to thermal conductivity with increasing pressure, it can be concluded that pressure is an unfavorable variable to change to decrease thermal conductivity as it is observed to increase by almost 60% over the pressure range measured. However, despite the small upturn in the electrical resistivity and the fairly large increase in thermal conductivity over the pressures measured, the value of **ZT** is observed to increase by almost 15% up to 3 GPa with a possible plateau reached near this pressure. In addition to these thermoelectric property measurements at high-pressure, structural

measurements were performed on TiNiSn up to 50 GPa. The ambient $F-43m$ crystal structure remains stable up to 33.5 GPa and just as with TiCoSb, the bulk modulus is obtained in this structure. The bulk modulus was determined to be 128 (4) GPa from our experimental measurements which agrees fairly well with the theoretically predicted value of 122 by Xu *et al* [143]. As pressure is increased past 33.5 GPa, there is a clear indication of the coexistence of a new high-pressure phase due to the appearance of several diffraction peaks in the XRD patterns collected. Due to the small amount of peaks and the largely mixed nature of this high-pressure phase, no definitive identification of the structure of this high-pressure phase was determined. Theoretical calculations are required further to identify the stable high pressure phases based on our experimental observations.

In conclusion, this system is highly capable of performing extremely valuable high-pressure transport property measurements with the added benefit of *in-situ* radiography imaging and EDXRD measurement. As pressure plays a significant role in sculpting transport properties of materials, a large array of compounds can benefit from the measurement capabilities of this system. SnSe has recently been discovered to have incredible thermoelectric behavior at high-temperature in single-crystal form, and understanding the effect of high-pressure on these properties could aid in a fundamental understanding of these incredible properties [40]. Due to previously reported thermoelectric property results on lead chalcogenides responding favorably to compression, further measurement of these materials is imperative to furthering thermoelectric material research. It is very important to note that while this dissertation dedicatedly studied the properties of thermoelectric materials, this system has no inherent limit on the type of material being studied. As such, it could be highly beneficial to study the properties of other materials to understand the correlation between transport properties and structural properties. Additionally,

since this system is capable of obtaining even qualitative behavior of the thermal conductivity as a function of pressure, it is extremely applicable to measuring trends in thermal conductivity for various materials to validate theoretical models of these properties.

Appendix A – Figures

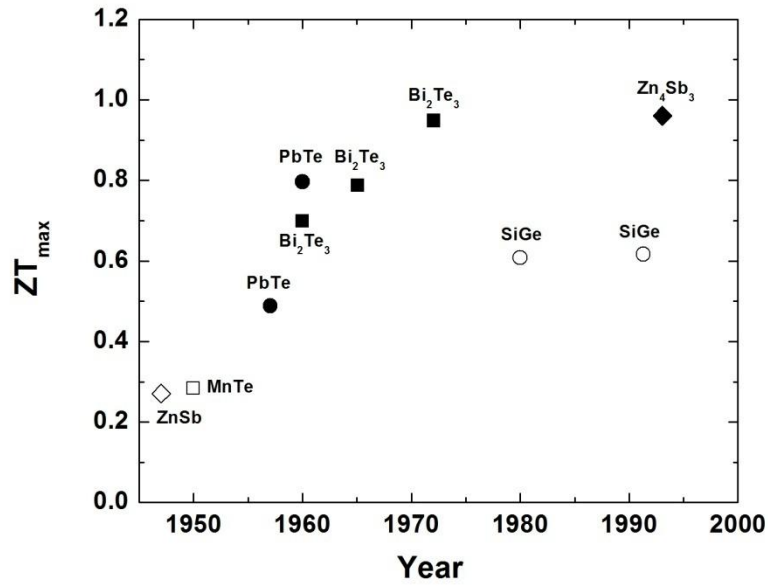


Figure 1. ZT vs. Time 1950 – 2000

Plot of the change in thermoelectric efficiency through ZT values as a function of time from 1950 – 2000. From 1950 – 1970 there was a great deal of rapid improvement in ZT values which leveled off for a significant amount of time. [11]

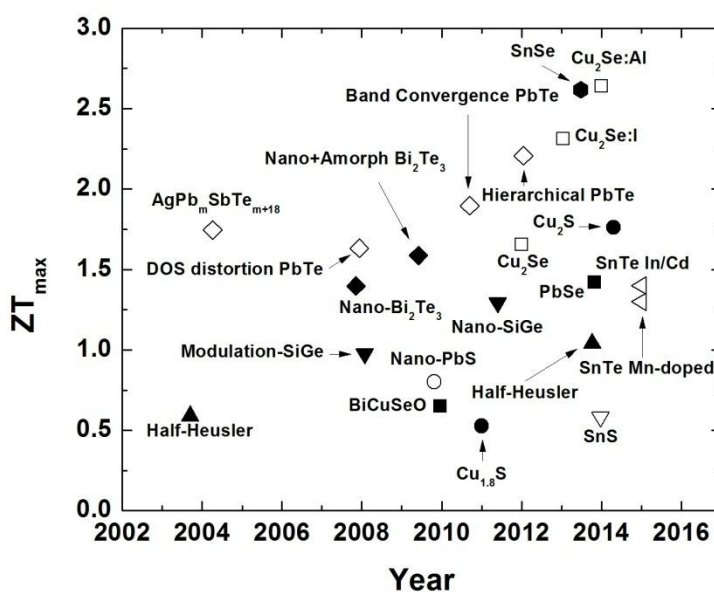


Figure 2. ZT vs Time: 2000 – Present

Plot of the change in thermoelectric efficiency via ZT values as a function of time over the sample two decades. A great deal of improvement in ZT is observed with values reaching as high as 3.0 nearing the potential of large-scale application. [7]

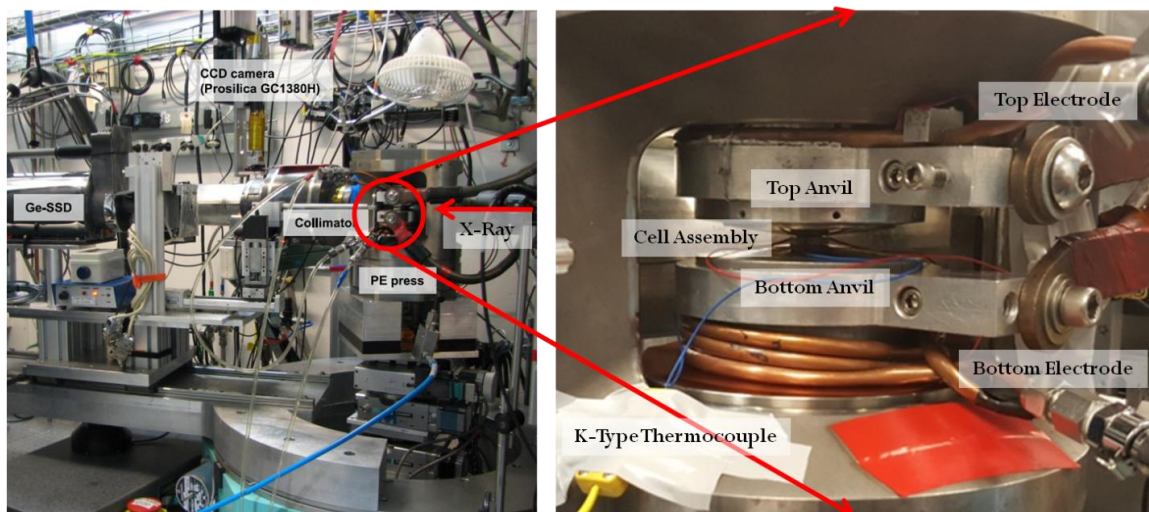


Figure 3. Paris-Edinburgh Photograph

(a) A photograph of the Sector 16 BM-B beamline at HPCAT with the Paris-Edinburgh press equipped and thermoelectric sample cell assembly installed. The X-rays are incident on the right hand side as indicated and after interacting with the sample the diffracted rays are collimated and collected by the Ge-SSD detector for X-ray diffraction measurement. The CCD camera shown in the photograph allows for X-ray radiographic imaging through high-contrast absorption pictures to measure sample thickness *in-situ*. (b) The thermoelectric cell assembly is photographed installed in the PE press with the K-type thermocouples being the electrical and thermal probes. Also shown in this picture are the electrodes which provide power for the graphite heater. [76]

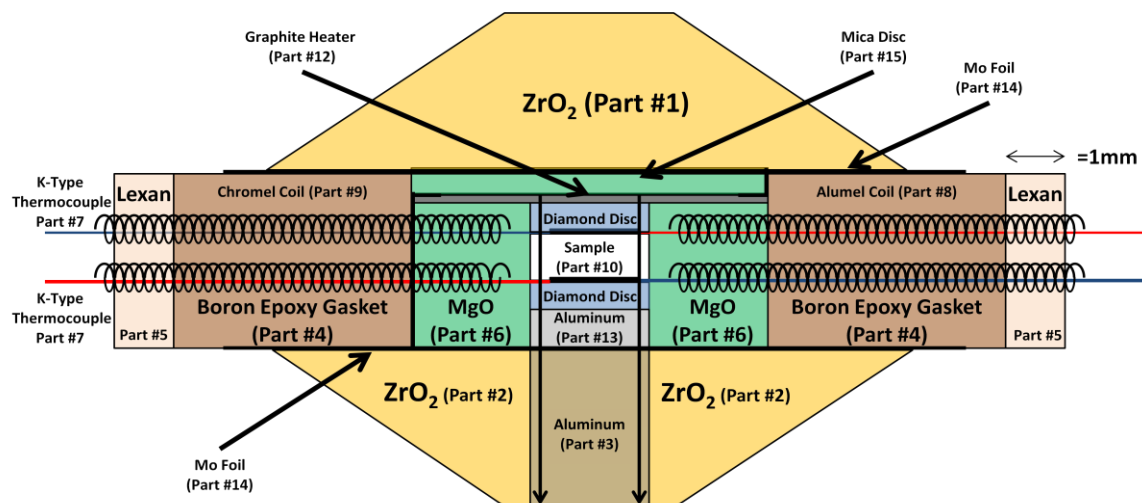


Figure 4. Thermoelectric Cell Assembly Schematic

A scaled schematic of the thermoelectric cell assembly. A variety of parts are required for proper assembly, but the most important section is the center where the sample lies. Electrical resistivity, Seebeck coefficient, relative changes in thermal conductivity, absolute temperature, and thermoelectric efficiency behavior at high-pressure and high-temperature conditions are measureable alongside X-ray radiography and X-ray diffraction *in-situ* with this cell assembly. [75,76]

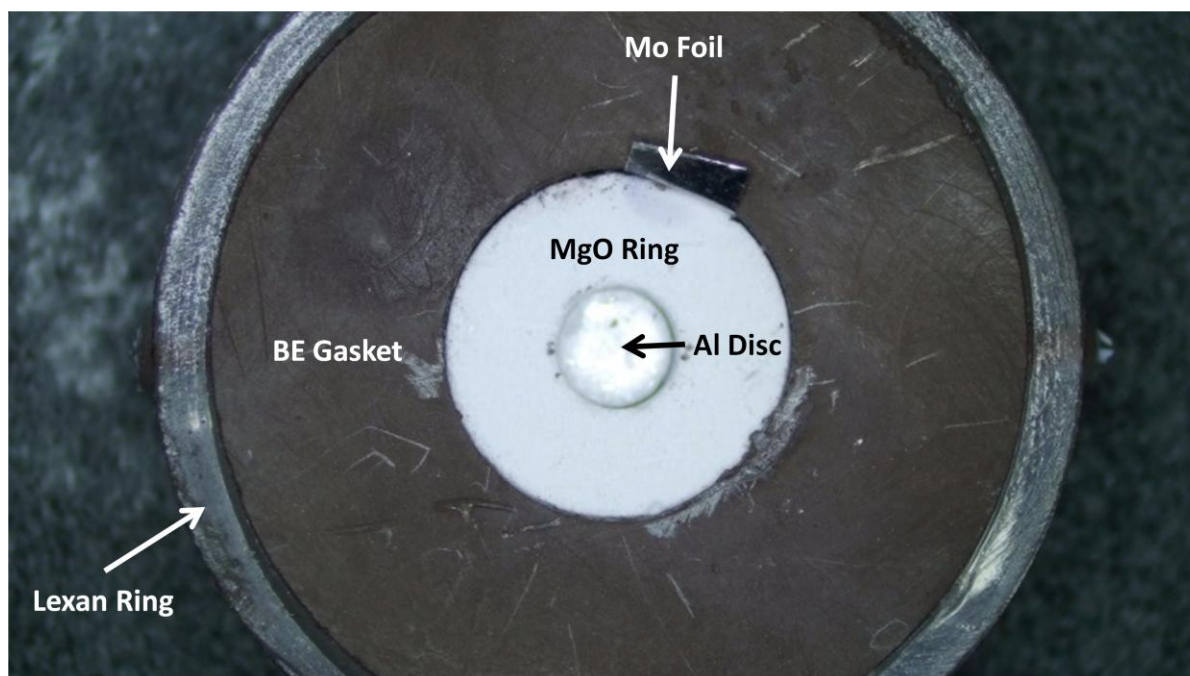


Figure 5. Cell Assembly Step #2

Sample cell assembly with bottom Al disc installed.

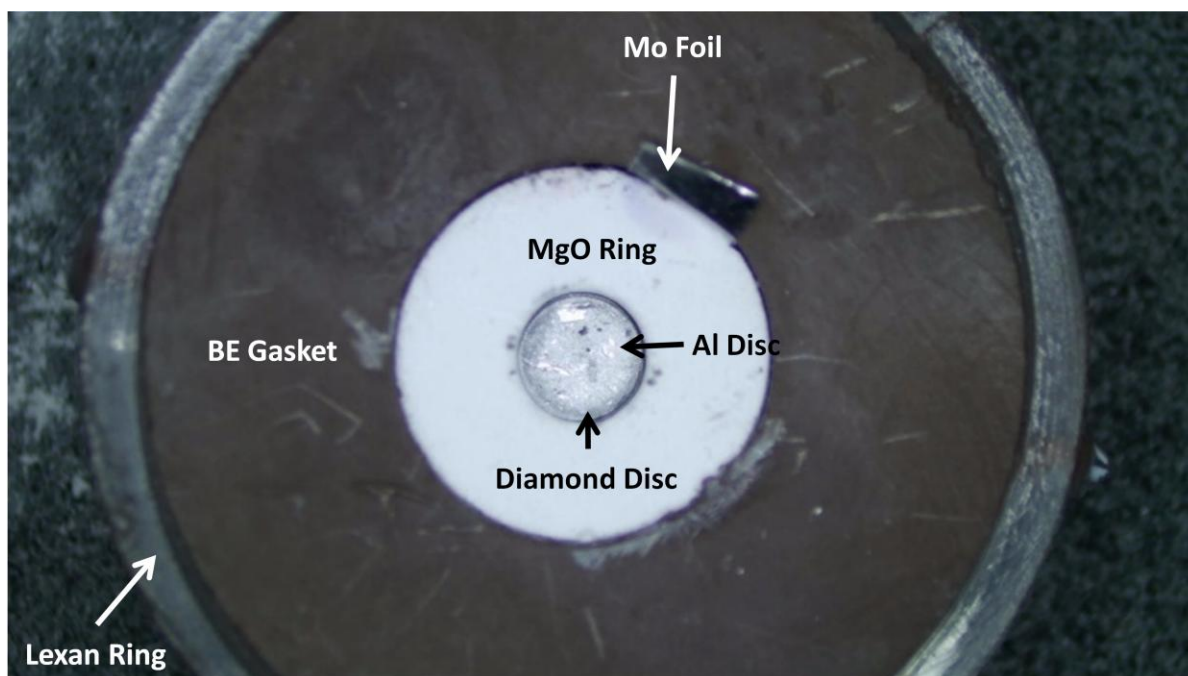


Figure 6. Cell Assembly Step #3

Sample cell assembly with bottom Al disc and bottom diamond disc installed.

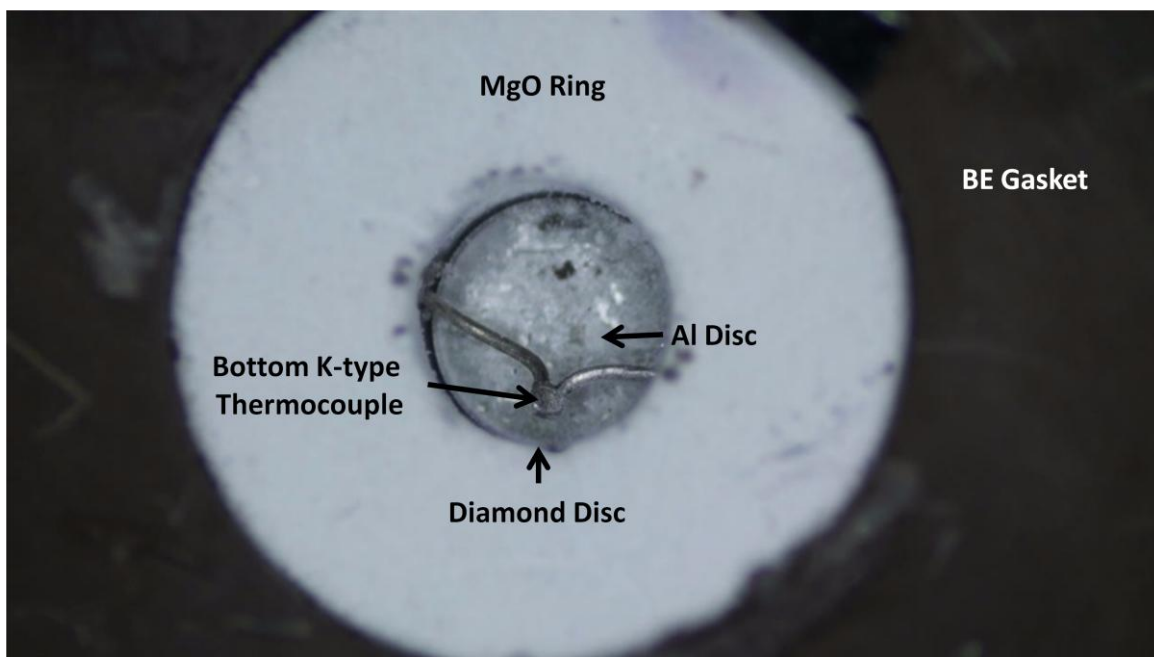


Figure 7. Cell Assembly Step #4

Sample cell assembly with bottom thermocouple inserted and centered above the bottom diamond disc.

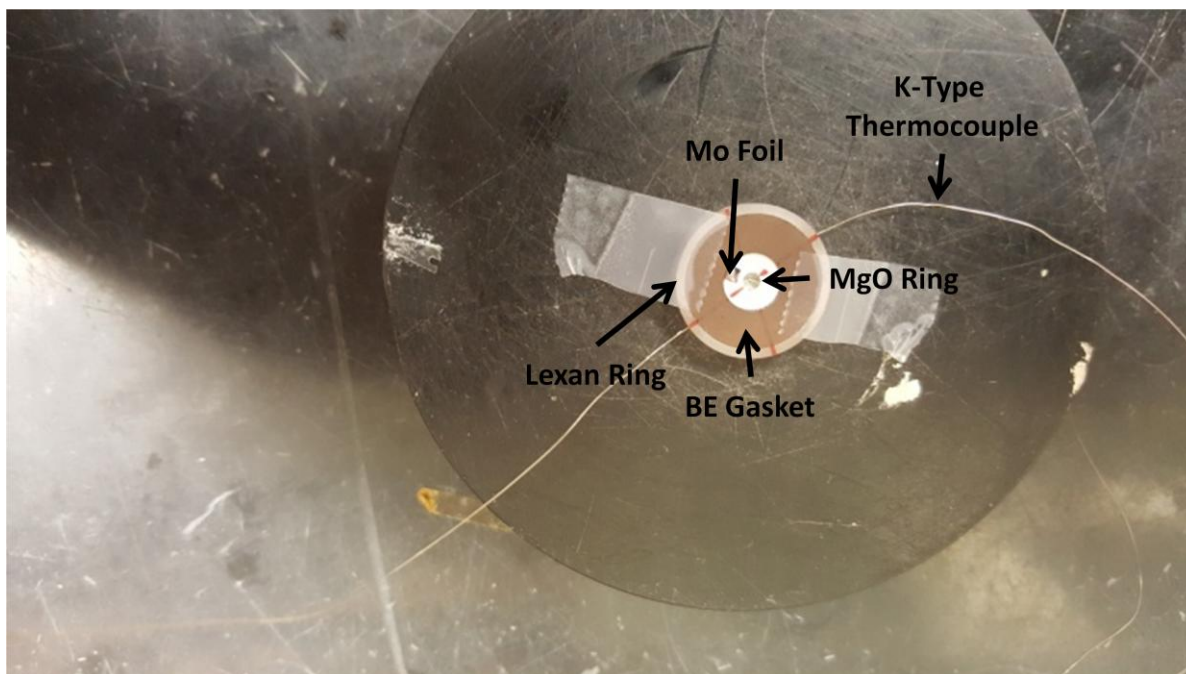


Figure 8. Cell Assembly Step #5

Sample cell assembly depicting the result of inserting the bottom thermocouple and the placement of the “spring coils.”

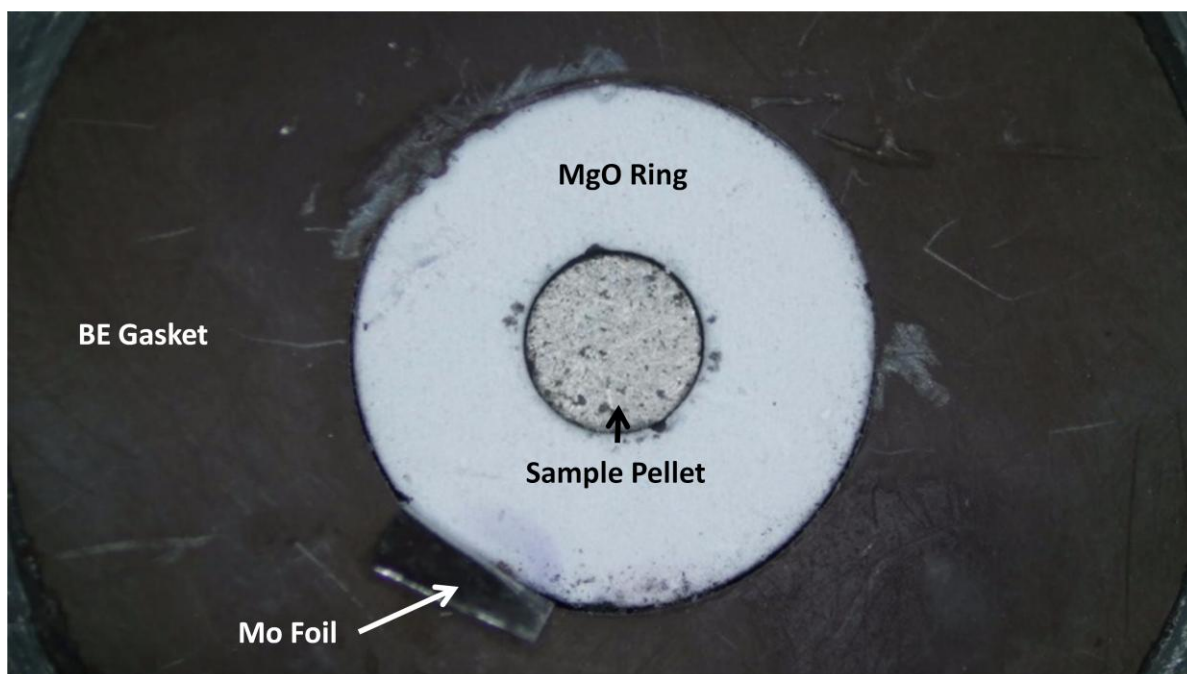


Figure 9. Cell Assembly Step #6

Sample cell assembly with the sample pellet inserted on top of the bottom thermocouple.

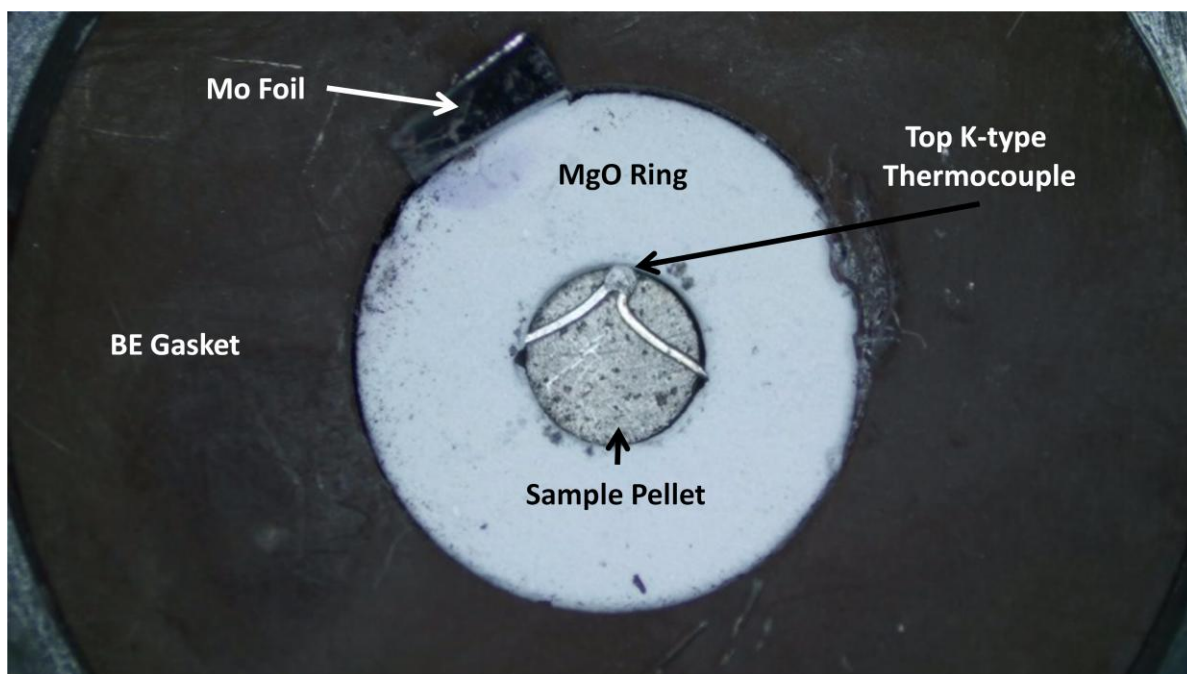


Figure 10. Cell Assembly Step #7

Sample cell assembly with the top thermocouple inserted and centered on top of the sample pellet.

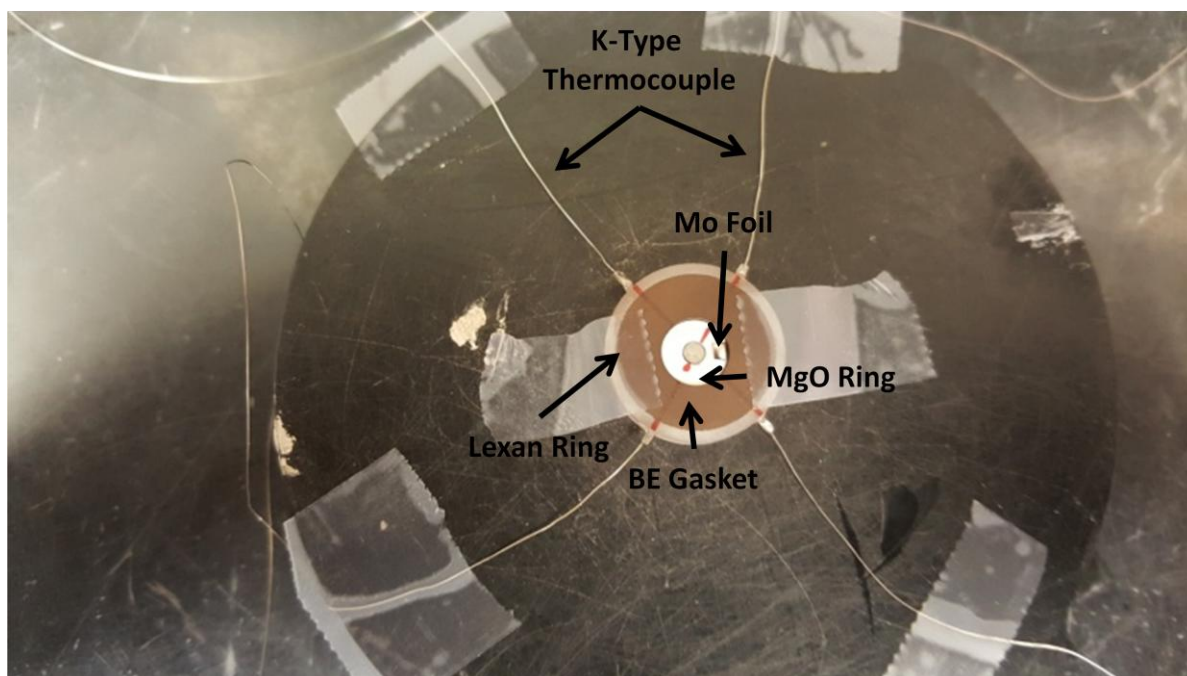


Figure 11. Cell Assembly Step #8

Sample cell assembly with both thermocouples and both sets of “spring coils” placed and glued.

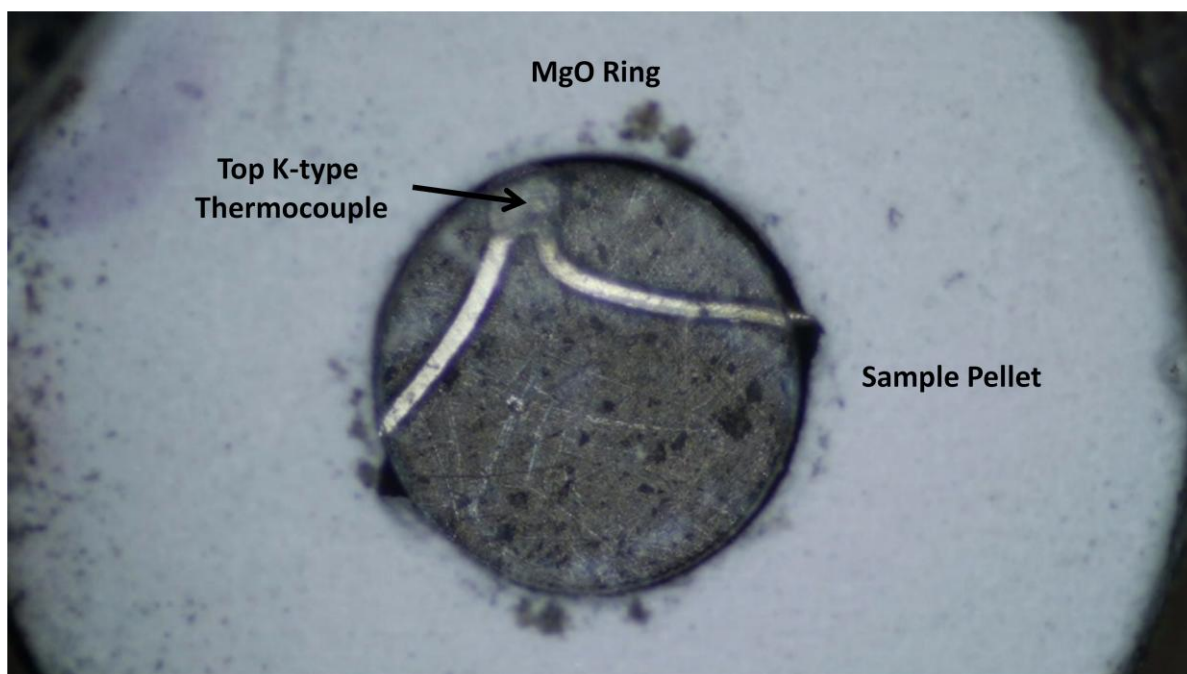


Figure 12. Cell Assembly Step #9

Sample cell assembly with the top diamond placed upon the completed sample stack.

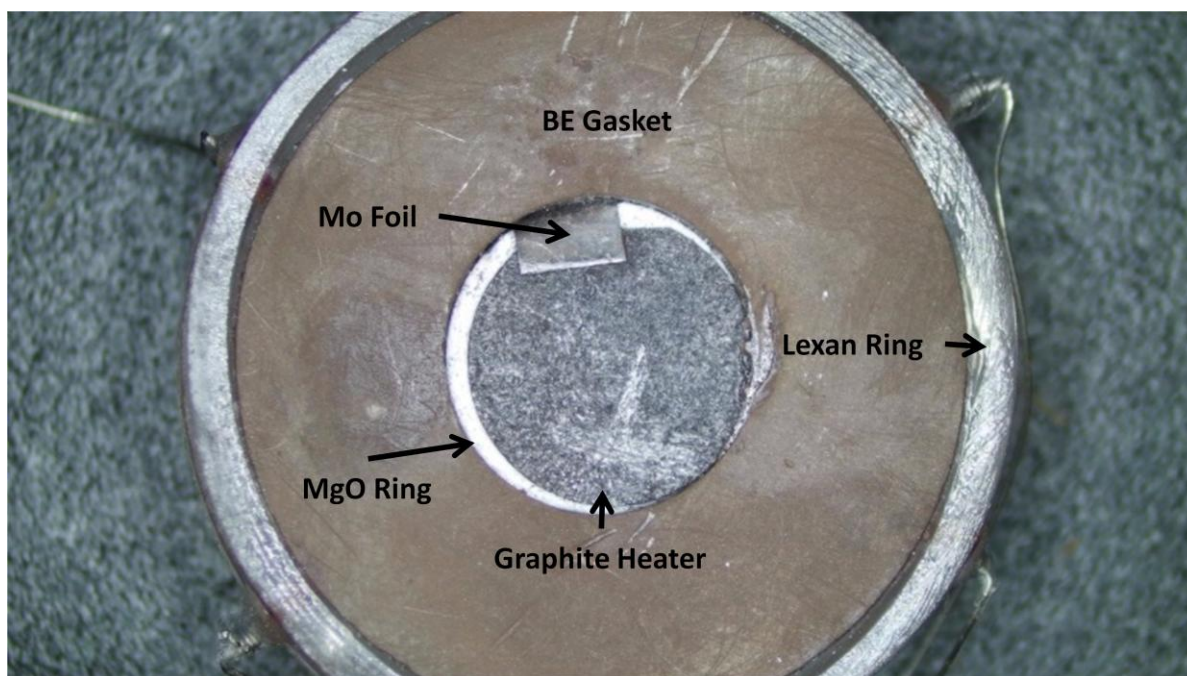


Figure 13. Cell Assembly Step #10

Sample cell assembly depicting the placement of the graphite heater placed above the sample stack. The small tab of the molybdenum foil has been bent over to make contact.

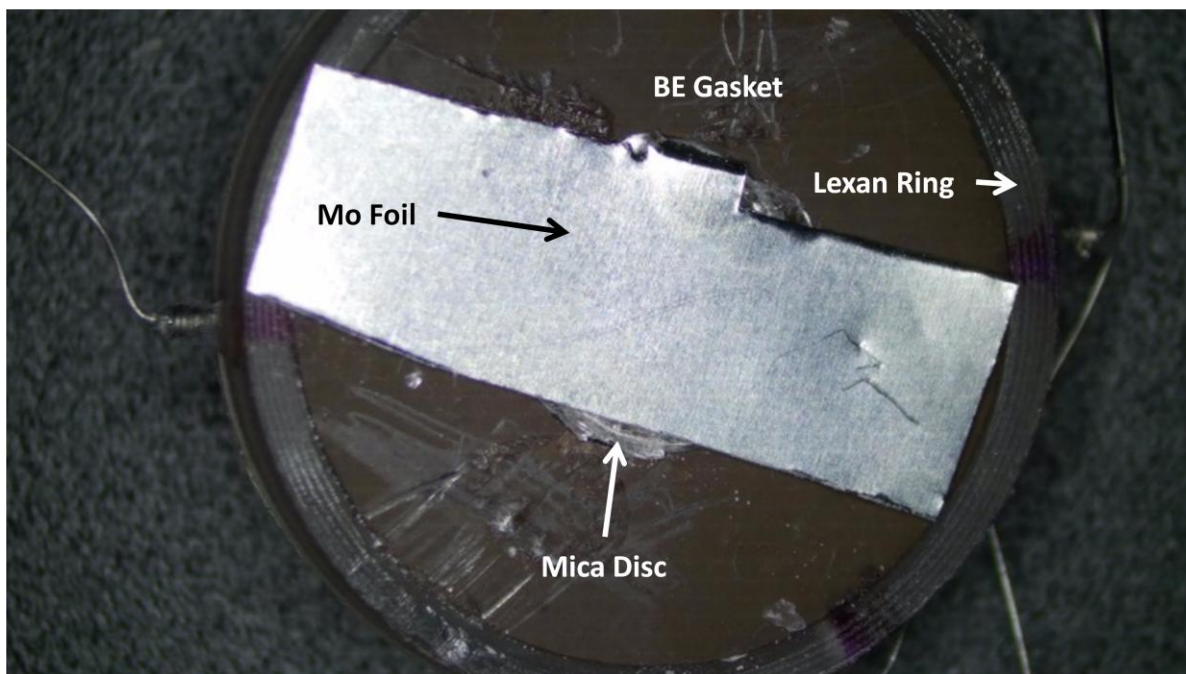


Figure 14. Cell Assembly Step #11

Sample cell assembly with the top molybdenum foil placed over the top of the assembly. Directly beneath the foil are mica discs for insulation from complete contact with the graphite heater.

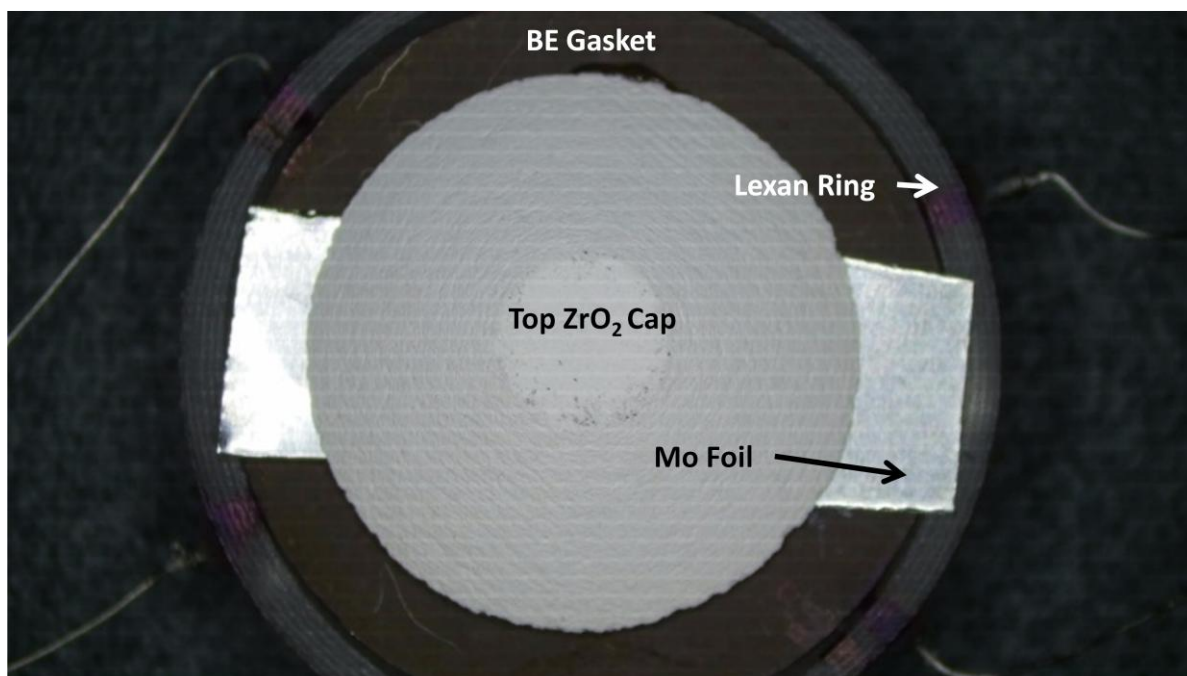


Figure 15. Cell Assembly Step #12

Sample cell assembly with the top ZrO₂ cap placed glued onto the molybdenum foil and the boron-epoxy gasket.

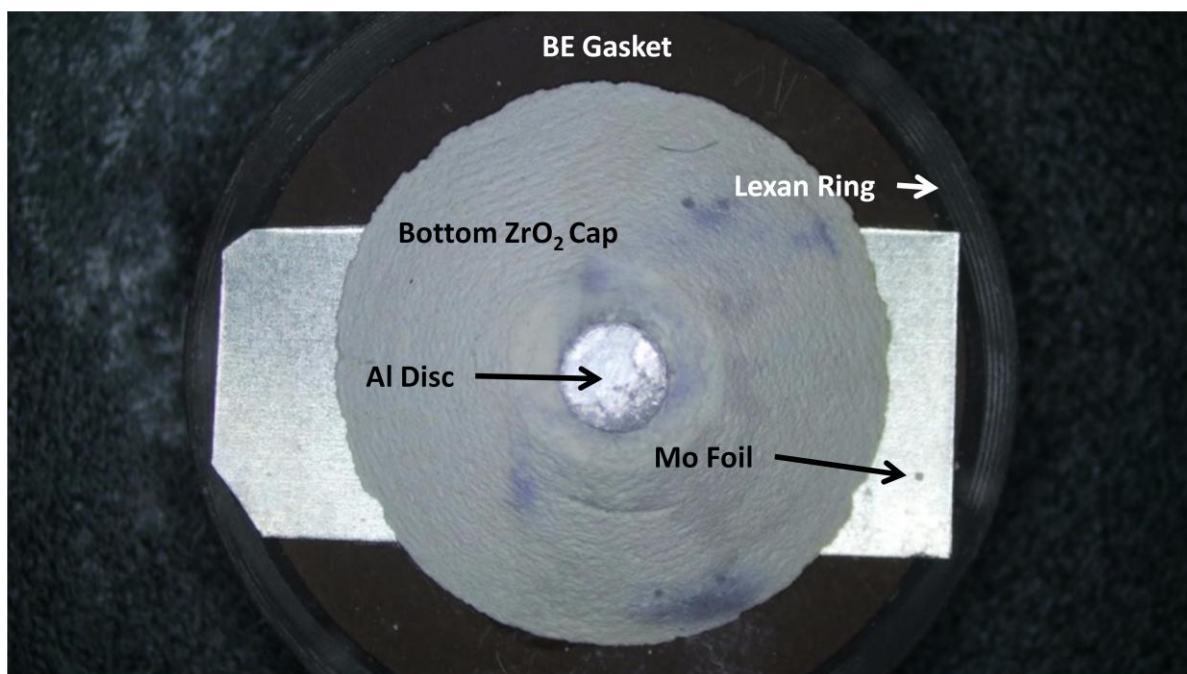


Figure 16. Cell Assembly Step #14

Sample cell assembly with view from the bottom after placement of the bottom ZrO₂ cap and insertion of the Al disc into the center of this cap.

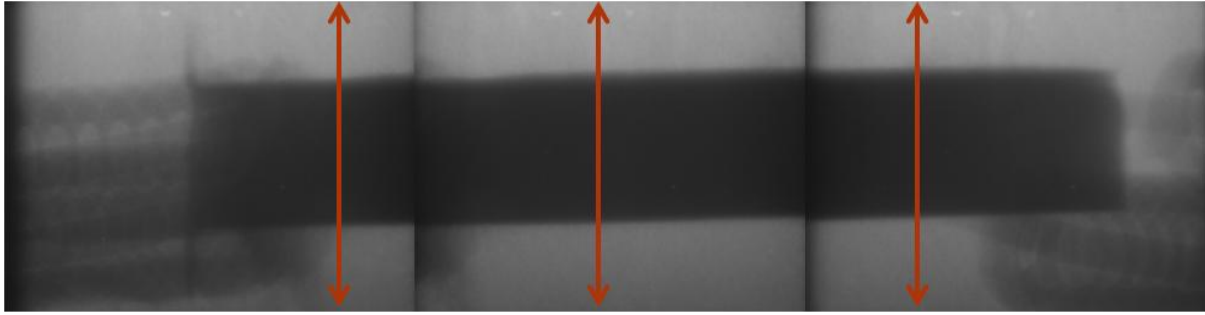


Figure 17. Example Radiography Image

Three radiography images stitched together to create a single radiographic image of a sample installed in the Paris-Edinburgh press with arrows indicating the three separate measurements of the sample thickness.

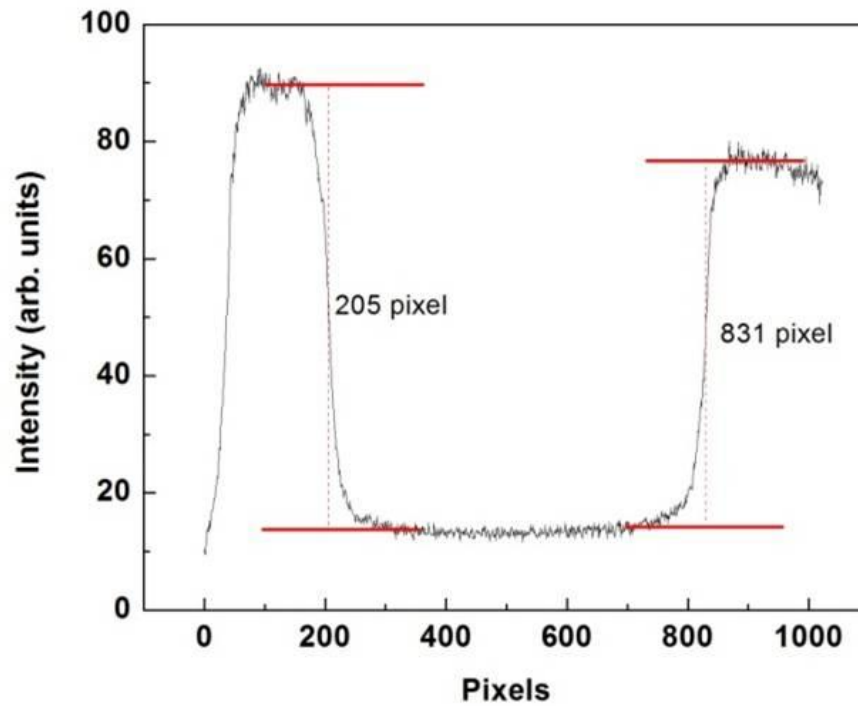


Figure 18. Example Intensity Profile

Example intensity versus pixel plot used to determine sample thickness from radiography images.

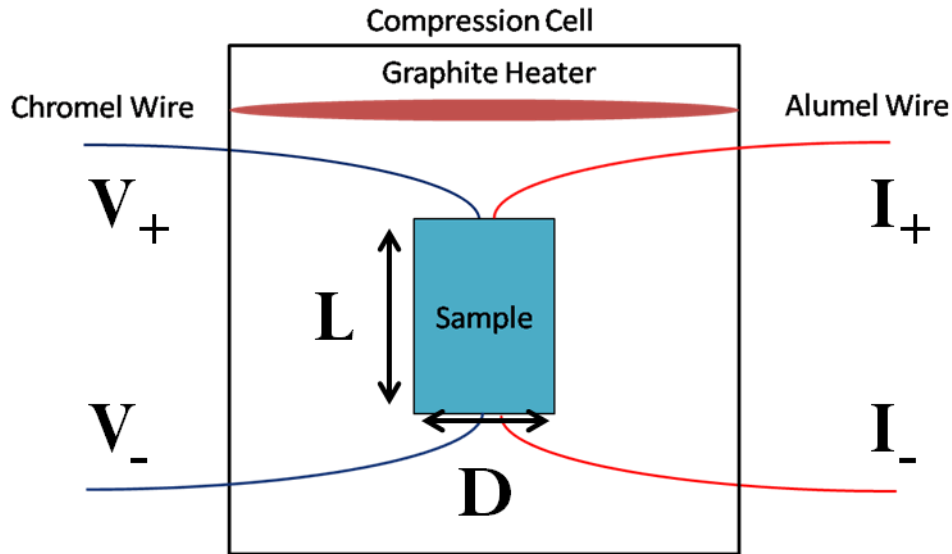


Figure 19. Electrical Resistivity Set-Up Schematic

Sample cell assembly schematic diagram depicting the parameters measured to determine the electrical resistivity of the sample. V_+ , V_- , I_+ , and I_- represent the measurements required to determine the electrical resistance of the sample through use of Ohm's Law. L represents the sample thickness, and D represents the sample diameter. Through combining the sample dimensions and the electrical resistance of the sample, the electrical resistivity is determined [76].

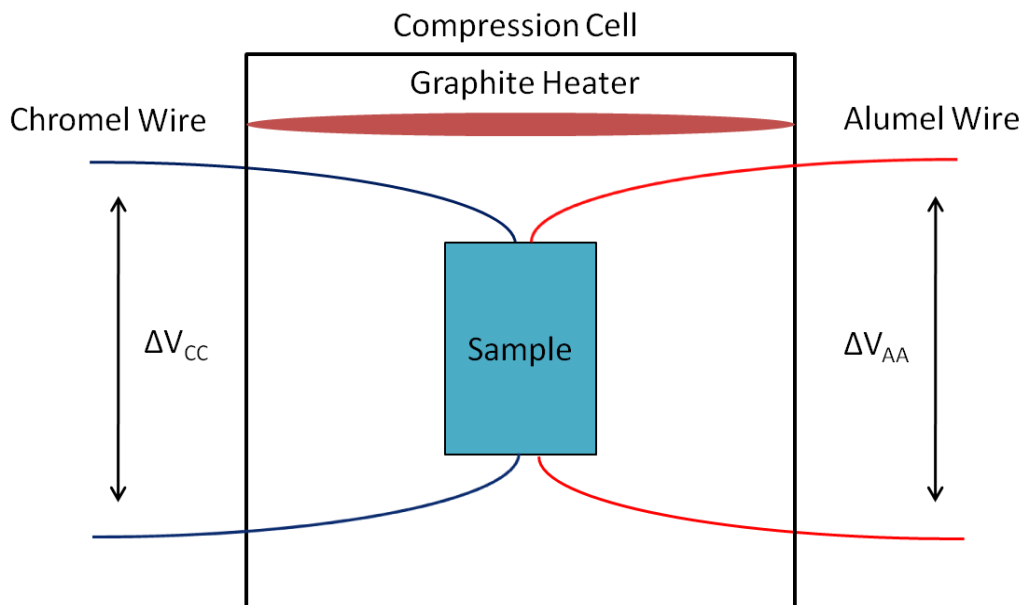


Figure 20. Seebeck Coefficient Set-Up Schematic

Sample cell assembly schematic diagram depicting the voltages measured to determine the Seebeck coefficient of the sample. ΔV_{CC} is the voltage from the top to the bottom thermocouple chromel wires and ΔV_{AA} is the similar voltage for the alumel wires [76].

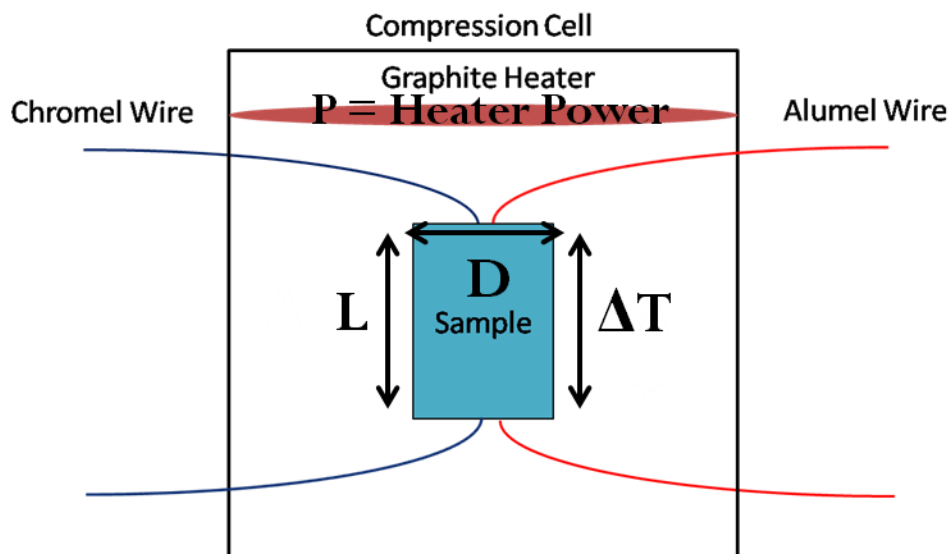


Figure 21. Thermal Conductivity Set-Up Schematic

Sample cell assembly schematic diagram depicting the parameters required for thermal conductivity measurements. L represents the sample thickness, D represents the sample diameter, ΔT represents the temperature difference across the sample measured from the top to bottom thermocouple. With these parameters, the thermal conductivity can be determined [76].



Figure 22. Princeton symmetric type diamond anvil cell [81].

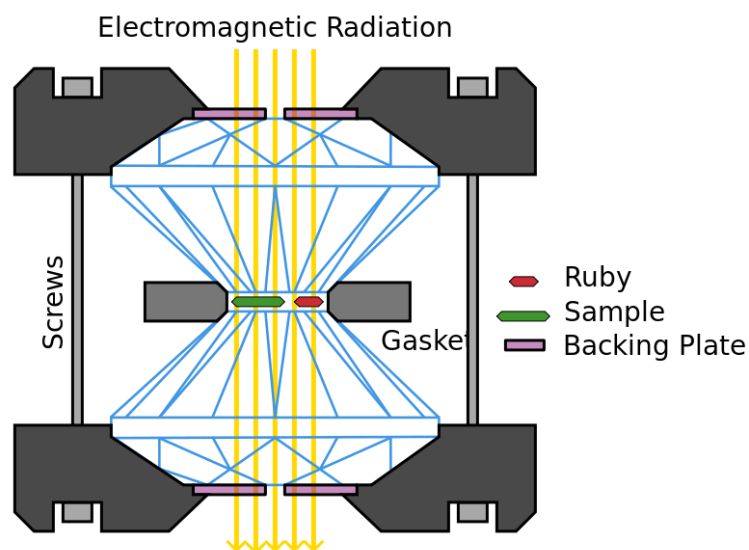


Figure 23. Diamond Anvil Cell Schematic

A schematic representing a typical design for a diamond anvil cell depicting the sample chamber with sample, ruby, and pressure transmitting medium. The screws are tightened to apply pressure to the sample chamber inside of the gasket. Additionally, the X-ray direction is indicated by the yellow arrows [82].

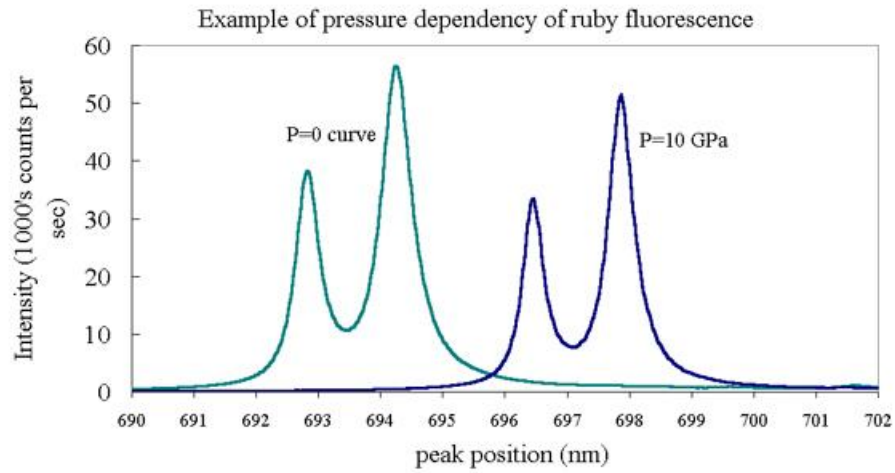


Figure 24. Example Ruby Fluorescence Spectrum

Example spectrum of ruby fluorescence depicting both emission lines observable with excitation of ruby. Two different pressures are shown to indicate the shift in the spectral lines as pressure is increased.

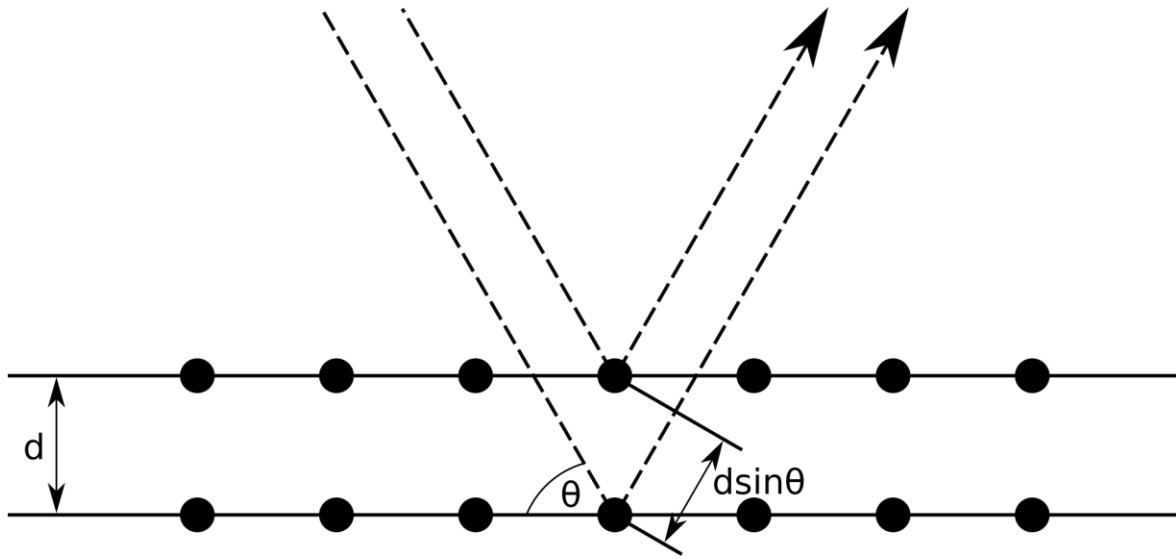


Figure 25. Bragg's law. [87]

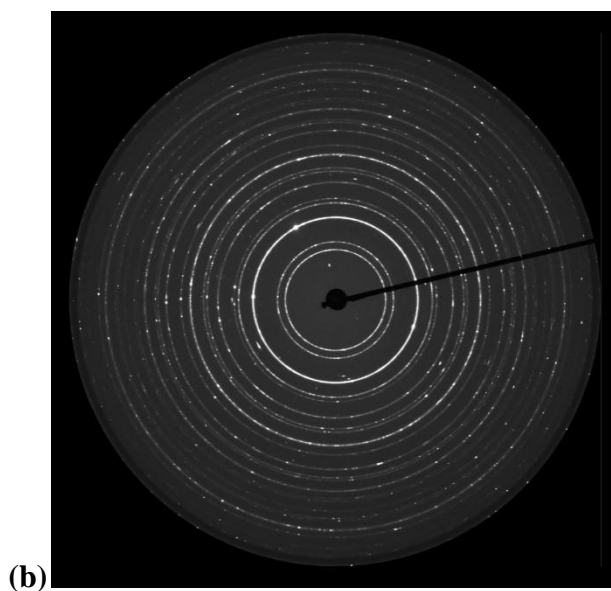
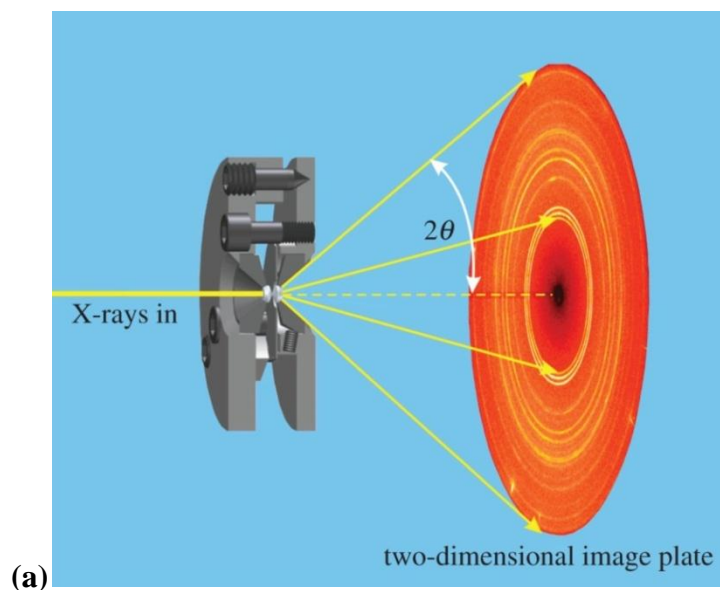


Figure 26. Example Powder XRD

(a) A schematic presenting the interaction of the incident X-rays with the sample placed within the diamond anvil cell producing diffraction cones at particular angles. (b) Example raw powder diffraction MAR-345 image taken from TiCoSb sample in a capillary at ambient pressure and temperature conditions. The image can be corrected for distortions such as brighter spots due to preferred orientation caused by uneven grain size of the powder [88].

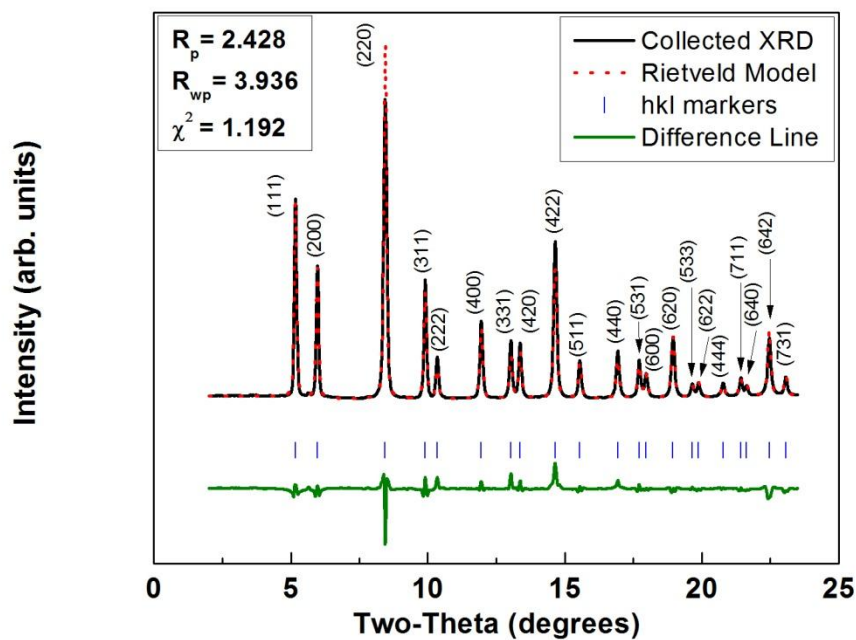


Figure 27. XRD Spectra Example

Example X-ray diffraction pattern after integration of MAR-345 image. The black line indicates the collected data, the red line represents a Rietveld refinement, the blue vertical markers represent the indexed hkl values, and the green line represents the difference between the calculated refinement and collected data.

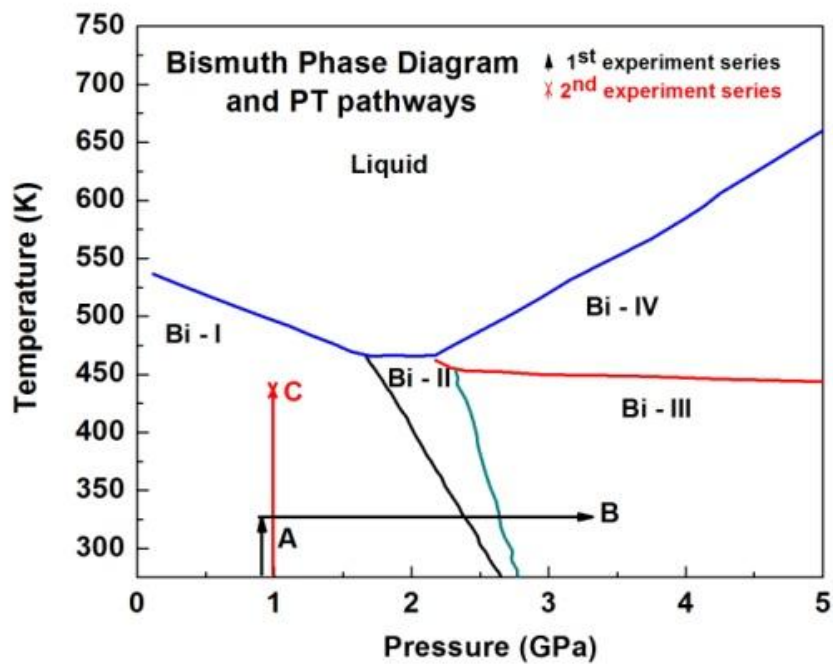


Figure 28. Bi – Phase Diagram.

Phase diagram of elemental Bi adapted from Chen *et al.* Arrows indicate pressure-temperature pathways taken during experiments [96].

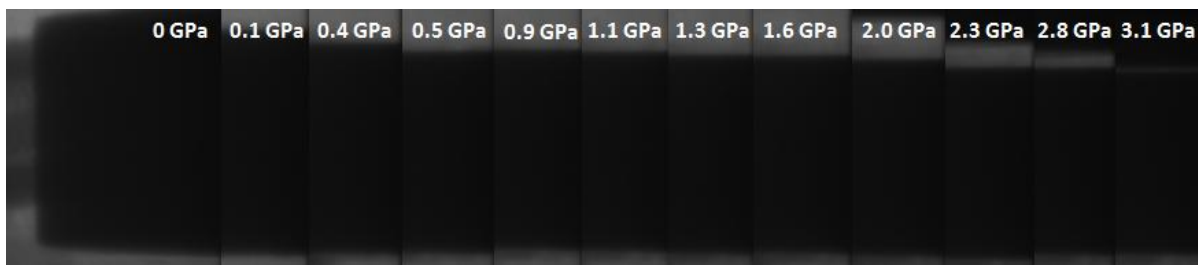


Figure 29. Bi – Radiography Images

Series of radiography images taken at edge of Bi sample during measurements. Sample thickness can be determined from these radiography images.

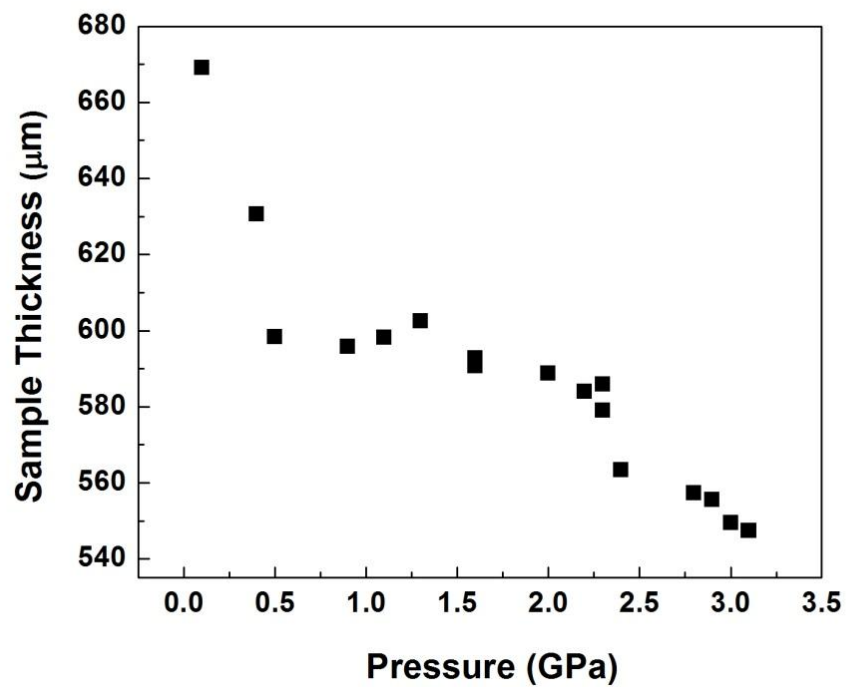
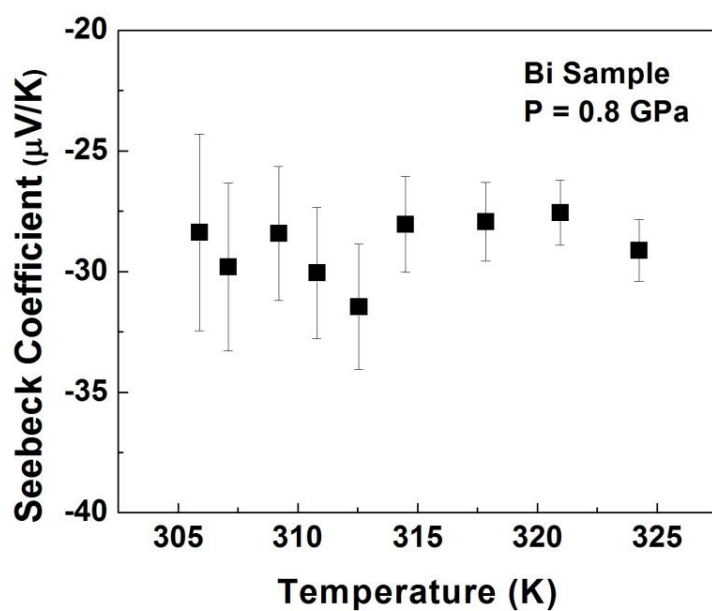
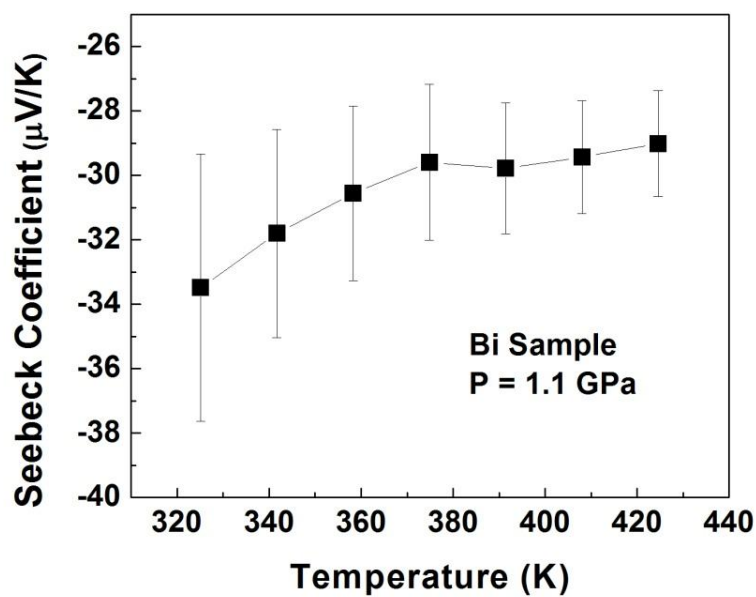


Figure 30. Bi – Sample Thickness vs Pressure

Sample thickness as a function of increasing pressure for the Bismuth sample.



(a)



(b)

Figure 31. Bi – Seebeck Coefficient vs Temperature

Isobaric Seebeck coefficient measurements for Bi at (a) 0.8 GPa and (b) 1.1 GPa from separate experimental runs.

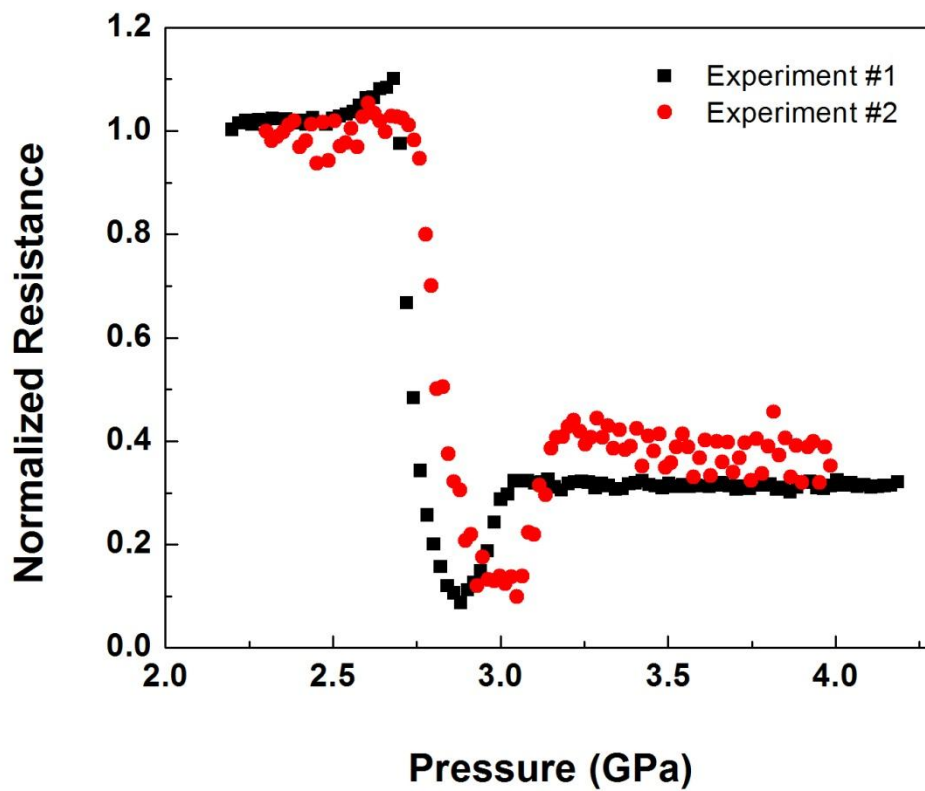


Figure 32. Bi – Normalized Electrical Resistance vs Pressure

Normalized electrical resistance as a function of increasing pressure for Bi sample. Two separate experiment runs are displayed to provide evidence of reproducibility of electrical measurements. Comparing both experiments, there is excellent qualitative agreement and both show distinct changes correlating to the phase boundaries of Bi.

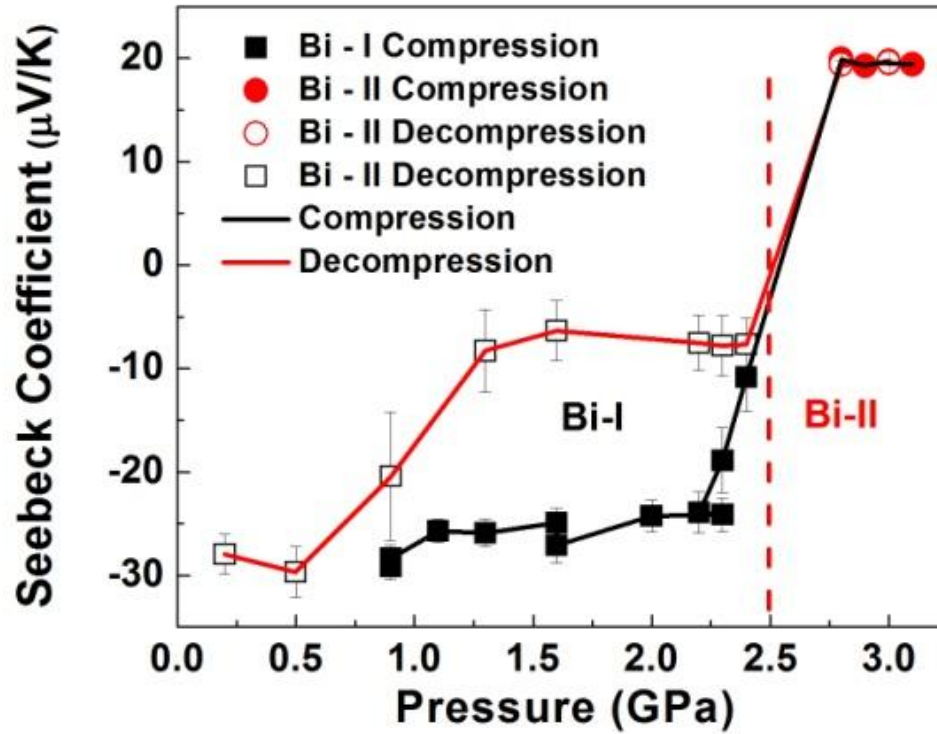


Figure 33. Bi – Seebeck Coefficient vs Pressure

Isothermal Seebeck coefficient measurements for compression and decompression of the bismuth sample at 325 K. The sharp variation and the change of sign of the Seebeck coefficient between 2 GPa and 2.7 GPa corresponds well with the Bi – I to Bi – II phase boundary (shown as the dotted line). A similar trend is observed with decompression, but with a large hysteresis. The errors are propagated from those of voltage values.

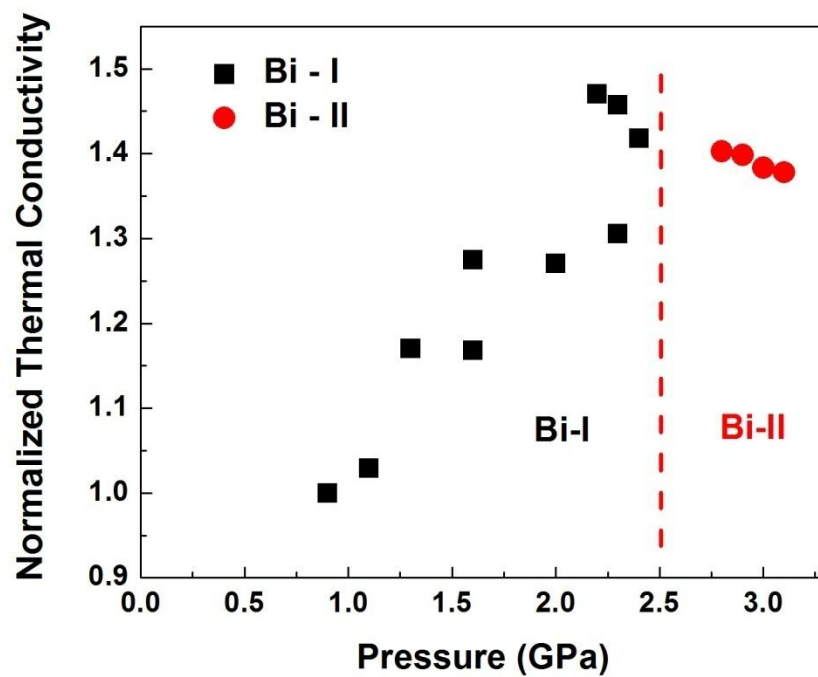


Figure 34. Bi – Normalized Thermal Conductivity vs Pressure

The relative change in the thermal conductance for compression of bismuth at 325 K. The abrupt trend reversal at 2.5 GPa corresponds with the Bi – I to Bi – II transition in bismuth.

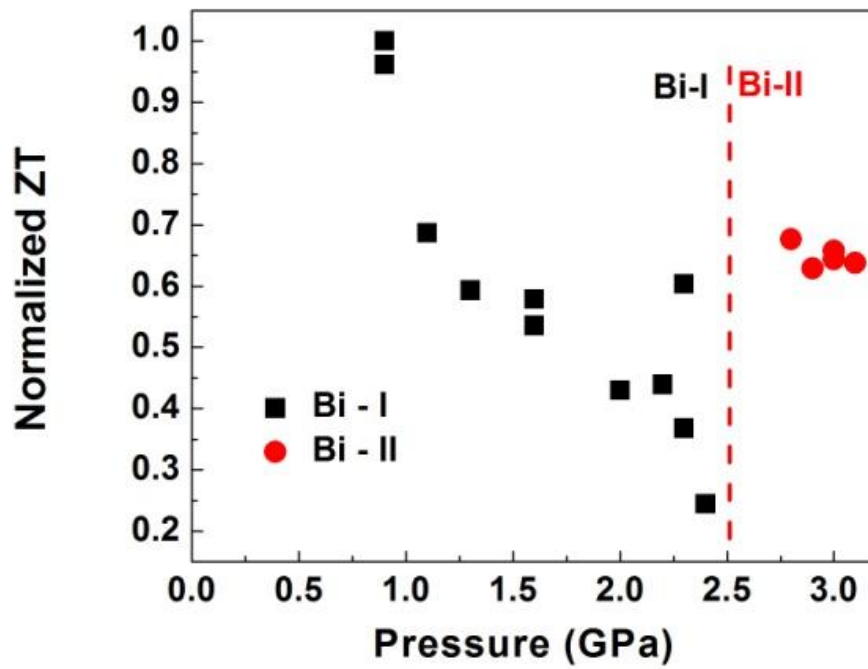


Figure 35. Bi – Normalized ZT vs Pressure

The relative change in the figure of merit (normalized by the largest value), ZT, for compression for bismuth. The discontinuity in the trend at around 2.5 GPa is consistent with those observed in the Seebeck and thermal measurements.

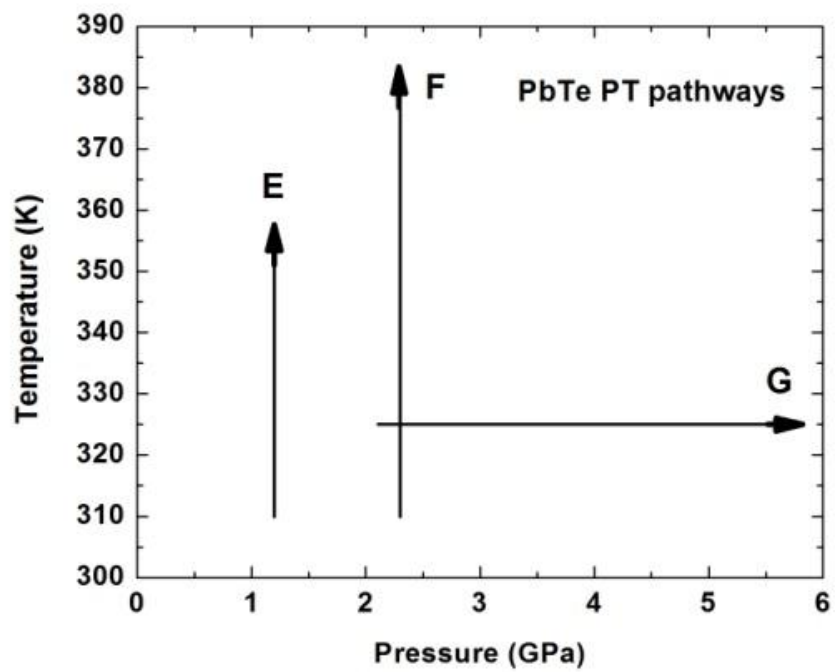


Figure 36. PbTe – P-T Pathways

Pressure and temperature pathways taken in PbTe measurements.

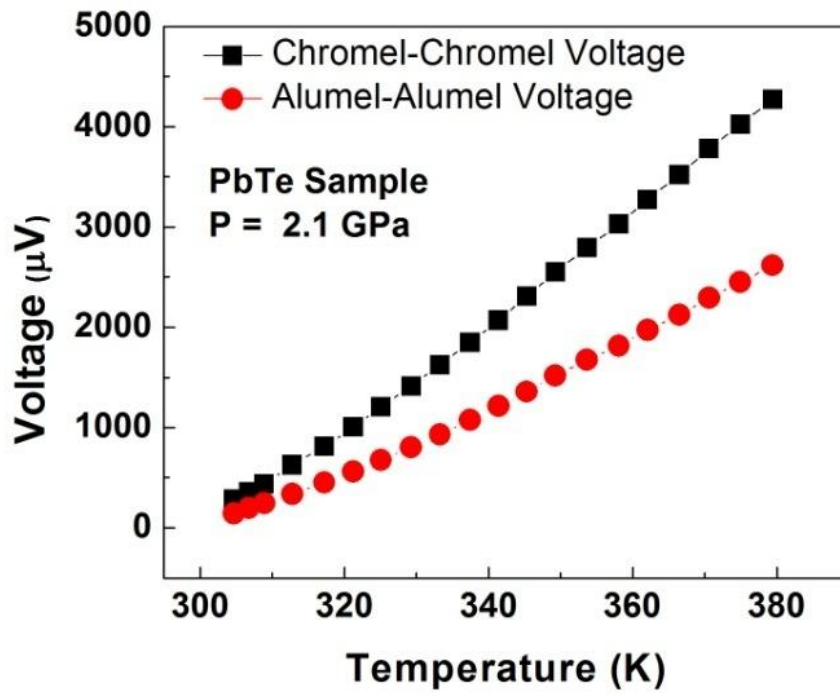
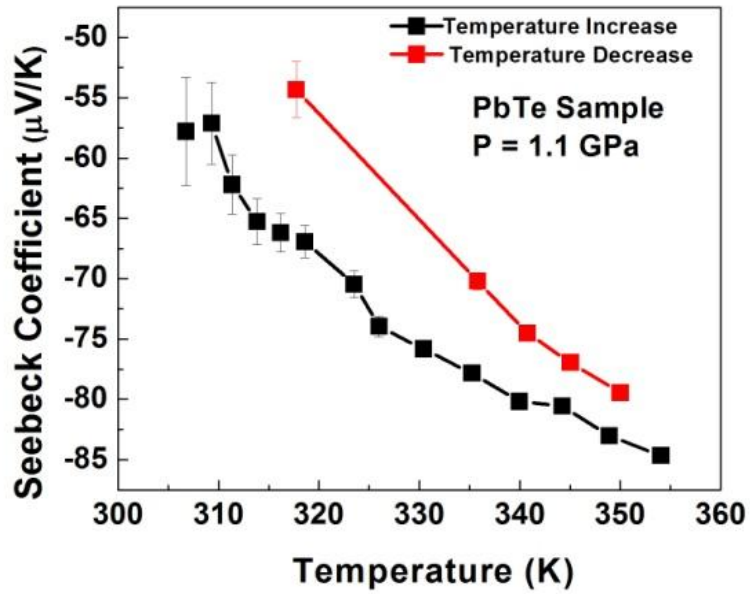
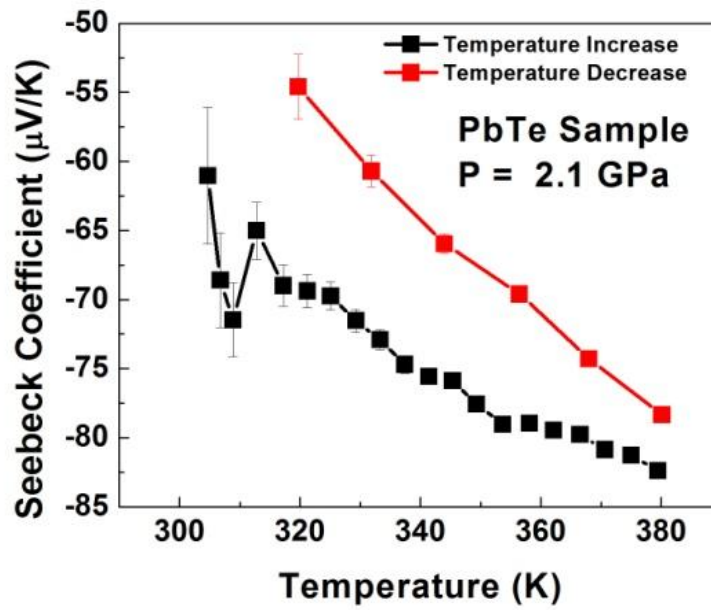


Figure 37. PbTe – Thermoelectric EMF vs Temperature

Example of thermoelectric voltages measured for PbTe at 2.1 GPa from 300 – 380 K.



(a)



(b)

Figure 38. PbTe – Seebeck Coefficient vs Temperature

Seebeck coefficient as a function of increasing and decreasing temperature for PbTe at (a) 1.0 GPa and (b) 2.1 GPa.

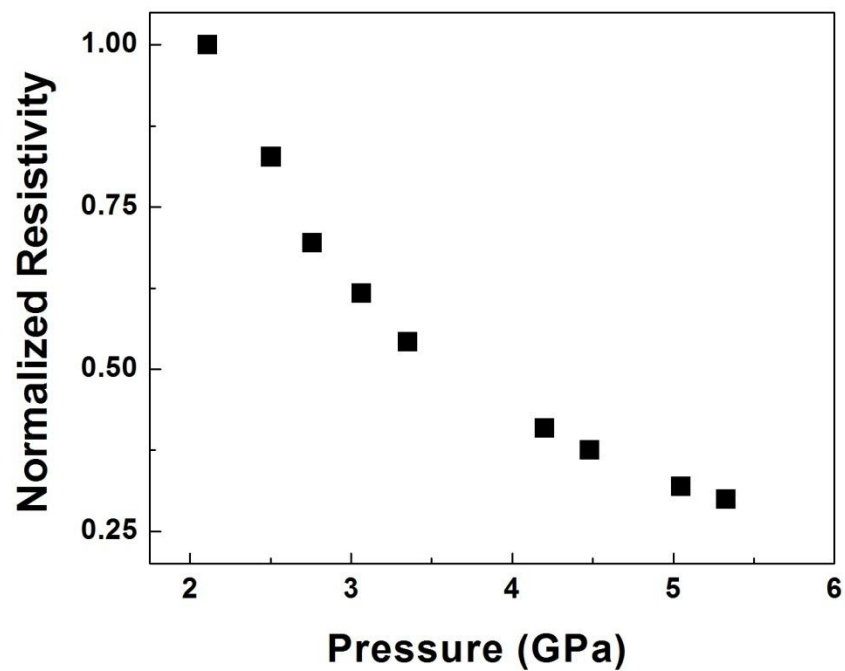


Figure 39. PbTe – Normalized Electrical Resistivity vs Pressure

Electrical resistivity as a function of increasing pressure from 2.0 GPa to 5.5 GPa at 325 K for PbTe sample.

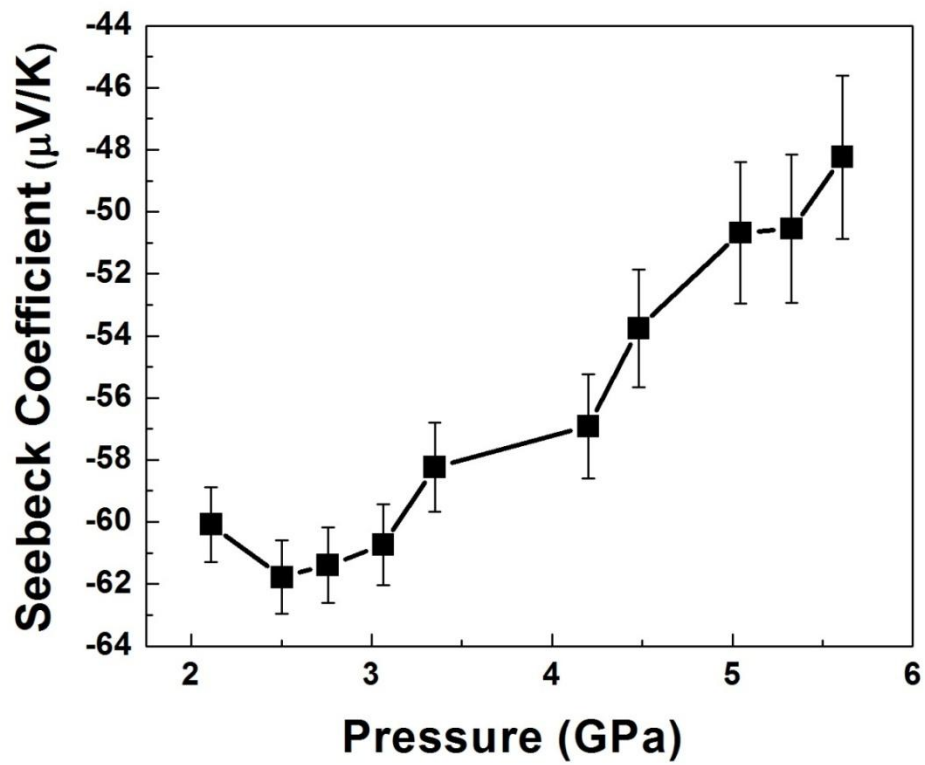


Figure 40. PbTe – Seebeck Coefficient vs Pressure

Seebeck coefficient as a function of pressure from 2 GPa to 5.5 GPa at 325 K for PbTe sample.

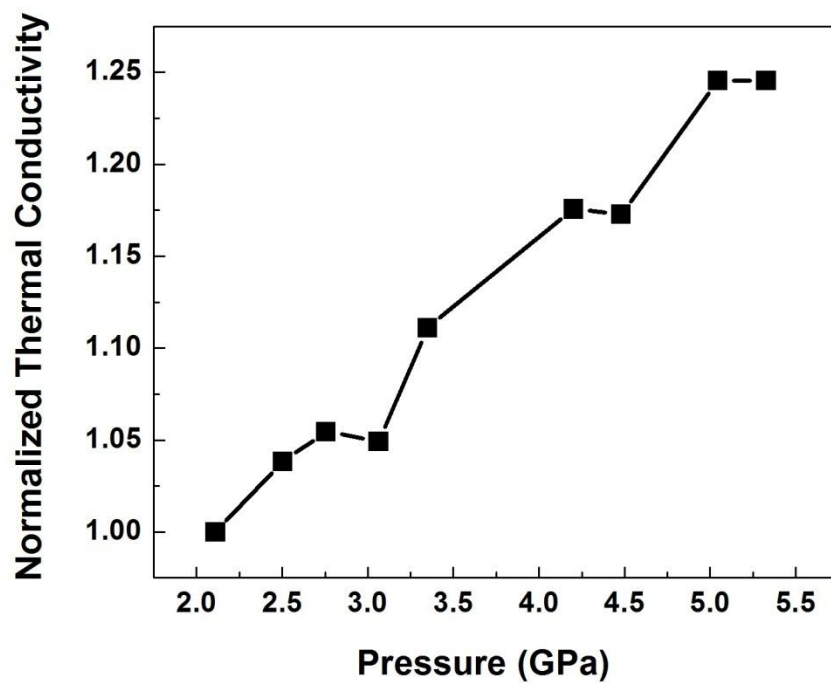


Figure 41. PbTe – Normalized Thermal Conductivity vs Pressure

Relative changes in thermal conductivity at 325 K as a function of increasing pressure for PbTe sample.

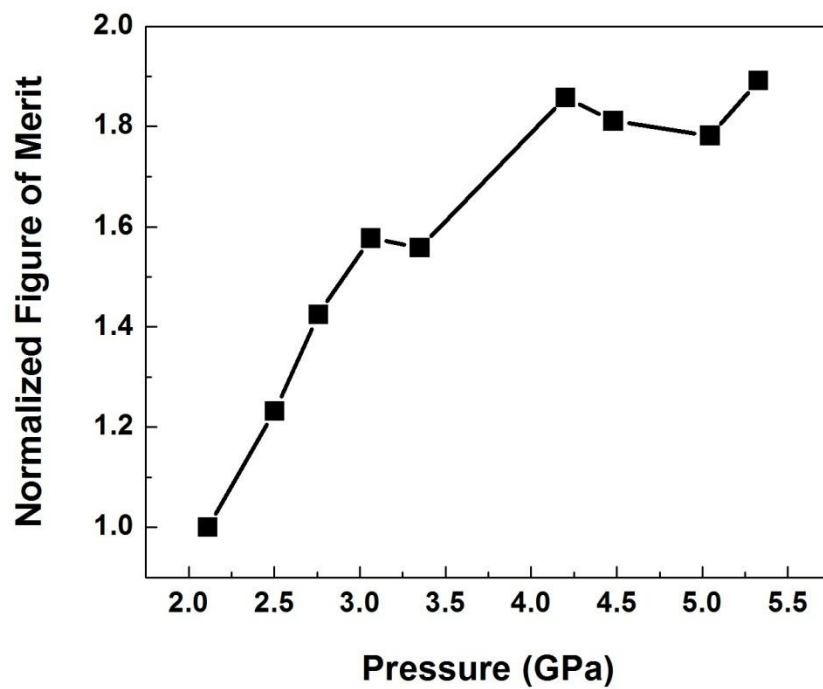


Figure 42. PbTe – Normalized ZT vs Pressure

Relative changes in the dimensionless figure of merit, ZT at 325 K for PbTe as a function of increasing pressure.

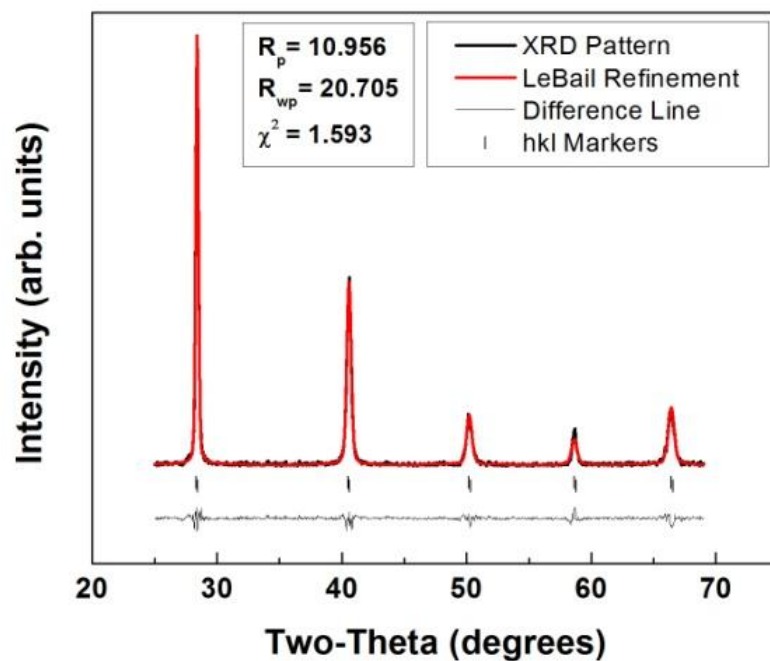


Figure 43. SnTe – Ambient XRD Spectrum

Ambient pressure and temperature X-ray diffraction pattern of SnTe using Cu k- α source ($\lambda = 1.5418 \text{ \AA}$). The black solid line represents the collected XRD pattern for the SnTe sample and the dotted red line represents the results of a LeBail refinement performed with the collected XRD data. The black horizontal lines below the XRD pattern represent the hkl values for the indexed peaks corresponding to the $Fm-3m$ structure. The line at the bottom of the plot represents the residual calculated between the collected data and the LeBail refinement.

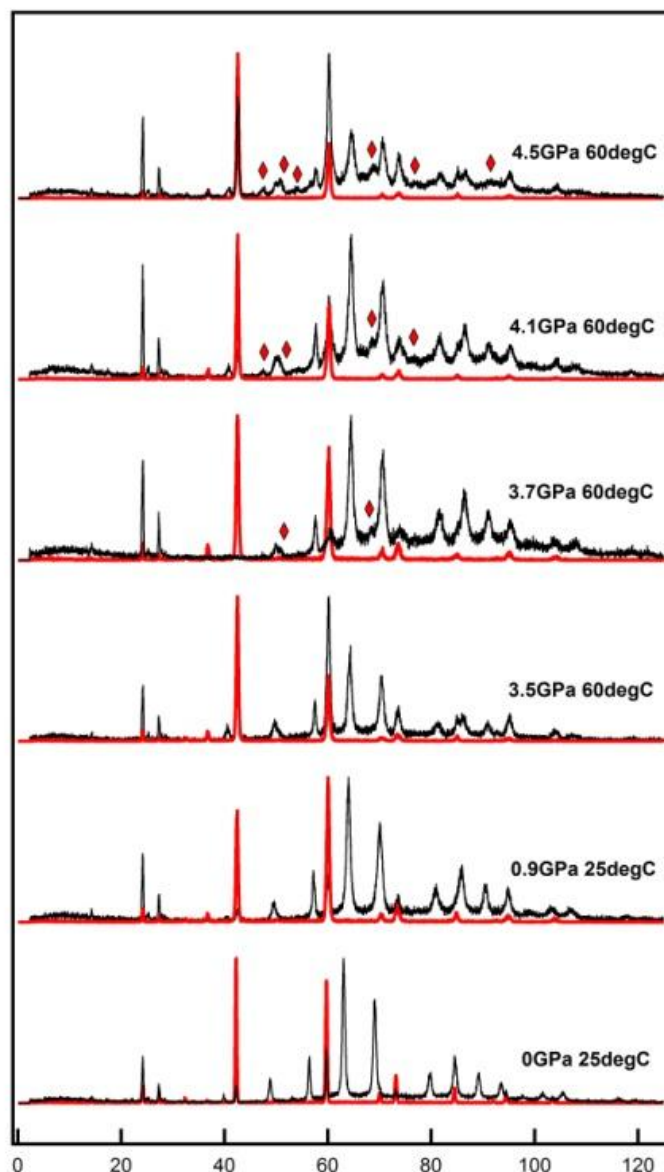


Figure 44. SnTe – EDXRD Spectra vs Pressure

Energy-dispersive X-ray diffraction spectra for SnTe (black) and MgO (red). The MgO spectra are plotted as a reference to identify the small MgO peaks present in the sample spectra. The red diamonds indicate new peaks appearing not associated with the SnTe ambient crystal structure or the MgO crystal structure, thus indicating the onset of a pressure-induced structural phase transformation.

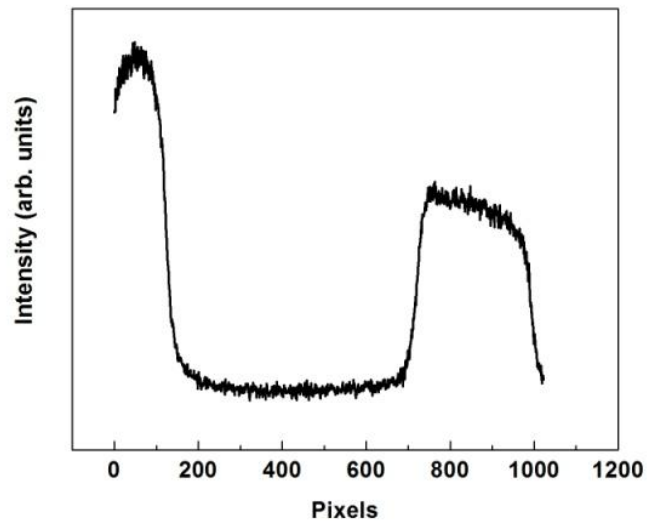


Figure 45. SnTe – Radiography Image

(a) Radiography image of SnTe at 2.2 GPa. The arrow indicates the path for the intensity profile to determine thickness of the sample. **(b)** Intensity profile corresponding to the arrowed path in the radiography image. Sample thickness can be calculated by determining the number of pixels between edges and applying calibrated conversion ratio of 0.95 $\mu\text{m}/\text{pixel}$.

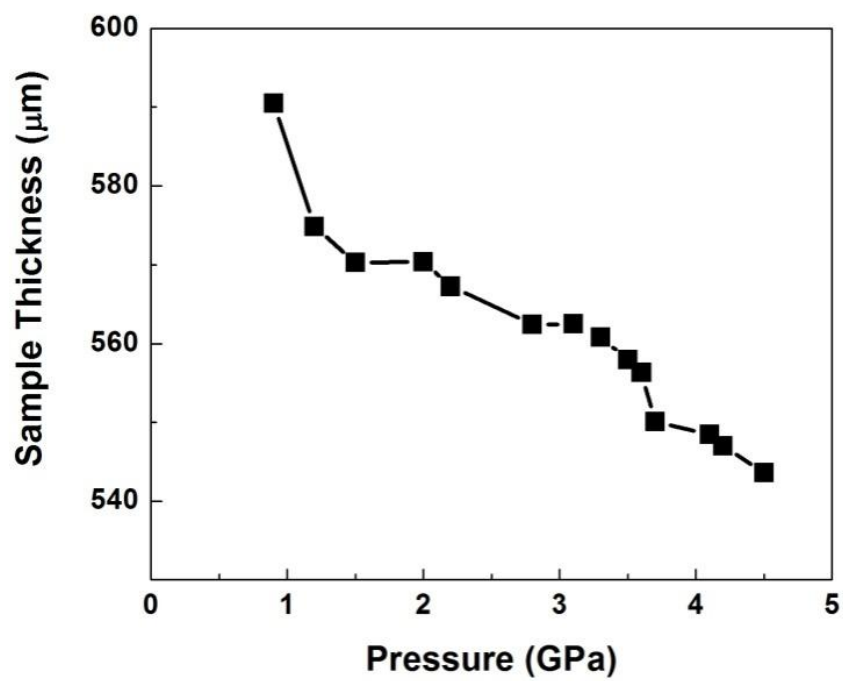


Figure 46. SnTe – Sample Thickness vs Pressure

Sample thickness as a function of increasing pressure for SnTe.

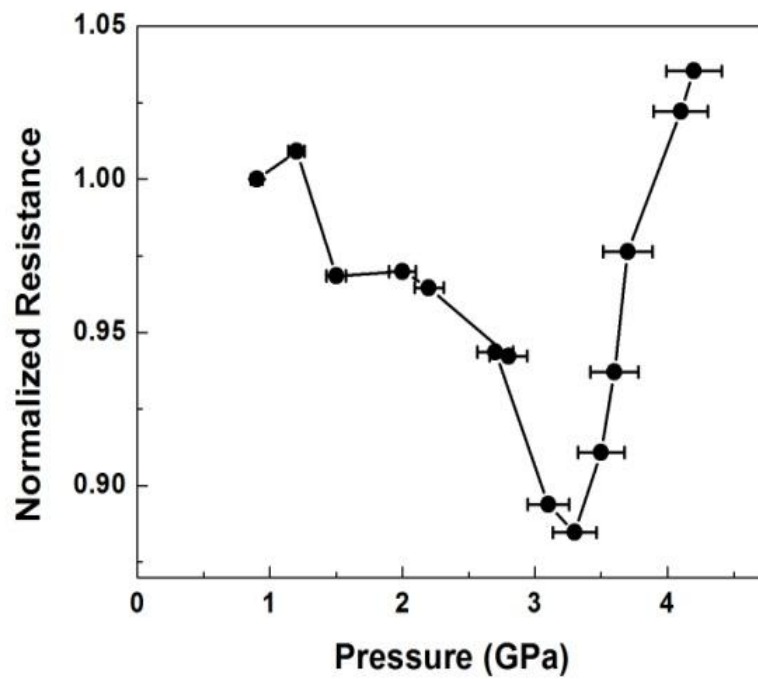


Figure 47. SnTe – Normalized Electrical Resistance vs Pressure

Pressure variation of the normalized electrical resistance for SnTe at 330K up to 4.5 GPa.

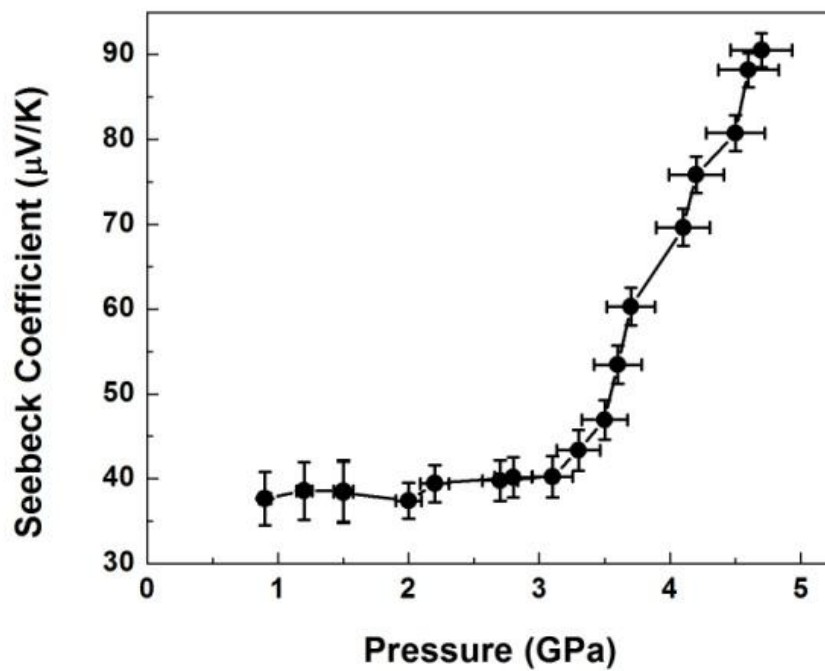


Figure 48. SnTe – Seebeck Coefficient vs Pressure

Pressure variation in the Seebeck coefficient for SnTe at 330K up to 4.5 GPa. A huge increase up to 230% starts above 3.2 GPa, corresponding to a structural phase transition.

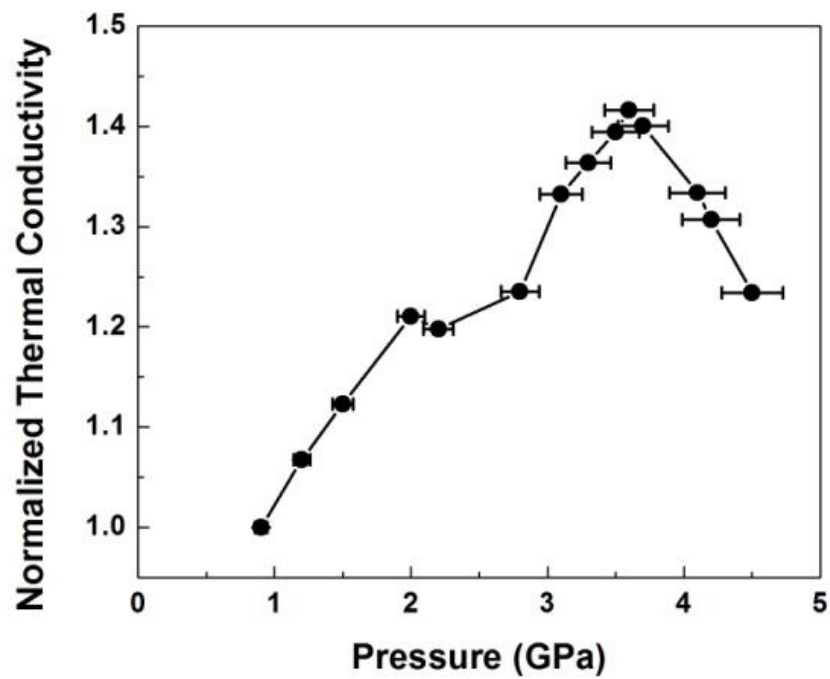


Figure 49. SnTe – Normalized Thermal Conductivity vs Pressure

Pressure effect on the relative changes to thermal conductivity for SnTe at 330K up to 4.5 GPa.

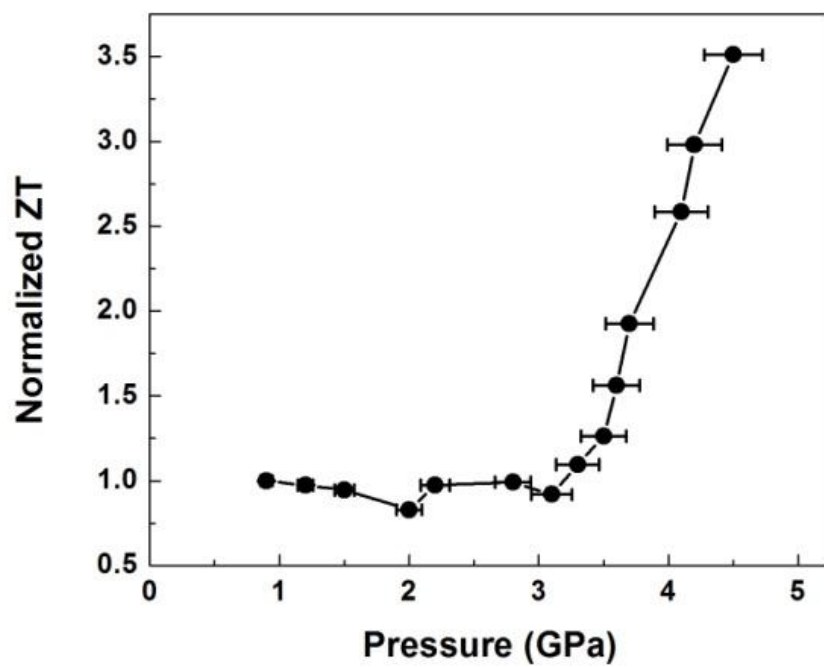


Figure 50. SnTe – Normalized ZT vs Pressure

Pressure variation of the relative changes in ZT for SnTe at 330K up to 4.5 GPa.

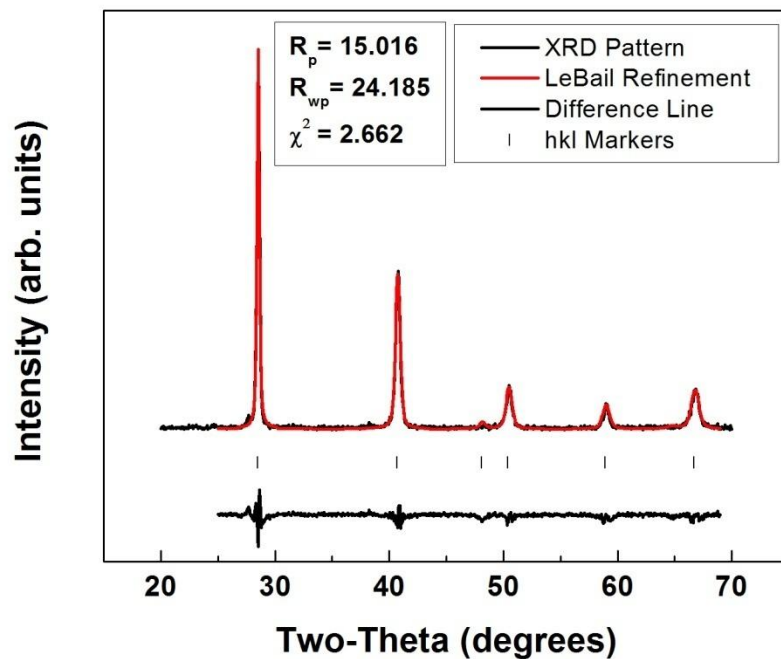


Figure 51. $\text{Sn}_{1-x}\text{Mn}_x\text{Te}$ ($x = 12\%$) – Ambient XRD Spectrum

Ambient pressure and temperature XRD pattern for $\text{Sn}_{1-x}\text{Mn}_x\text{Te}$ ($x = 12\%$) sample. The red line represents the calculated LeBail refinement performed to match the collected data, which is shown as the black line. Beneath the XRD pattern, the vertical lines represent the hkl markers corresponding to the ambient pressure and temperature $Fm-3m$ crystal structure. The solid black line underneath the hkl markers represents the difference between the observed data and the calculated refinement.

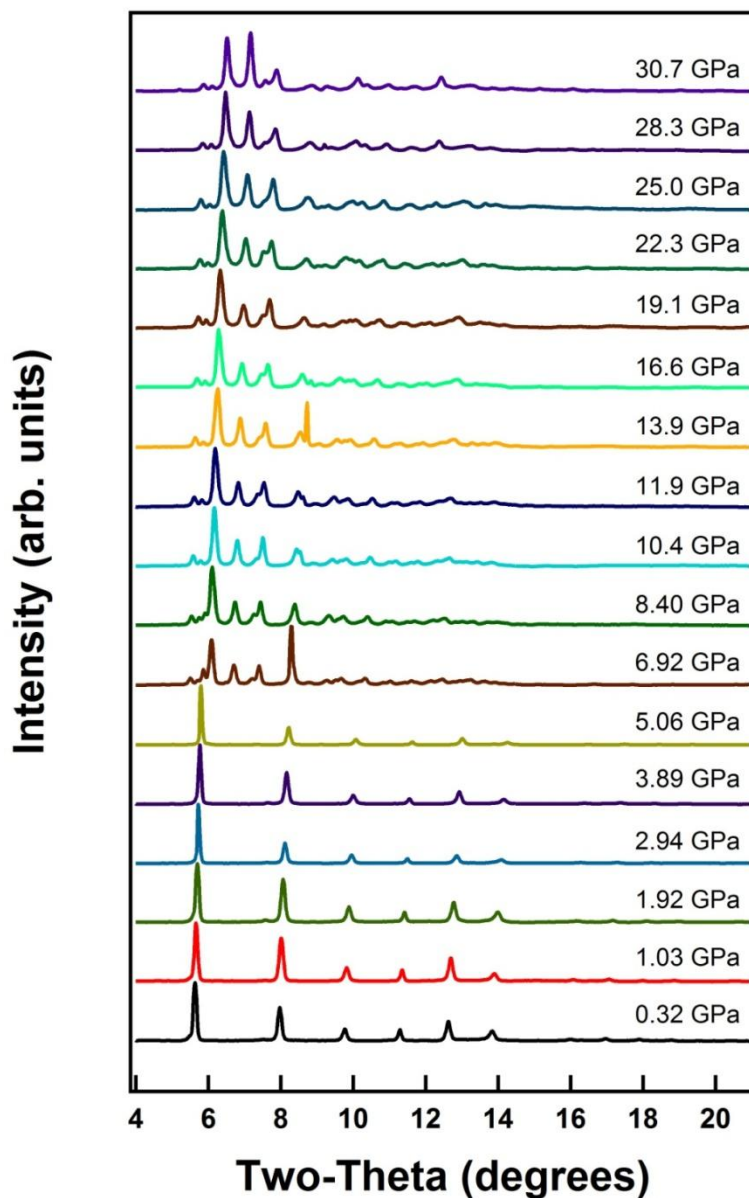
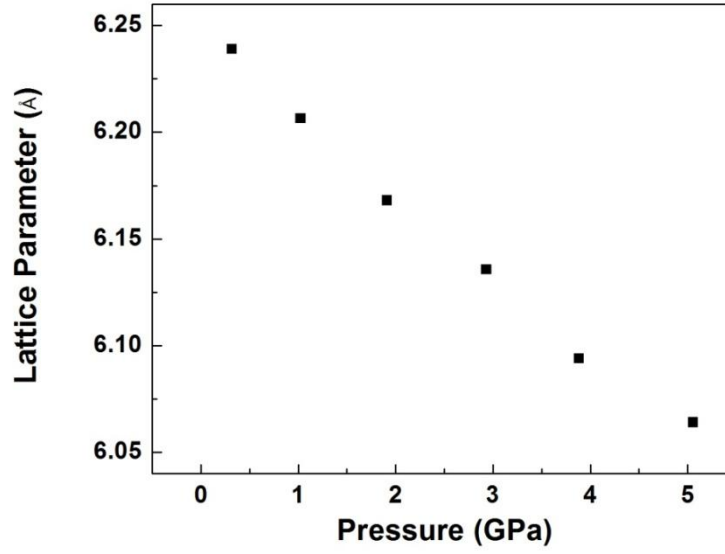
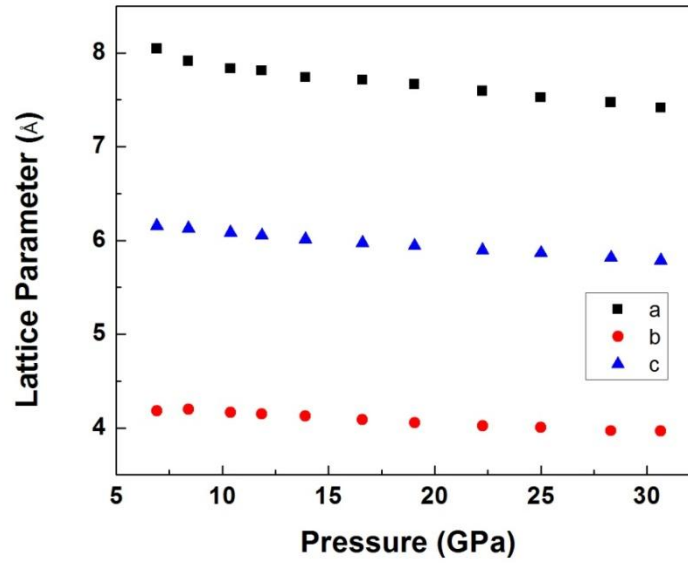


Figure 52. $\text{Sn}_{1-x}\text{Mn}_x\text{Te}$ ($x = 12\%$) – XRD Spectra vs Pressure

High pressure XRD patterns for $\text{Sn}_{1-x}\text{Mn}_x\text{Te}$ ($x = 12\%$) from 0.32 GPa to 30.7 GPa. Clear indication of a structural phase transition is observed at 6.92 GPa from the ambient $Fm-3m$ crystal structure to a $Pnma$ crystal structure. This phase transition is also observed in pure-SnTe in published literature at lower pressure (~ 4 GPa).



(a)



(b)

Figure 53. $\text{Sn}_{1-x}\text{Mn}_x\text{Te}$ ($x = 12\%$) – Lattice Parameters vs Pressure

Plot of unit-cell lattice parameters for the (a) low pressure ambient $Fm-3m$ crystal structure and the (b) high pressure $Pnma$ crystal structure for $\text{Sn}_{1-x}\text{Mn}_x\text{Te}$ ($x = 12\%$).

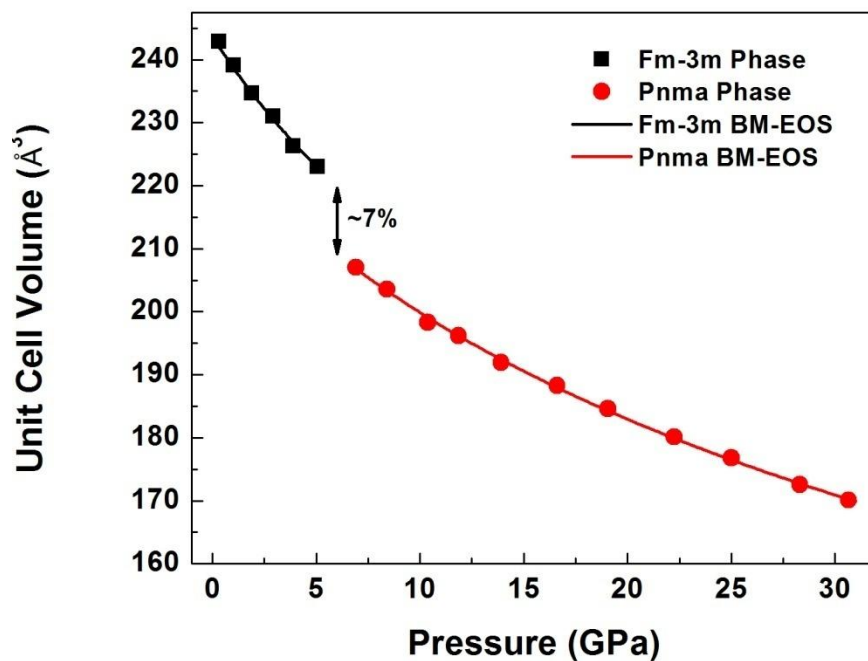


Figure 54. $\text{Sn}_{1-x}\text{Mn}_x\text{Te}$ ($x = 12\%$) – Unit Cell Volume vs Pressure

Plot of the unit-cell volume for both the low pressure and high pressure phases as a function of increasing pressure for $\text{Sn}_{1-x}\text{Mn}_x\text{Te}$ ($x = 12\%$). A volume collapse of 7%, as indicated, is observed during the pressure-induced structural phase transition which is slightly larger than observed in pure-SnTe.

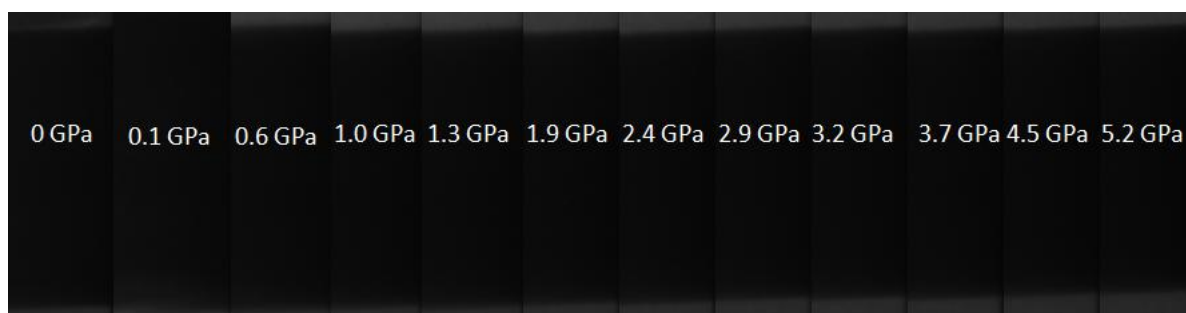


Figure 55. $\text{Sn}_{1-x}\text{Mn}_x\text{Te}$ ($x = 12\%$) – Radiography Images

Radiography images depicting change in sample thickness as a function of increasing pressure.

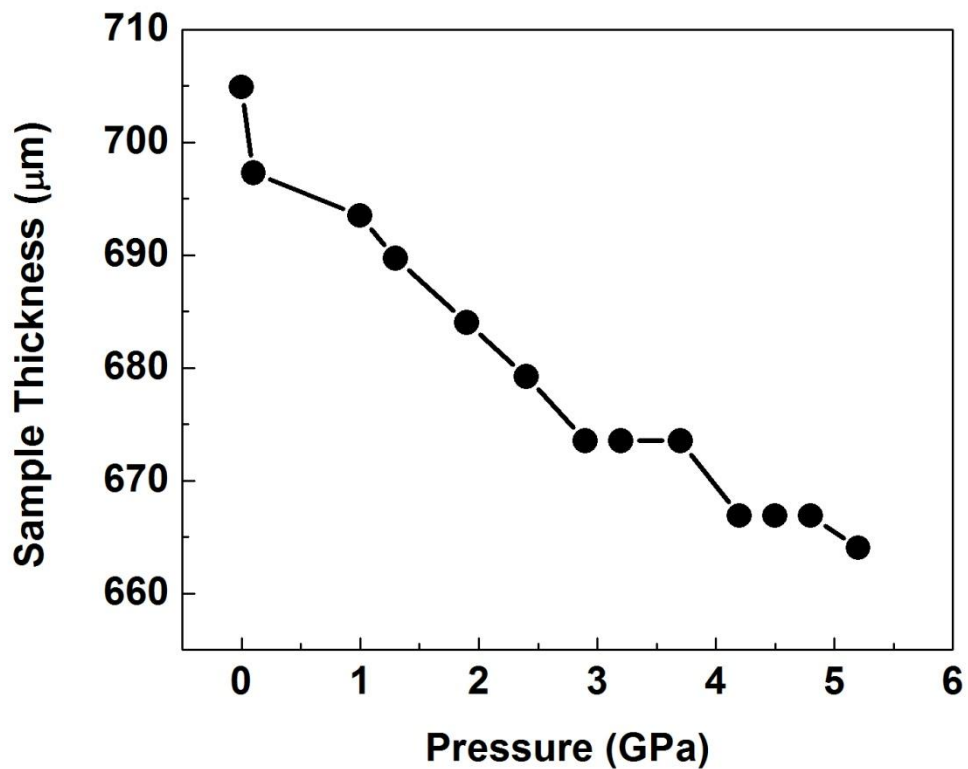


Figure 56. $\text{Sn}_{1-x}\text{Mn}_x\text{Te}$ ($x = 12\%$) – Sample Thickness vs Pressure

A plot of the sample thickness determined from analysis of the radiography images as a function of increasing pressure.

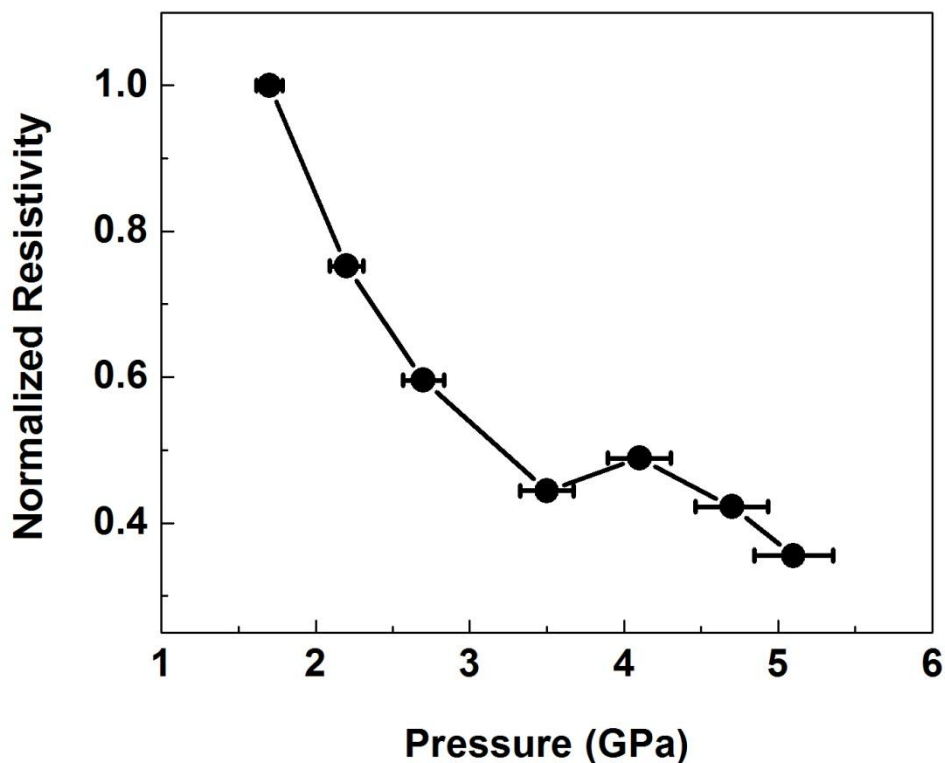


Figure 57. $\text{Sn}_{1-x}\text{Mn}_x\text{Te}$ ($x = 12\%$) – Normalized Electrical Resistivity vs Pressure

Plot of the normalized electrical resistivity as a function of increasing pressure for $\text{Sn}_{1-x}\text{Mn}_x\text{Te}$ ($x = 12\%$). A fairly steady decrease is observed over the pressure range studied. The small increase at 3.5 GPa may be an indication of influence from the structural phase transition observed in pure-SnTe, but this transition does not seem to occur until higher pressure in this Mn-doped SnTe sample.

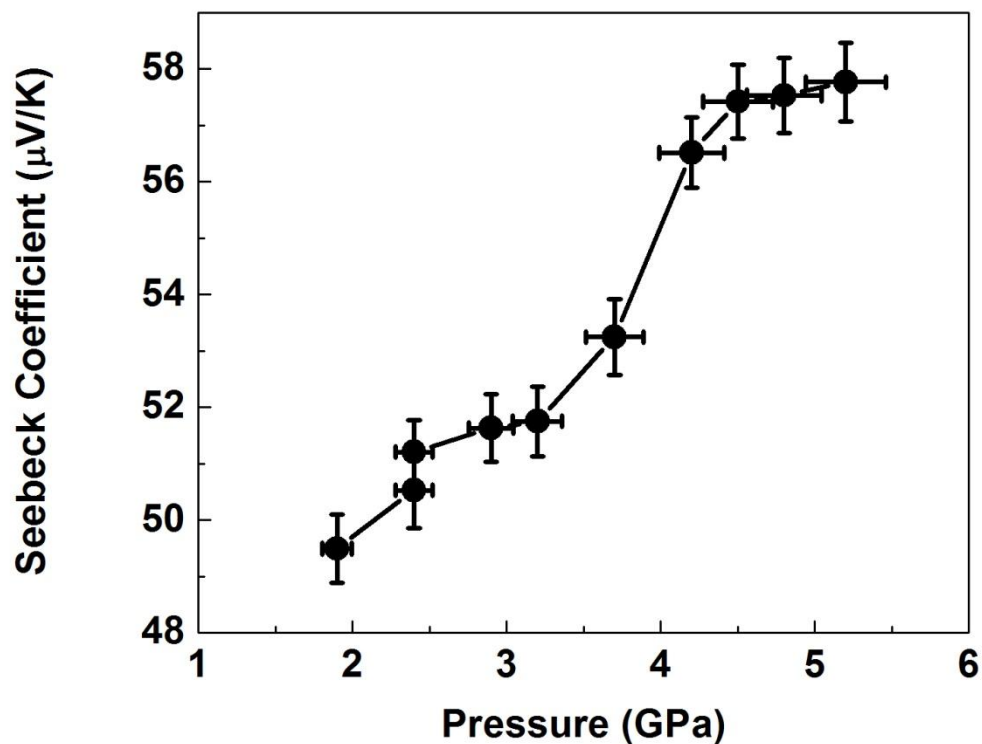


Figure 58. $\text{Sn}_{1-x}\text{Mn}_x\text{Te}$ ($x = 12\%$) – Seebeck Coefficient vs Pressure

Plot of the Seebeck coefficient as a function of increasing pressure for $\text{Sn}_{1-x}\text{Mn}_x\text{Te}$ ($x = 12\%$). A steady increase from 2 GPa to 5 GPa is observed corresponding to a 14% increase in the Seebeck coefficient.

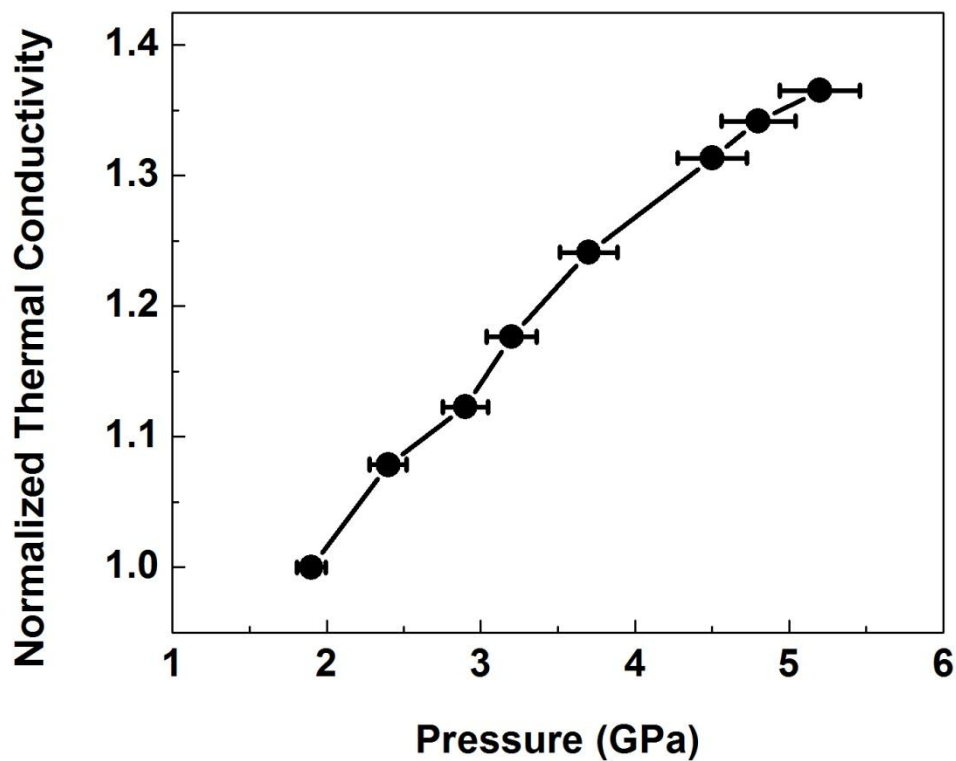


Figure 59. $\text{Sn}_{1-x}\text{Mn}_x\text{Te}$ ($x = 12\%$) – Normalized Thermal Conductivity vs Pressure

Plot of the normalized thermal conductivity measurement results as a function of increasing pressure for $\text{Sn}_{1-x}\text{Mn}_x\text{Te}$ ($x = 12\%$). The trend in the thermal conductivity is observed to steadily increase over the entire pressure range measured with a 35% increase

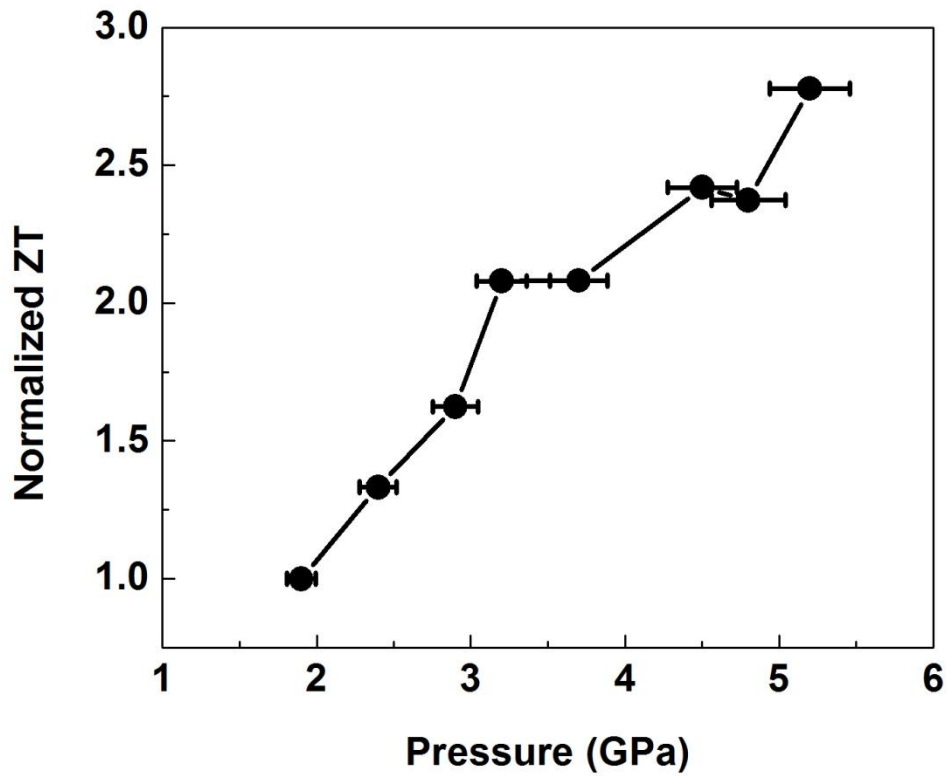


Figure 60. $\text{Sn}_{1-x}\text{Mn}_x\text{Te}$ ($x = 12\%$) – Normalized ZT vs Pressure

Plot of the normalized ZT value as a function of increasing pressure for $\text{Sn}_{1-x}\text{Mn}_x\text{Te}$ ($x = 12\%$).

A large increase over the entire pressure range is observed and is due to the large decrease in electrical resistivity observed in our experiments.

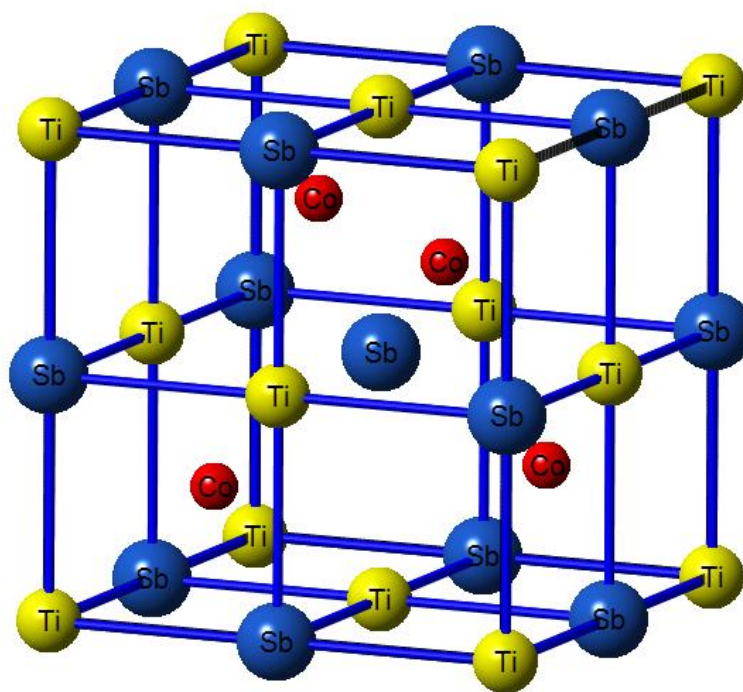


Figure 61. TiCoSb – Ambient Crystal Structure

The MgAgAs ambient pressure and temperature structure of TiCoSb.

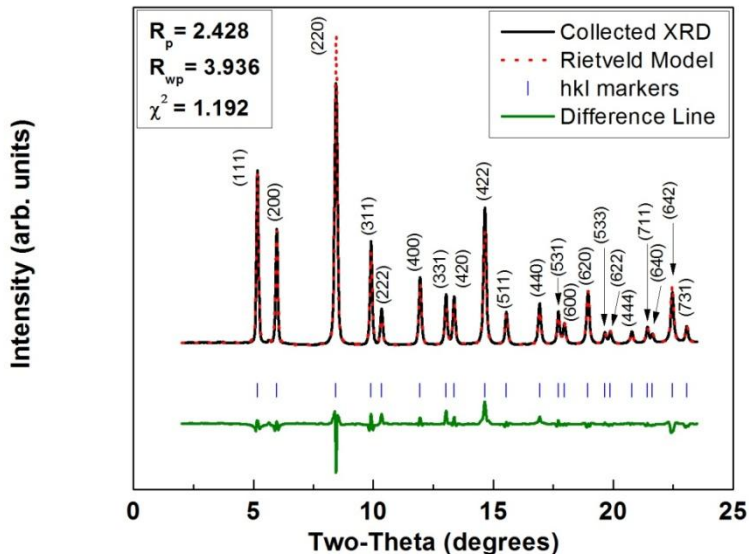


Figure 62. TiCoSb – Ambient XRD Spectrum

Ambient pressure and temperature X-ray diffraction pattern of TiCoSb. A Rietveld refinement (dotted red line) was performed to model the collected data (solid black line) which has been indexed to the MgAgAs structure with reflections shown as solid blue lines under the XRD pattern. The green solid line at the bottom indicates the difference between the Rietveld refinement and the collected data.

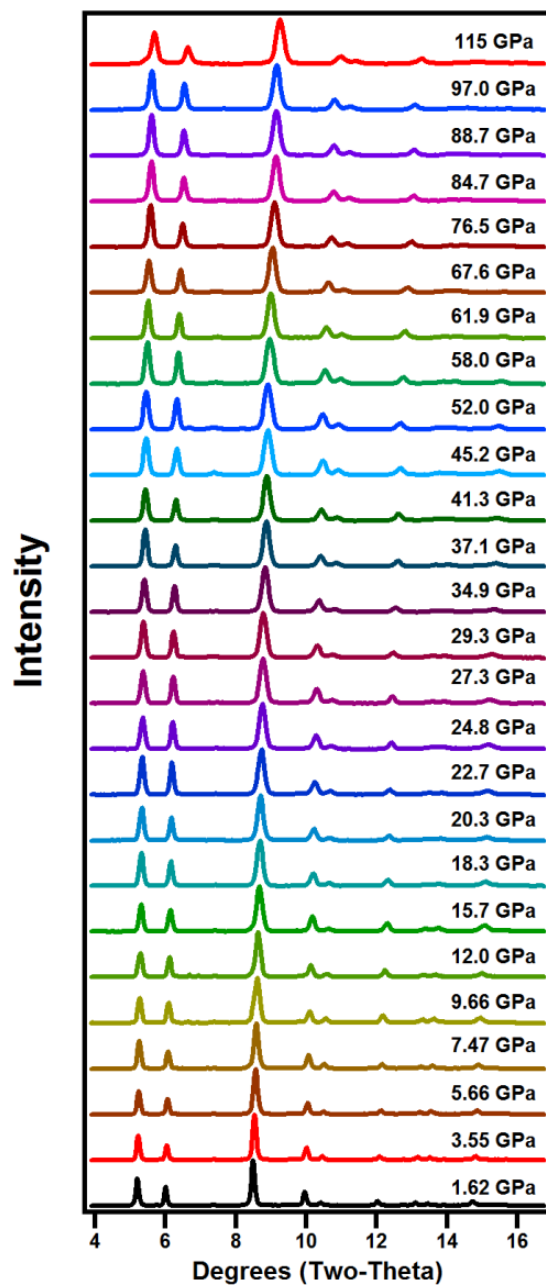


Figure 63. TiCoSb – XRD Spectra vs Pressure

High-pressure X-ray diffraction patterns of TiCoSb. No evidence of a pressure-induced structural phase transition is observed over the entire pressure range, and as such, TiCoSb remains in the ambient cubic structure with $F-43m$ space group up to 115 GPa.

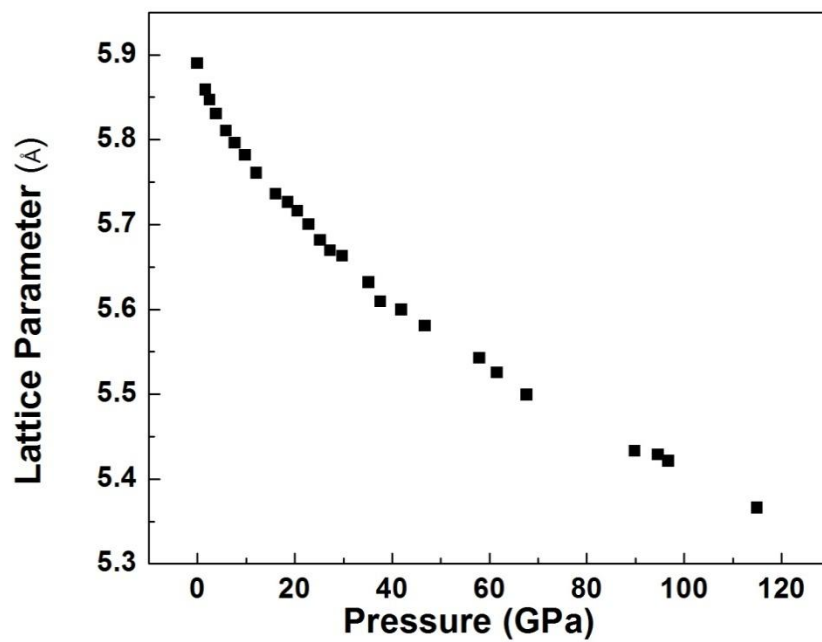


Figure 64. TiCoSb – Lattice Parameter vs Pressure

Plot of the cell parameter, a , as a function of increasing pressure for TiCoSb sample.

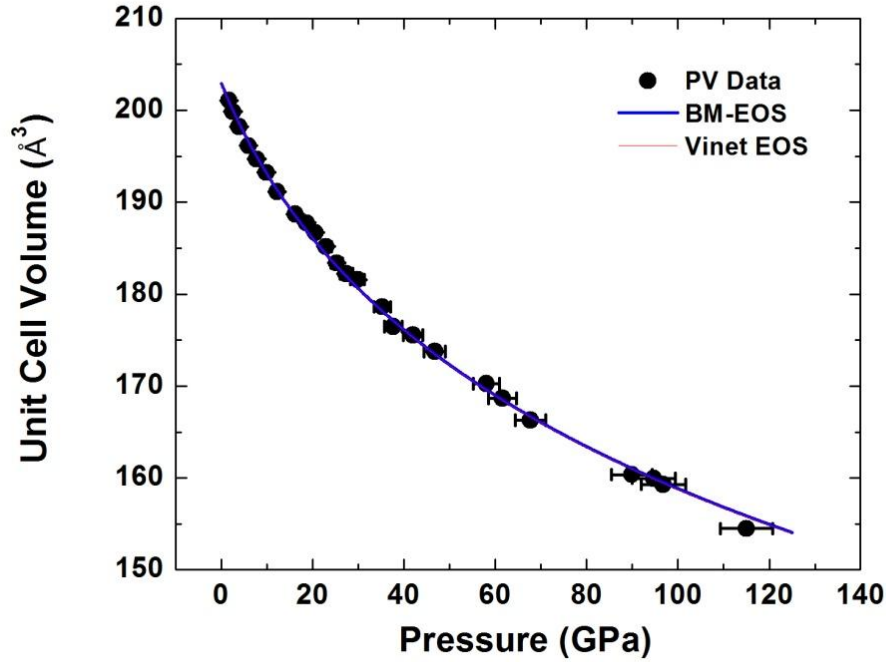


Figure 65. TiCoSb – Unit Cell Volume vs Pressure

Plot of the unit-cell volume as a function of pressure. The black solid circles represent the TiCoSb data as measured in this study. The x-error bar represents a 5% uncertainty in the pressure and the y-error bar is smaller than the data points. The solid blue line represents a 3rd – order Birch-Murnaghan equation of state fit to the experimental data and the solid red line represent the Vinet EOS fit to the experimental data. The fit parameters are displayed indicating the initial unit cell volume, the bulk modulus, and the pressure-derivative of the bulk modulus.

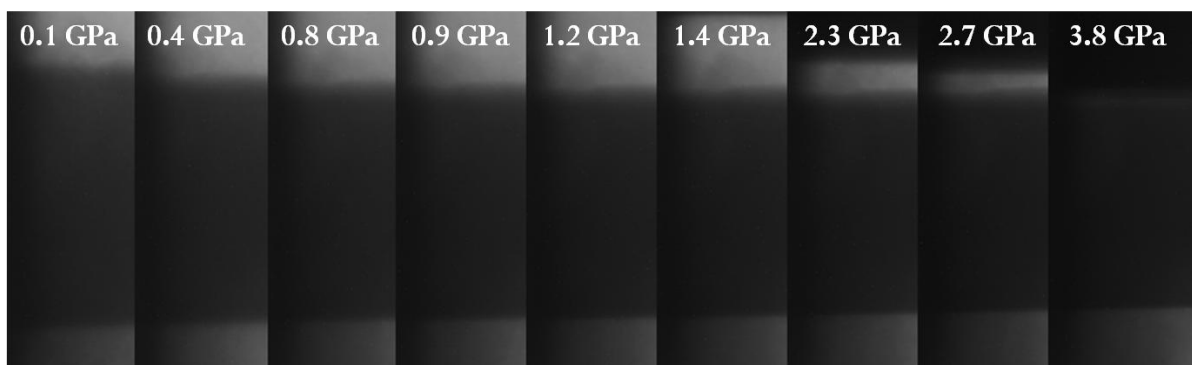


Figure 66. TiCoSb – Radiography Images

Series of radiography images depicting the sample thickness decreasing as pressure is increased for TiCoSb. The radiography images are taken at the edge of the sample.

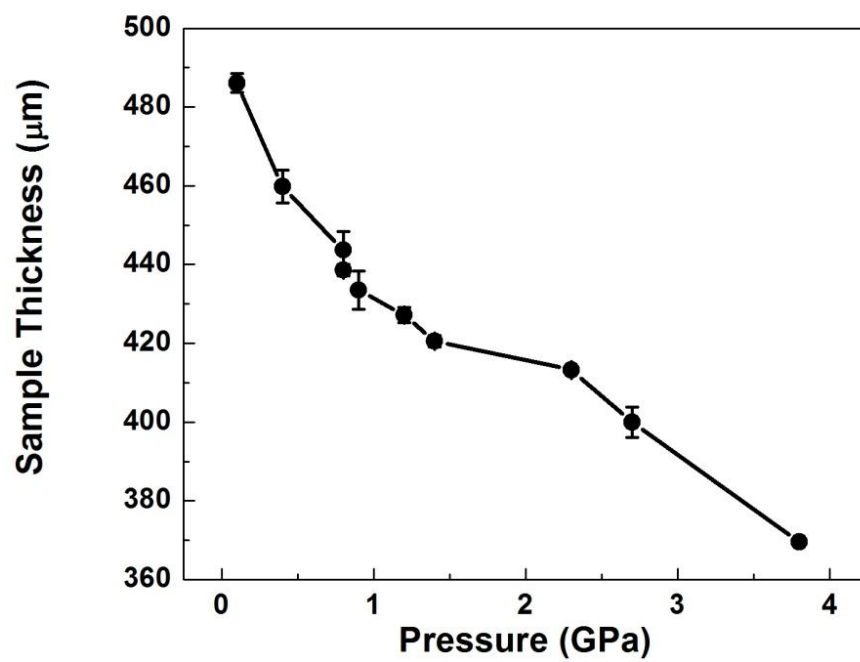


Figure 67. TiCoSb – Sample Thickness vs Pressure

A plot of the sample thickness determined from analysis of the radiography images as a function of increasing pressure for TiCoSb.

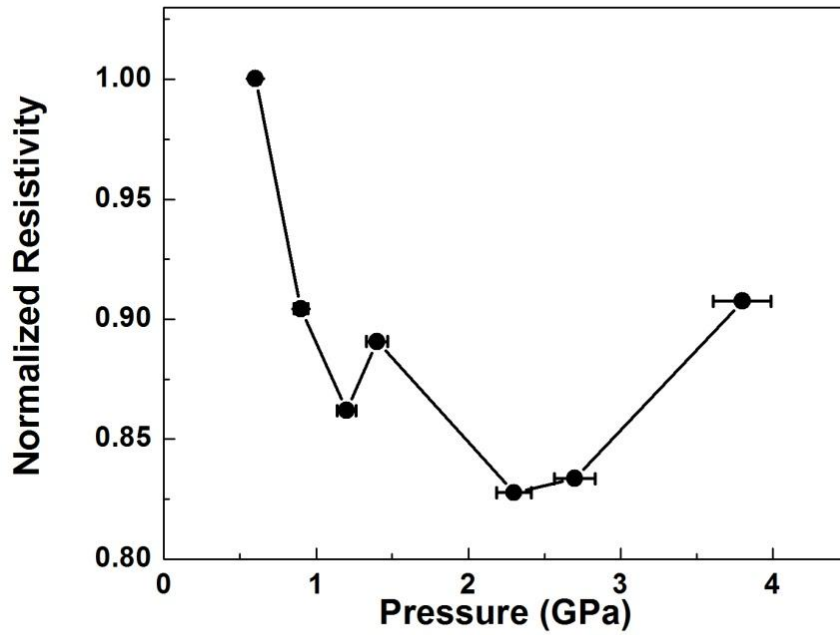


Figure 68. TiCoSb – Normalized Electrical Resistivity vs Pressure

Normalized electrical resistivity as a function of pressure for TiCoSb. A maximum decrease of 18% is observed at 2 GPa, with an increasing trend beginning and maintaining until the maximum pressure (4 GPa). This indicates a favorable effect of pressure on the thermoelectric efficiency up to 2.3 GPa with a negative effect at increasing pressures.

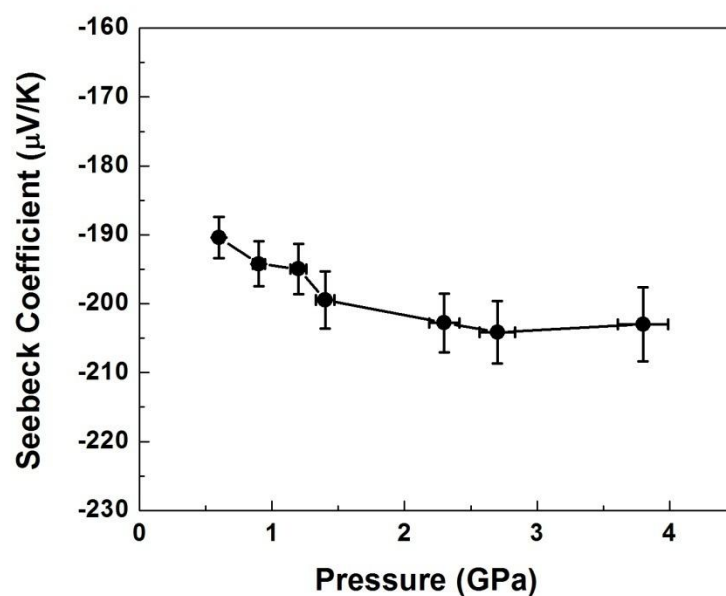


Figure 69. TiCoSb – Seebeck Coefficient vs Pressure

The variation of the Seebeck coefficient with pressure for TiCoSb. A small (approximately 6%) increase in the absolute value of the Seebeck coefficient is observed over the pressure range studied. This implies a very small effect on the thermoelectric efficiency of this material.

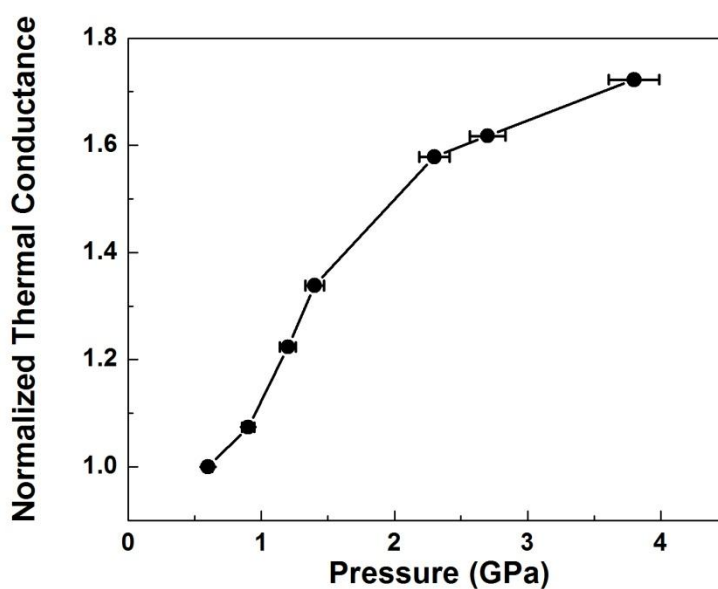


Figure 70. TiCoSb – Normalized Thermal Conductivity vs Pressure

The normalized thermal conductivity (normalized to the lowest pressure value) as a function of temperature is plotted for TiCoSb. A generally increasing trend is observed as pressure is increased for this material. However, the rate of increase is larger between 0.6 GPa to 2.3 GPa (60% increase) than the increase between 2.3 GPa to 4.0 GPa (15% increase).

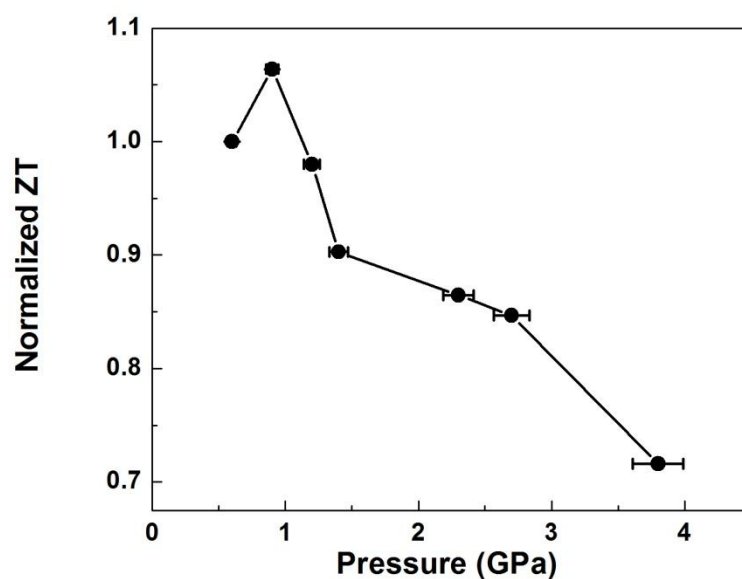


Figure 71. TiCoSb – Normalized ZT vs Pressure

Plot of the normalized dimensionless figure of merit ZT as a function of pressure for TiCoSb. A small increase at very low pressures is observed and after this initial increase, there is a steady decrease until the highest pressure obtained. The overall decrease in the TE efficiency is 30% for the TiCoSb sample.

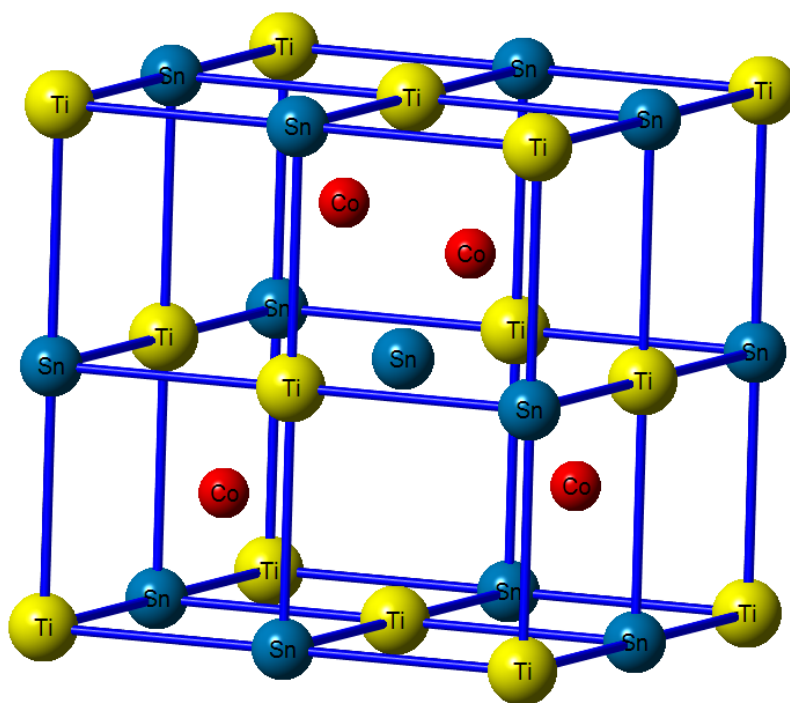


Figure 72. TiNiSn – Ambient Crystal Structure

The MgAgAs ambient pressure and temperature structure of TiNiSn.

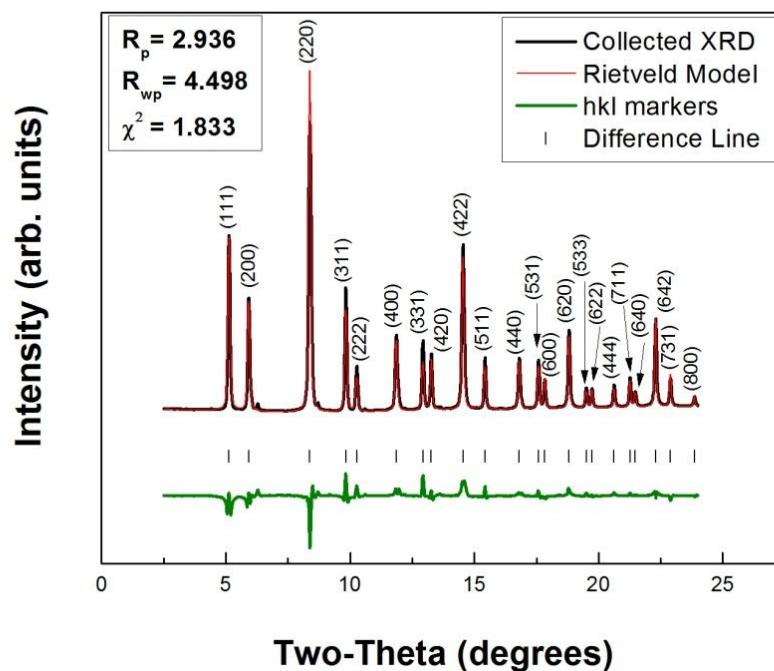


Figure 73. TiNiSn – Ambient XRD Spectrum

Ambient pressure and temperature X-ray diffraction pattern of TiNiSn. A Rietveld refinement (red line) was performed to model the collected data (solid black line) which has been indexed to the MgAgAs structure with reflections shown as solid black lines under the XRD pattern. The green solid line at the bottom indicates the difference between the Rietveld refinement and the collected data. The quality factors R_p , R_{wp} , and χ^2 are presented as well.

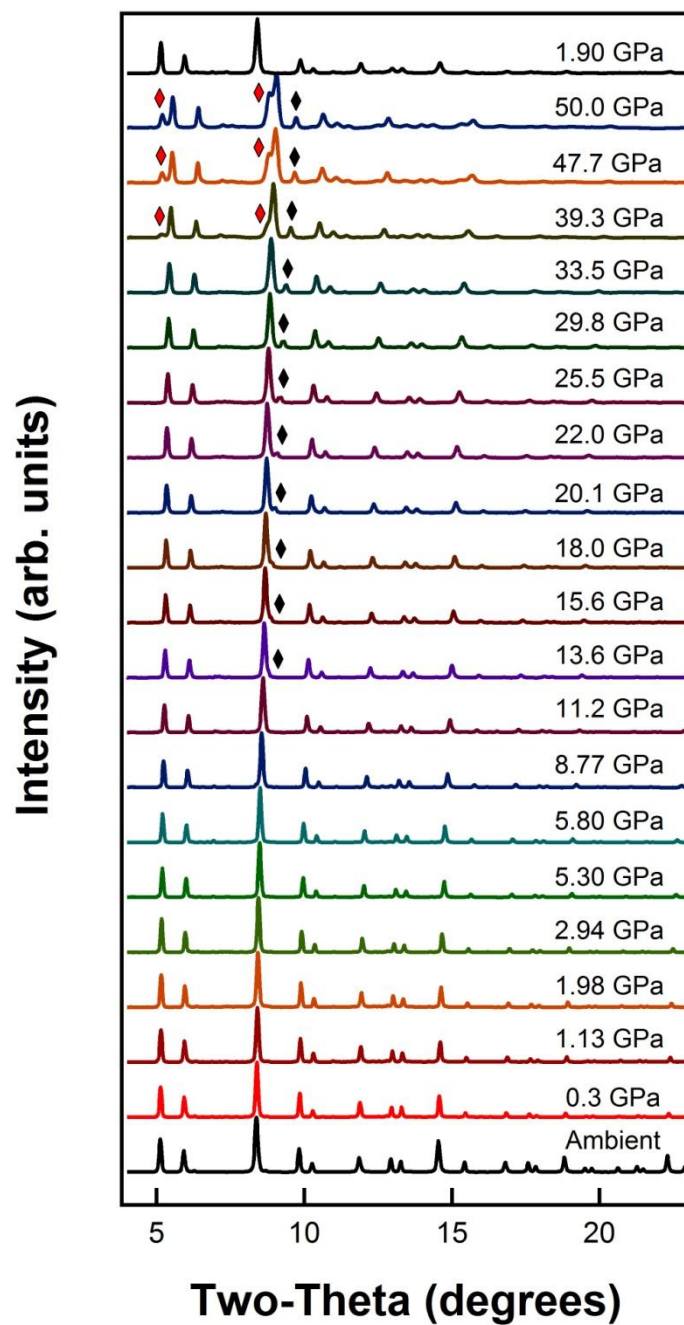


Figure 74. TiNiSn – XRD Spectra vs Pressure

The evolution of XRD patterns as pressure increases for TiNiSn. Black diamonds represent XRD peaks from the Ne pressure-transmitting medium. Red diamonds represent the appearance of new peaks corresponding to a high-pressure structural phase transition.

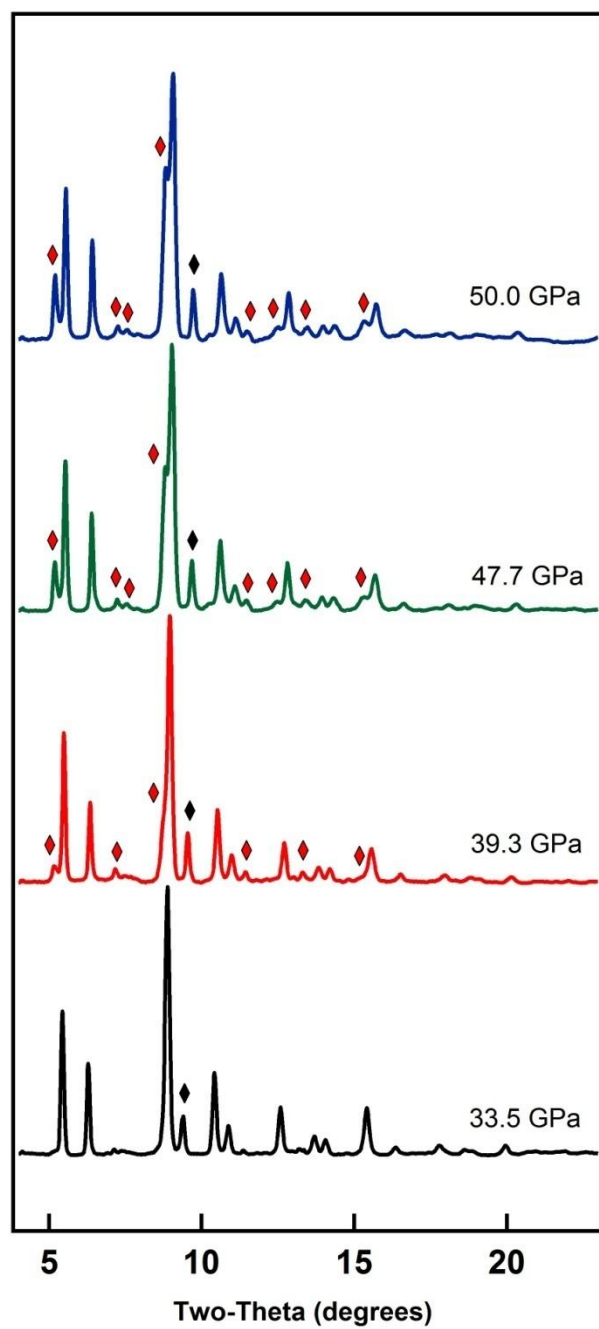


Figure 75. TiNiSn – XRD Spectra vs Pressure: High-Pressure Phase

Selected XRD patterns corresponding to the pressure-induced structural phase transition.

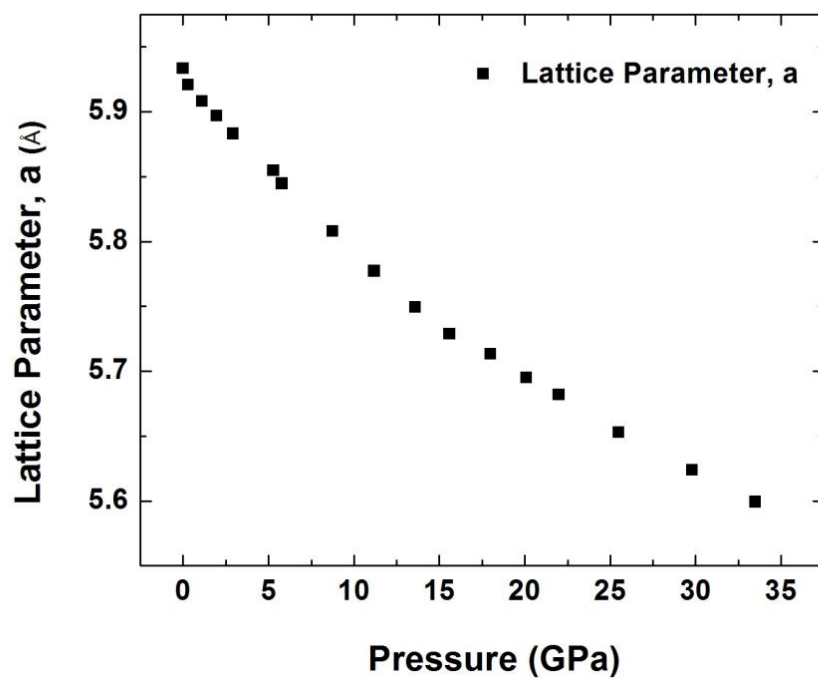


Figure 76. TiNiSn – Lattice Parameter vs Pressure

Plot of the lattice parameter, a , for TiNiSn as a function of increasing pressure.

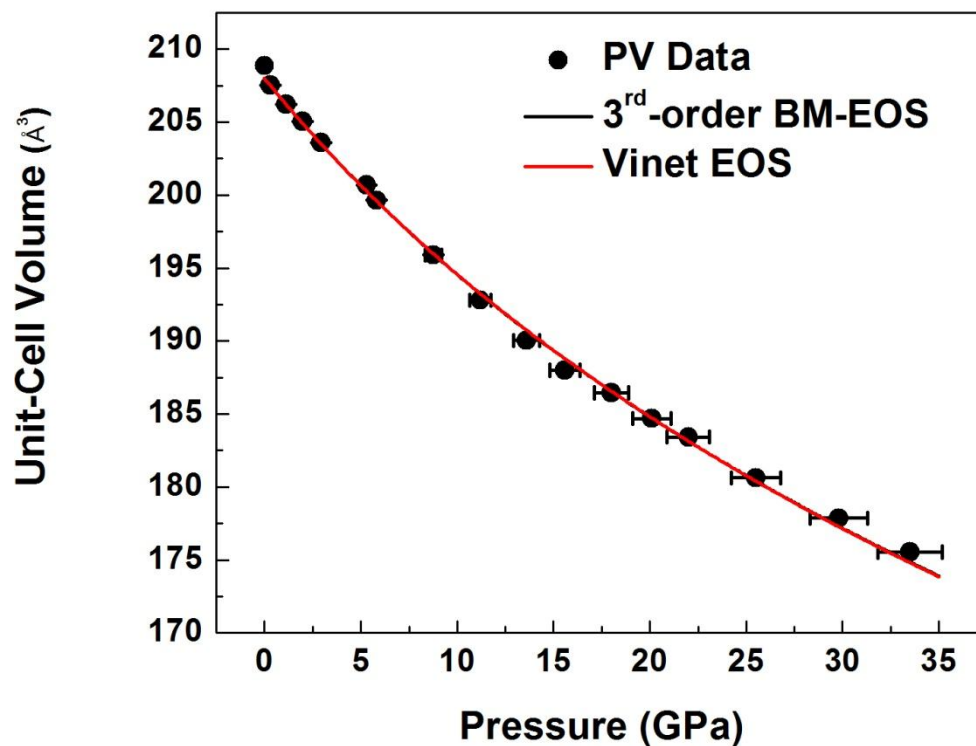


Figure 77. TiNiSn – Unit Cell Volume vs Pressure

Plot of the unit-cell volume as a function of increasing pressure. The solid black circles represent the collected TiNiSn data and the black and red lines represent the 3rd order Birch-Murnaghan and Vinet equation of state fits to the collected data.



Figure 78. TiNiSn – Radiography Images

Series of radiography images to visualize the sample thickness decreasing as pressure is increased for TiNiSn. The radiography images are taken at the edge of the sample.

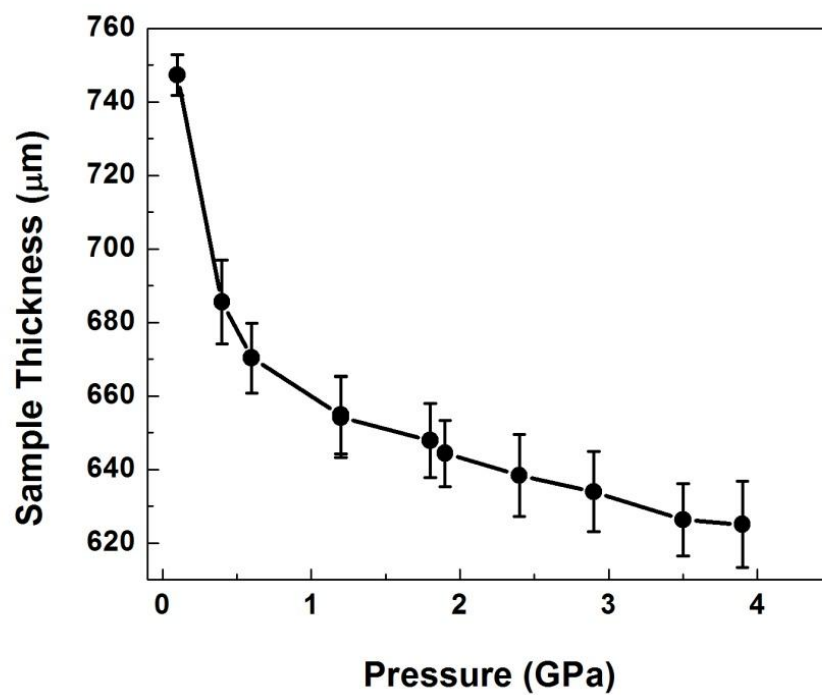


Figure 79. TiNiSn – Sample Thickness vs Pressure

Sample thickness variation with increasing pressure for TiNiSn sample

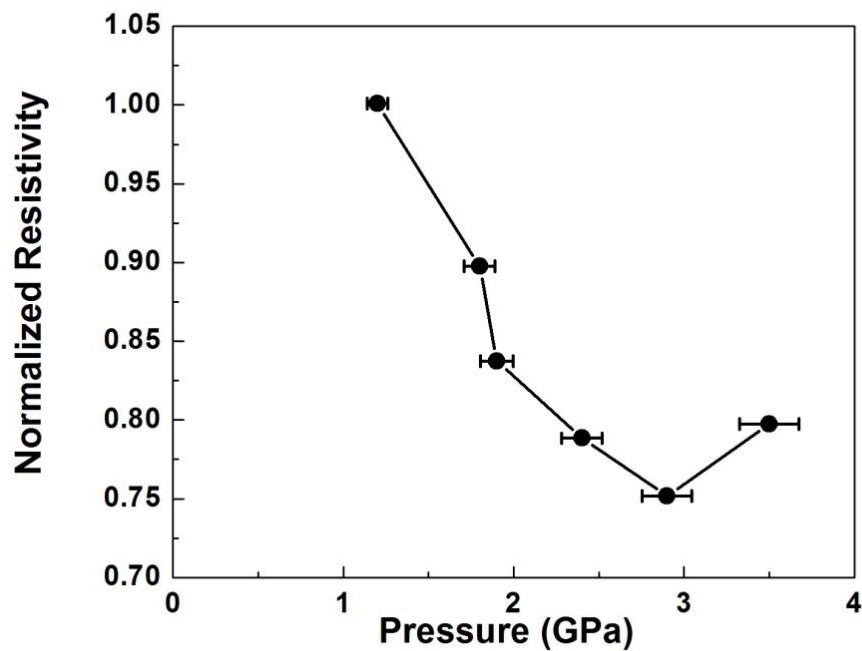


Figure 80. TiNiSn – Normalized Electrical Resistivity vs Pressure

A plot of the normalized electrical resistivity (normalized to the lowest pressure value) as a function of increasing pressure. An increase of 25% is observed from 1 to 3 GPa with a small upturn of 5% being observed as the pressure is increased further to 3.5 GPa.

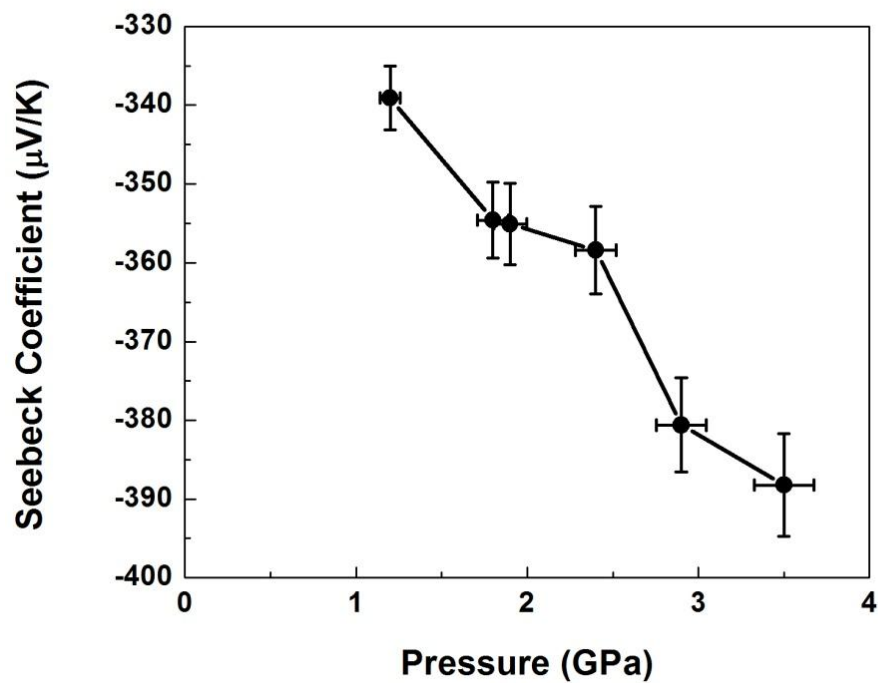


Figure 81. TiNiSn – Seebeck Coefficient vs Pressure

The variation of the Seebeck coefficient as a function of increasing pressure for TiNiSn. An overall increase of 13% in the absolute value of the Seebeck coefficient is observed over the pressure range from 1 to 3.5 GPa.

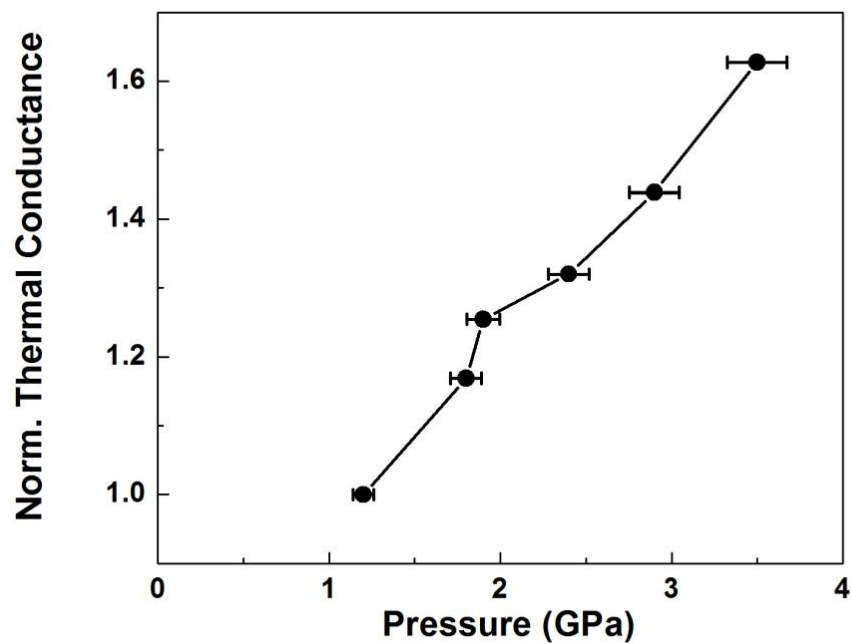


Figure 82. TiNiSn – Normalized Thermal Conductivity vs Pressure

The thermal conductivity normalized to the lowest pressure value is plotted as a function of increase pressure from 1 GPa to 3.5 GPa. There is an overall 60% increase in the thermal conductivity observed for the TiNiSn sample.

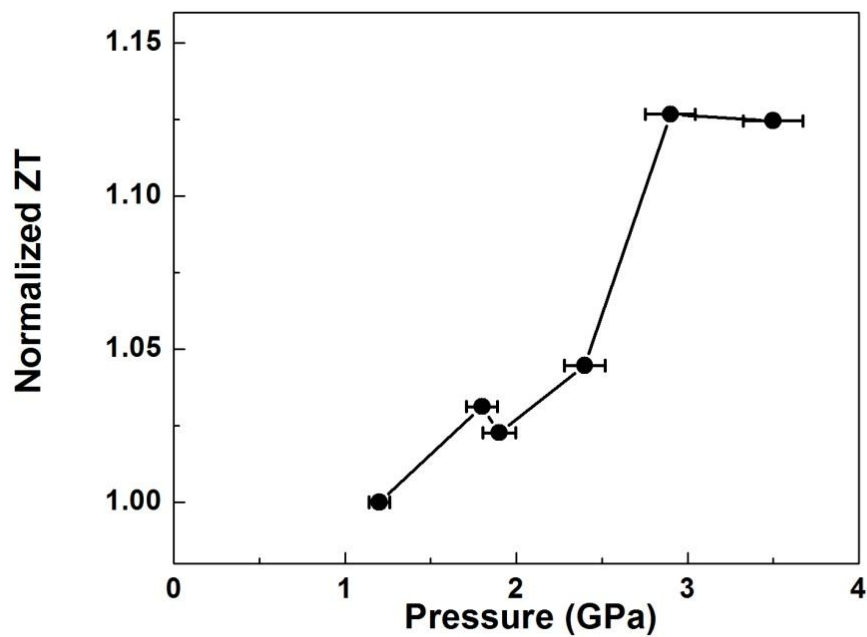


Figure 83. TiNiSn – Normalized ZT vs Pressure

The dimensionless figure of merit ZT is plotted as a normalized value as a function of increasing pressure for TiNiSn. An increase of almost 15% is observed over the pressure range from 1 to 3.0 GPa with a plateau seemingly observed above 3.0 GPa.

Appendix B – Tables

Table 1. PbTe – Raw Thermoelectric Data

Example raw data from PbTe experiment with small temperature increase indicated by the Power increase from 2 – 8 W and pressure increase from 3800 psi to 9,500 psi.

P (Psi)	Power (W)	Ch1-Ch2 (V)	Al1-Al2 (V)	R (Ohms)	T1 (K)	T2 (K)
3809	2	2.25E-04	8.93E-05	1.77E-01	309.2	306.2
3806	5	6.89E-04	3.17E-04	2.11E-01	322.9	314.2
3805	8	1.20E-03	6.08E-04	2.53E-01	336.9	322.9
4500	8	1.18E-03	6.09E-04	2.13E-01	337.0	323.3
4950	8	1.14E-03	5.90E-04	1.82E-01	336.1	322.8
5493	8	1.08E-03	5.54E-04	1.65E-01	335.6	322.4
6000	8	1.04E-03	5.17E-04	1.47E-01	334.8	322.4
7507	8	9.20E-04	4.49E-04	1.16E-01	333.0	321.6
8000	8	8.83E-04	4.12E-04	0.107979	332.8	321.5
9000	8	8.00E-04	3.55E-04	9.34E-02	331.7	321.1
9500	8	7.66E-04	3.39E-04	8.86E-02	331.4	320.8

Table 2. PbTe – Calculated Thermoelectric Data

Example calculated thermoelectric quantities from collected raw data for PbTe from 2.1 GPa to 5.3 GPa.

P (GPa)	Power (W)	Δx (μm)	ΔT (K)	Avg T (K)	R (ohms)	ρ (ohm - m)	α ($\mu V/K$)	κ (W/mK)	ZT
2.1	8	562	14	330	0.224	1.25E-03	-60.1	12.8	7.46E-05
2.5	8	571	14	330	0.185	1.02E-03	-61.8	13.3	9.31E-05
2.8	8	563	13	329	0.155	8.67E-04	-61.4	13.5	1.06E-04
3.1	8	556	13	329	0.138	7.80E-04	-60.7	13.4	1.16E-04
3.4	8	553	12	329	0.121	6.89E-04	-58.2	14.2	1.14E-04
4.2	8	538	11	327	0.092	5.35E-04	-56.9	15.0	1.32E-04
4.5	8	532	11	327	0.084	4.96E-04	-53.8	15.0	1.27E-04
5.0	8	530	11	326	0.071	4.23E-04	-50.7	15.9	1.24E-04
5.3	8	530	11	326	0.067	3.97E-04	-50.5	15.9	1.32E-04

Table 3. $\text{Sn}_{1-x}\text{Mn}_x\text{Te}$ ($x = 12\%$) – Unit Cell Parameters, Volume, and Pressure Data

Unit-cell parameters, **a**, **b**, and **c**, unit-cell volume, **V**, and pressure data-set for $\text{Sn}_{1-x}\text{Mn}_x\text{Te}$ ($x = 12\%$) for the ambient pressure *Fm-3m* and high-pressure *Pnma* phases.

Pressure (GPa)	a (Å)	b (Å)	c (Å)	Unit-Cell Volume (Å ³)
<i>Fm-3m Phase</i>				
0.32	6.2388	6.2388	6.2388	242.8
0.92	6.2064	6.2064	6.2064	239.1
1.79	6.1679	6.1679	6.1679	234.6
2.77	6.1356	6.1356	6.1356	231.0
3.74	6.0939	6.0939	6.0939	226.3
4.90	6.0639	6.0639	6.0639	223.0
<i>Pnma Phase</i>				
6.92	8.045	4.182	6.154	207.0
8.40	7.912	4.199	6.126	203.5
10.4	7.834	4.163	6.081	198.3
11.9	7.810	4.151	6.052	196.2
13.9	7.738	4.127	6.010	191.9
16.6	7.710	4.088	5.973	188.3
19.1	7.664	4.054	5.942	184.6
22.3	7.593	4.024	5.896	180.1
25.0	7.522	4.007	5.865	176.8
28.3	7.471	3.971	5.816	172.5
30.7	7.414	3.966	5.785	170.1

Table 4. $\text{Sn}_{1-x}\text{Mn}_x\text{Te}$ ($x = 12\%$) – 2nd-order BM-EOS Fit Parameters

Equation of state parameters for the 2nd-order Birch-Murnaghan EOS for $\text{Sn}_{1-x}\text{Mn}_x\text{Te}$ ($x = 12\%$).

Values inside the parenthesis are error on the last digit as determined by fit.

Birch-Murnaghan Equation of State		
<i>Fm-3m Phase</i>		
V₀	B₀	B'₀
244 (4)	48 (6)	4 (fixed)
Birch-Murnaghan Equation of State		
<i>Pnma Phase</i>		
V₀	B₀	B'₀
228 (3)	59 (5)	4 (fixed)

Table 5. TiCoSb – Unit Cell Parameters, Volume, and Pressure Data

Unit-cell parameter, **a**, unit-cell volume, **V**, and pressure data-set for TiCoSb in MgAgAs crystal phase.

Pressure (GPa)	a = b = c (Å)	Unit-Cell Volume (Å³)
1.7	5.8586	201.09
2.6	5.8465	199.84
3.9	5.8304	198.20
5.9	5.8101	196.13
7.7	5.7958	194.69
9.8	5.7814	193.24
12.2	5.7603	191.13
16.2	5.7357	188.69
18.6	5.7261	187.75
20.6	5.7154	186.70
22.9	5.6997	185.16
25.3	5.6814	183.39
27.3	5.6692	182.21
29.8	5.6628	181.59
35.3	5.6316	178.61
37.7	5.6090	176.46
42.0	5.5992	175.54
46.8	5.5802	173.76
58.0	5.5425	170.26
61.6	5.5251	168.66
67.7	5.4991	166.56
90	5.4330	160.37
95	5.4283	159.95
97	5.4209	159.30
115	5.3658	154.49

Table 6. TiCoSb – 3rd-order BM-EOS Fit Parameters

Equation of state parameters for the 3rd-order Birch-Murnaghan EOS and Rose-Vinet EOS for TiCoSb. Values inside the parenthesis are error on the last digit.

Birch-Murnaghan Equation of State		
V₀ (Å³)	B₀ (GPa)	B'₀
203 (8)	166 (6)	7.8(5)
Vinet Equation of State		
V₀ (Å³)	B₀ (GPa)	B'₀
203 (2)	168 (6)	7.5 (4)

Table 7. TiNiSn – Unit Cell Parameters, Volume, and Pressure Data

Unit-cell parameter, **a**, unit-cell volume, **V**, and pressure data-set for TiNiSn in MgAgAs crystal phase.

Pressure (GPa)	a = b = c (Å)	Unit-Cell Volume (Å³)
0	5.9332	208.9
0.3	5.9205	207.5
1.1	5.9079	206.2
2.0	5.8968	205.0
2.9	5.8829	203.6
5.3	5.8547	200.7
5.8	5.8445	199.6
8.8	5.8078	195.9
11.2	5.777	192.8
13.6	5.7493	190.0
15.6	5.7286	188.0
18.0	5.713	186.5
20.1	5.6948	184.7
22.0	5.6817	183.4
25.5	5.6528	180.6
29.8	5.6238	177.9
33.5	5.5992	175.5

Table 8. TiNiSn – 3rd-order BM-EOS Fit Parameters

Equation of state parameters for the 3rd-order Birch-Murnaghan EOS and Rose-Vinet EOS for TiNiSn. Values inside the parenthesis are error on the last digit.

Birch-Murnaghan Equation of State		
V₀ (Å³)	B₀ (GPa)	B'₀
208 (1)	128 (4)	4.7 (6)
Vinet Equation of State		
V₀ (Å³)	B₀ (GPa)	B'₀
208 (1)	128 (4)	4.8 (6)

References

- [1] Seebeck, T.J. "Magnetic polarization of metals and minerals." *Abhandlungen der Deutschen Akademie der Wissenschaften zu Berlin*, (1822-1823):265.
- [2] Peltier, J.C.. Nouvelles experience sur la caloricite des courans electrique. *Ann. Chim.*, LV1 (1834):371.
- [3] U.S. Department of Energy. *Waste Heat Recovery: Technology and Opportunities in U.S. Industry*. Industrial Technologies Program. By BCS, Incorporated. March 2008.
- [4] Rowe, D.M. *CRC Handbook of Thermoelectrics*. CRC Press, Inc, 1995.
- [5] Yang, J. "Automotive applications of thermoelectric materials." *J. Elec. Mater.* **38** (2009):1245.
- [6] O'Dwyer, C., Chen, R., He, Jr-H., Lee, J., Razeeb, K.M. "Scientific and Technical Challenges in Thermal Transport and Thermoelectric Materials and Devices." *ECS J. Solid State Sci. Technol.*, **6.3** (2017):N3058.
- [7] Zhang, X., Zhao, L-D. "Thermoelectric Materials: Energy Conversion Between Heat and Electricity." *J. Materiomics* **1** (2015):92.
- [8] Twaha, S., Zhu J., Yan, Y., Li, B. "A Comprehensive Review of Thermoelectric Technology: Materials, Applications, Modelling, and Performance Improvement." *Renew. Sust. Energ. Rev.*, **65** (2016):698.
- [9] Nozariasbmarz, A., Agarwal, A., Coutant, Z.A., Hall, M.J., Liu, J., Liu, R., Malhotra, A., Norouzzadeh, P., Öztürk, M.C., Ramesh, V.P., Sargolzaeiaval, Y., Suarez, F., Vashae, D. "Thermoelectric Silicides: A Review." *Jpn. J. Appl. Phys.*, **56** (2017):05DA04.
- [10] Kanatzidis, M.G. "Nanostructured Thermoelectrics: The New Paradigm." *Chem. Mater.*, **22** (2010):648.
- [11] Heremans, J.P., Dresselhaus, M.S., Bell, L.E., Morelli, D.T. "When Thermoelectrics Reached the Nanoscale." *Nat. Nanotechnol.*, **8** (2013):471.
- [12] Franz, R., Wiedemann, G. "Ueber die Wärme-Leitungsfähigkeit der Metalle." *Annalen der Physik*, **165**. 8 (1853):497.
- [13] Heremans, J.P., Jovovic, V., Toberer, E.S., Saramat, A., Kurosaki, K., Charoenphakdee, A., Yamanaka, S., Snyder, G.F. "Enhancement of Thermoelectric Efficiency in PbTe by Distortion of the Electronic Density of States." *Science*, **321.5888** (2008):554.
- [14] Heremans, J.P., Wiendlocha, B., Chamoire, A.M. "Resonant Levels in Bulk Thermoelectric Semiconductors." *Energy Environ. Sci.* **5** (2012):5510.
- [15] Pei, Y.Z., Shi, X.Y., Lalonde, A., Wang, H., Chen, L.D., Snyder, G.J. "Convergence of Electronic Bands for High Performance Bulk Thermoelectrics." *Nature*, **473** (2011):414.

- [16] Liu, W., Tan, X.J., Yin, K., Liu, H.J., Tang, X.F., Shi, J., Zhang, Q., Uher, C. "Convergence of Conduction Bands as a Means of Enhancing Thermoelectric Performance of n-Type $\text{Mg}_2\text{Si}_{1-x}\text{Sn}_x$ Solid Solutions." *Phys. Rev. Lett.* **108** (2012):166601.
- [17] Hicks, L.D., Dresselhaus, M.S. "Effect of Quantum-Well Structures on the Thermoelectric Figure of Merit." *Phys. Rev. B*, **47** (1993):12727.
- [18] Hicks, L.D., Dresselhaus, M.S. "Thermoelectric Figure of Merit of a One-Dimensional Conductor." *Phys. Rev. B*, **47** (1993):16631.
- [19] Hsu, K.F., Loo, S., Guo, F., Chen, W., Dyck, J.S., Uher, C., Hogan, T., Polychroniadis, E.K., Kanatzidis, M.G. "Cubic $\text{AgPb}_m\text{SbTe}_{2+m}$: Bulk Thermoelectric Materials with High Figure of Merit." *Science*, **303** (2014):818.
- [20] Biswas, K., He, J.Q., Blum, I.D., Wu, C.I., Hogan, T.P., Seidman, D.N., Dravid, V.P., Kanatzidis, M.G. "High-Performance Bulk Thermoelectrics with All-Scale Hierarchical Architectures." *Nature*, **489** (2012):414.
- [21] Zhao, L.D., He, J.Q., Hao, S.Q., Wu, C.I., Hogan, T.P., Wolverton, C., Dravid, V.P., Kanatzidis, M.G. "Raising the Thermoelectric Performance of p-Type PbS with Endotaxial Nanostructuring and Valence-Band Offset Engineering Using CdS and ZnS." *J. Am. Chem. Soc.*, **134**, **39** (2012):16237.
- [21] Biswas, K., He, J., Zhang, Q., Wang, G., Uher, C., Dravid, V.P., Kanatzidis, M.G. "Strained Endotaxial Nanostructures with High Thermoelectric Figure of Merit." *Nat. Chem.*, **3** (2011):160.
- [22] Morelli, D.T., Jovovic, V., Heremans, J.P. "Intrinsically Minimal Thermal Conductivity in Cubic I-V-VI(2) Semiconductors." *Phys. Rev. Lett.*, **101** (2008):035901.
- [23] Kurosaki, K., Kosuga, A., Muta, H., Uno, M., Yamanaka, S. "Ag₉TlTe₅: A High Performance Thermoelectric Bulk Material with Extremely Low Thermal Conductivity." *Appl. Phys. Lett.*, **87** (2005):061919.
- [24] Zhao, L.D., Berardan, D., Pei, Y.L., Byl, C., Pinsard-Gaudart, L., Dragoie, N. " $\text{Bi}_{1-x}\text{Sr}_x\text{CuSeO}$ Oxyselenides as Promising Thermoelectric Materials." *Appl. Phys. Lett.*, **97** (2010):092118.
- [25] Hicks, L.D., Harman, T.C., Sun, X., Dresselhaus, M.S. "Experimental Study of the Effect of the Quantum Well Structures on the Thermoelectric." *Phys. Rev. B*, **53** (1996):R10493
- [26] Ohta, H., Kim, S., Mune, Y., Mizoguchi, T., Nomura, K., Ohta, S., Nomura, T., Nakanishi, Y., Ikuhara, Y., Hirano, M., Hosono, H., Koumoto, K. "Giant Thermoelectric Seebeck Coefficient of a Two-Dimensional Electron Gas in SrTiO_3 " *Nat. Mater.*, **6** (2007):129.
- [27] Zhang, Q., Liao, B.L., Lan, Y.C., Lukas, K., Liu, W.S., Esfarjani, K., Opeil, C., Broido, D., Chen, G., Ren, Z.F. "High Thermoelectric Performance by Resonant Dopant Indium in Nanostructured SnTe." *Proc. Natl. Acad. Sci.*, **110** (2013):13261.

- [28] Zhao, L.D., Wu, H.J., Hao, S.Q., Wu, C.I., Zhou, X.Y., Biswas, K., He, J.Q., Hogan, T.P., Uher, C., Wolverton, C., Dravid, V.P., Kanatzidis, M.G. "All-Scale Hierarchical Thermoelectrics: MgTe in PbTe Facilitates Valence Band Convergence and Suppresses Bipolar Thermal Transport for High Performance." *Energy Environ. Sci.*, **6** (2013):3346.
- [29] Pei, Y.Z., Wang, H., Gibbs, Z.M., Lalonde, A.D., Snyder, G.J. "Thermopower Enhancement in $\text{Pb}_{1-x}\text{Mn}_x\text{Te}$ Alloys and Its Effect on Thermoelectric Efficiency." *Npg. Asia Mater.*, **4.9** (2012):e28.
- [30] Moon, J., Kim, J.H., Chen, Z.C.Y., Xiang, J., Chen, R.K. "Gate-Modulated Thermoelectric Power Factor of Hole Gas in Ge-Si Core-Shell Nanowires." *Nano. Lett.*, **13.3** (2013):1196.
- [31] Pei, Y.L., He, J., Li, J.F., Li, F., Liu, Q., Pan, W., Barreateau, C., Berardan, D., Dragoe, N., Zhao, L.D. "High Thermoelectric Performance of Oxyselenides: Intrinsically Low Thermal Conductivity of Ca-Doped BiCuSeO." *NPG Asia Mater.*, **5** (2013):e47.
- [32] Hu, L.P., Zhu, T.J., Liu, X.H., Zhao, X.B. "Point Defect Engineering of High Performance Bismuth-Telluride-Based Thermoelectric Materials." *Adv. Funct. Mater.*, **24** (2014):5211.
- [33] Jiang, G.Y., He, J., Zhu, T.J., Fu, C.G., Liu, X.H., Hu, L.P., Zhao, X. "High Performance $\text{Mg}_2(\text{Si}, \text{Sn})$ Solid Solutions: A Point Defect Chemistry Approach to Enhancing Thermoelectric Properties." *Adv. Funct. Mater.*, **24** (2014):3776.
- [34] Zhao, L.D., Zhang, B.P., Li, J.F., Zhou, M., Liu, W.S., Liu, J. "Thermoelectric and Mechanical Properties of Nano-SiC-Dispersed Bi_2Te_3 Fabricated by Mechanical Alloying and Spark Plasma Sintering." *J. Alloy Compd.*, **455** (2008):259.
- [35] Xiong, Z., Chen, X.H., Zhao, X.Y., Bai, S.Q., Huang, X.Y., Chen, L.D. "Effect of Nano TiO_2 Dispersion on the Thermoelectric Properties of Filled Skutterudite $\text{Ba}_{0.22}\text{Co}_4\text{Sb}_{12}$." *Solid State Sci.*, **11** (2009):1612.
- [36] Zhao, X.Y., Shi, X., Chen, L.D., Zhang, W.Q., Bai, S.Q., Pei, Y.Z., Li, X.Y. "Synthesis of $\text{Yb}_y\text{Co}_4\text{Sb}_{12}/\text{Yb}_2\text{O}_3$ Composites and Their Thermoelectric Properties." *Appl. Phys. Lett.* **89** (2006):092121.
- [37] Tan, G.J., Zhao, L.D., Shi, F.Y., Doak, J.W., Lo, S.H., Sun, H., Wolverton, C., Dravid, V.P., Uher, C., Kanatzidis, M.G. "High Thermoelectric Performance of p-Type SnTe via a Synergistic Band Engineering and Nanostructuring Approach." *J. Am. Chem. Soc.*, **136** (2014):7006.
- [38] Lee, Y., Lo, S.H., Androulakis, J., Wu, C.I., Zhao, L.D., Chung, D.Y., Hogan, T.P., Dravid, V.P., Kanatzidis, M.G. "High-Performance Tellurium-Free Thermoelectrics: All Scale Hierarchical Structuring of p-Type PbSe-MSe Systems ($\text{M} = \text{Ca}, \text{Sr}, \text{Ba}$)." *J. Am. Chem. Soc.*, **135.13** (2013):5152.

- [39] Zhao, L.D., He, J.Q., Wu, C.I., Hogan, T.P., Zhou, X., Uher, C., Dravid, V.P., Kanatzidis, M.G. "Thermoelectrics with Earth Abundant Elements: High Performance p Type PbS Nanostructured with SrS and CaS." *J. Am. Chem. Soc.*, **134**.18 (2012):7902.
- [40] Zhao, L.D., Lo, S.H., Zhang, Y., Sun, H., Tan, G., Uher, C., Wolverton, C., Dravid, V.P. Kanatzidis, M.G. "Ultralow Thermal Conductivity and High Thermoelectric Figure of Merit in SnSe Crystals." *Nature*, **508** (2014):373.
- [41] Payne, D.J., Egdel, R.G., Walsh, A., Watson, G.W., Guo, J., Glans, P.A., Learmonth, T. Smith, K.E. "Electronic Origins of Structural Distortions in Post-Transition Metal Oxides: Experimental and Theoretical Evidence for a Revision of the Lone Pair Model." *Phys. Rev. Lett.*, **96** (2006):157403.
- [42] Brown, S.R., Kauzlarich, S.M., Gascoin, F., Snyder, G.J. "Yb₁₄MnSb₁₁: New High Efficiency Thermoelectric Material for Power Generation." *Chem. Mater.*, **18** (2006): 1873.
- [43] Chiritescu, C., Cahill, D.G., Nguyen, N., Johnson, D., Bodapati, A., Keblinski, P., Zshack, P. "Ultralow Thermal Conductivity in Disordered, Layered WSe₂ Crystals." *Science*, **315** (2007):351.
- [44] Liu, H., Shi, X., Xu, F., Zhang, L., Zhang, W., Chen, L., Li, Q., Uher, C., Day, T., Snyder, J., "Copper Ion Liquid-Like Thermoelectrics." *Nat. Mater.*, **11** (2012):422.
- [45] Yo, B., Liu, W., Chen, S., Wang, H., Wang, H., Chen, G., Ren, Z. "Thermoelectric Properties of Copper Selenide with Ordered Selenium Layer and Disordered Copper Layer." *Nano Energy*, **1** (2012):472.
- [46] Parker, D., Singh, D.J. "First Principles Investigations of the Thermoelectric Behavior of Tin Sulfide." *J. Appl. Phys.*, **108** (2010):083712.
- [47] Tan, Q., Zhao, L.D., Li, J.F., Wu, C.F., Wei, T.R., Xing, Z.B., Kanatzidis, M.G., "Thermoelectrics with Earth Abundant Elements: Low Thermal Conductivity and High Thermopower in Doped SnS." *J. Mater. Chem. A*, **2** (2014):17302.
- [48] Badding, J.V., Meng, J.F., Polvani, D.A. "Pressure Tuning in the Search for New and Improved Solid State Materials." *Chem. Mater.*, **10** (1998):2889.
- [49] Disalvo, F.J. "Thermoelectric Cooling and Power Generation." *Science*, **285** (1999):703.
- [50] Bridgman, P.W. "The Resistance of 72 Elements, Alloys and Compounds to 100,000\ Kg/Cm²." *Proc. Am. Acad. Arts Sci.*, **81** (1952):165.
- [51] Bridgman, P.W. "The Effect of Pressure on the Thermal Conductivity of Metals." *Proc. Am. Acad. Arts Sci.*, **57** (1922):75.
- [52] Errandonea, D., Segura, A., Manjón, F.J., Chevy, A., Machado, E., Tobias, G., Ordejón, P., Canadell, E. "Crystal Symmetry and Pressure Effects on the Valence Band Structure of γ InSe and ϵ -GaSe: Transport Measurements and Electronic Structure Calculations." *Phys. Rev. B*, **71** (2005):125206.

- [53] Errandonea, D., Segura, A., Martínez-García, D., Muñoz-San Jose, V. “Hall-Effect and Resistivity Measurements in CdTe and ZnTe at High Pressure: Electronic Structure of Impurities in the Zinc-Blende Phase and the Semimetallic to Metallic Character of the High-Pressure Phases.” *Phys. Rev. B*, **79**, 125203 (2009).
- [54] Errandonea, D., Segura, A., Sánchez-Royo, J.F., Mun-Atoz, V., Grima, P., Chevy, A., Ulrich, C. “Investigation of Conduction-Band Structure, Electron-Scattering Mechanisms, and Phase Transitions in Indium Selenide by Means of Transport Measurements Under Pressure. *Phys. Rev. B*, **55** (1997):16217.
- [55] Shchennikov, V.V., Ovsannikov, S.V., Bazhenov, A.V. “A Composite High-Pressure Cell with Sintered Diamond Insets for Study of Thermoelectric and Thermomagnetic Properties in a Range up to 30 GPa: Application to Pr and PbTe.” *J. Phys. Chem. Solids*, **69** (2008):2315.
- [56] Ovsyannikov, S.V., Shchennikov, V.V. “Phase Transitions Investigation in ZnTe by Thermoelectric Power Measurements at High Pressure.” *Solid State Commun.*, **132** (2004):333.
- [57] Ovsyannikov, S.V., Shchennikov, V.V., Todo, S., Uwatoko, Y. “Transport Properties of Fe₃O₄ Magnetite at High Pressure up to 24 GPa: A Search for Crossovers.” *High Press. Res.*, **28** (2008):601.
- [58] Ovsyannikov, S.V., Shchennikov, V.V., Todo, S., Uwatoko, Y. “A New Crossover in Fe₃O₄ Magnetite Under Pressure Near 6 GPa: Modification to ‘Ideal’ Inverse Cubic Spinel.” *J. Condens. Matter*, **20** (2008):172201.
- [59] Ke, F., Yang, J., Liu, C., Wang, Q., Liu, Y., Zhang, J., Wu, L., Zhang, X., Han, Y., Wu, B., Ma, Y., Gao, C. “High-Pressure Electrical-Transport Properties of SnS: Experimental and Theoretical Approaches.” *J. Phys. Chem. C*, **117** (2013):6033.
- [60] McWilliams, R.S., Konôpková, Z., Goncharov, A.F. “A Flash Heating Method for Measuring Thermal Conductivity at High Pressure and Temperature: Application to Pt.” *Phys. Earth Planet. Inter.*, **247** (2015):17.
- [61] Konôpková, Z., McWilliams, R.S., Gómez-Pérez, N., Goncharov, A.F. “Direct Measurement of Thermal Conductivity in Solid Iron at Planetary Core Conditions. *Nature* **534**.7605 (2016):99.
- [62] Jacobsen, M.K., Liu, W., Li, B. “Measurement Setup for the Simultaneous Determination of Diffusivity and Seebeck Coefficient in a Multi-Anvil Apparatus.” *Rev. Sci. Instrum.*, **83** (2012):093903.
- [63] Yuan, B., Tao, Q., Zhao, X., Cao, K., Cui, T., Wang, X., Zhu, P. “In Situ Measurement of Electrical Resistivity and Seebeck Coefficient Simultaneously at High Temperature and High Pressure.” *Rev. Sci. Instrum.*, **85**.1 (2014):013904.
- [64] Li, B., Kung, J., Liebermann, R. “Modern Techniques in Measuring Elasticity of Earth Materials at High Pressure and High Temperature Using Ultrasonic Interferometry in

- Conjunction with Synchrotron X-Radiation in Multi-Anvil Apparatus.” *Phys. Earth Planet. Inter.*, **143-144** (2004):559.
- [65] Li, B., Jackson, I., Gasparik, T., Liebermann, R. “Elastic Wave Velocity Measurement in Multi-Anvil Apparatus to 10 GPa Using Ultrasonic Interferometry.” *Phys. Earth Planet. Inter.*, **98** (1996):79.
 - [66] Li, B., Liebermann, R. “Indoor Seismology by Probing the Earth’s Interior by Using Sound Velocity Measurements at High Pressure and Temperatures.” *Proc. Natl. Acad. Sci.*, **104** (2007):9145.
 - [67] Matityahu, S., Emuna, M., Yahel, E., Makov, G., Greenberg, Y. “Novel Experimental Design for High Pressure – High Temperature Electrical Resistance Measurements in a ‘Paris-Edinburgh’ Large Volume Press.” *Rev. Sci. Instrum.*, **86** (2015):043902.
 - [68] Besson, J.M., Nelmes, R.J., Hamel, G., Loveday, J.S., Weill, G., Hull, S. “Neutron Powder Diffraction Above 10 GPa.” *Physica B*, **180** (1992):907.
 - [69] Kono, Y., Park, C., Sakamaki, T., Kenney-Benson, C., Shen, G., Wang, Y. “Simultaneous Structure and Elastic Wave Velocity Measurement of SiO₂ Glass at High Pressures and High Temperatures in a Paris-Edinburgh Cell.” *Rev. Sci. Instrum.*, **83** (2012):033905.
 - [70] Kono, Y., Park, C., Kenny-Benson, C., Shen, G., Wang, Y. “Toward Comprehensive Studies of Liquids at High Pressures and High Temperatures: Combined Structure, Elastic Wave Velocity, and Viscosity Measurements in the Paris-Edinburgh Cell.” *Phys. Earth Planet. Inter.*, **228** (2014):269.
 - [71] Morard, G., Mezouar, M., Rey, N., Poloni, R., Merlen, A., Le Floch, S., Toulemonde, P., Pascarelli, S., San-Miguel, A., Sanloup, C., Fiquet, G. “Optimization of Paris-Edinburgh Press Cell Assemblies for In-Situ Monochromatic X-ray Diffraction and X-ray Absorption.” *High. Press. Res.*, **27** (2007):223.
 - [72] Nieto-Sanz, D., Loubeyre, P., Crichton, W., Mezouar, M. “X-ray Study of the Synthesis of Boron Oxides at High Pressure: Phase Diagram and Equation of State.” *Phys. Rev. B*, **70** (2004):214108.
 - [73] Yamada, A., Wang, Y., Inoue, T., Yang, W., Park, C., Yu, T., Shen, G. “High-Pressure X-ray Diffraction Studies on the Structure of Liquid Silicate Using a Paris-Edinburgh Type Large Volume Press.” *Rev. Sci. Instrum.*, **82** (2011):015103.
 - [74] Kono, Y., Irifune, T., Higo, Y., Inoue, T., Barnhoorn, A. “P-V-T Relation of MgO Derived by Simultaneous Elastic Wave Velocity and In-Situ X-ray Measurements: A New Pressure Scale for the Mantle Transition Region.” *Phys. Earth Planet. Inter.*, **183** (2010):196.
 - [75] Baker, J., Kumar, R., Velisavljevic, N., Park, C., Kenney-Benson, C., Kono, Y., Cornelius, A., Zhao, Y. “In-Situ X-Ray Diffraction, Electrical Resistivity, and Thermal

- Measurements Using a Paris-Edinburgh Cell at HPCAT 16BM-B Beamline.” *J. Phys. C*, **500** (2014):142003.
- [76] Baker, J., Kumar, R., Park, C., Kenney-Benson, C., Cornelius, A., Velisavljevic, N. “High-Pressure Seebeck Coefficients and Thermoelectric Behaviors of Bi and PbTe Measured Using a Paris-Edinburgh Cell.” *J. Synchrotron Rad.*, **23** (2016):1368.
- [77] Granta Design Limited. (2017, June) Zirconia – ZrO₂, Zirconium Dioxide. <http://www.azom.com/properties.aspx?ArticleID=133>.
- [78] Polvani, D., Meng, J., Hasegawa, M., Badding, J. “Measurement Setup for the Simultaneous Determination of Diffusivity and Seebeck Coefficient in a Multi-Anvil Apparatus.” *Rev. Sci. Instrum.* **70** (1999):3586.
- [79] Bundy, F. P. “Pressure Dependence of the EMF of Thermocouples.” *J. Appl. Phys.* **32** (1961):483.
- [80] Nishihara, Y., Fuke, K., Tange, Y., Higo, Y. “Determination of Pressure Effect on Thermocouple Electromotive Force Using Multi-Anvil Apparatus.” *High. Press. Res.* **36** (2016):121.
- [81] “Diamond Anvil Cells.” High Pressure Science and Engineering Center, University of Nevada, Las Vegas. <https://hipsecweb.files.wordpress.com/2014/11/mao-typesymmetric-dac-232x166.jpg>.
- [82] “Diamond Anvil Cell.” *Wikipedia: The Free Encyclopedia*. Wikimedia Foundation, Inc. 12 May 2012. https://en.wikipedia.org/wiki/Diamond_anvil_cell.
- [83] Jayaraman, A. “Diamond Anvil Cell and High-Pressure Physical Investigations.” *Rev. Mod. Phys.*, **55** (1983):65.
- [84] Rivers, M., Prakapenka, V.B., Kubo, A., Pullins, C., Holl, C.M., Jacobsen, S.D. “The COMPRES/GSECARS Gas-Loading System for Diamond Anvil Cells at the Advanced Photon Source.” *High Press. Res.*, **28** (2008):273.
- [85] Mao, H.K., Xu, J., Bell, P.M. “Calibration of the Ruby Pressure Gauge to 800 kbar Under Quasi-Hydrostatic Conditions.” *J. Geophys. Res.*, **91** (1986):4673.
- [86] Chijioke, A.D., Nellis, W.J., Soldatov, A., Silvera, I.F. “The ruby pressure standard to 150 GPa.” *J. Appl. Phys.* **98** (2005):114905.
- [87] “Bragg’s Law.” *Wikipedia: The Free Encyclopedia*. Wikimedia Foundation, Inc. 10 April 2009. https://en.wikipedia.org/wiki/Bragg%27s_law.
- [88] McMahon, M.I. “Diamonds on Diamond: Structural Studies at Extreme Conditions on the Diamond Light Source.” *Phil. Trans. R. Soc. A*, **373** (2015):20130158.
- [89] Hammersley, A.P., Svensson, S.O., Hanfland, M., Fitch, A.N., Häusermann, D. “Two-Dimensional Detector Software: From Real Detector to Idealised Image or Two-Theta Scan.” *High Press. Res.*, **14** (1996):235.

- [90] Prescher, C., Prakapenka, V.B. "Dioptas: A Program for Reduction of Two-Dimensional X-Ray Diffraction Data and Data Exploration." *High Press. Res.*, **35** (2015):223.
- [91] Howard, C.J., Hunter, B.A. "A Computer Program for Rietveld Analysis of X-Ray and Neutron Powder Diffraction Patterns." Lucas Height Research Laboratories (unpublished) (1988).
- [92] Materials Data Incorporated, 1224 Concannon Blvd., Livermore, California 94550, USA.
- [93] Chaikin, P.M., Lubensky, T.C. *Principles of Condensed Matter Physics*. Cambridge: Press Syndicate of the University of Cambridge, 1995. Print.
- [94] Birch, F. "The Effect of Pressure Upon the Elastic Parameters of Isotropic Solids, According to Murnaghan's Theory of Finite Strain." *J. Appl. Phys.* **9** (1938):279.
- [95] Vinet, P., Smith, J.R., Ferrante, J., Rose, J.H. "Temperature Effects on the Universal Equation of State of Solids." *Phys. Rev. B*, **35** (1987):1945.
- [96] Chen, J.H., Iwasaki, H., Kikegawa, T. "Structural Study of the High-Pressure High Temperature Phase of Bismuth Using High Energy Synchrotron Radiation." *J. Phys. Chem. Solids*, **58** (1997):247.
- [97] Bundy, F.P. "Phase Diagram of Bismuth to 130,000 kg/cm², 500 °C." *Phys. Rev.*, **110.2** (1958):314.
- [98] Reichlin, R. "Electrical Resistance Measurements of Metals to 40 GPa in the Diamond Cell." *J. de Physique*, **45** (1984):C8-399.
- [99] Ferdin, B.T., Jaya, N., Anbukumaran, K., Natarajan, S. "Measurement of Thermoelectric Power Using Metal Opposed Anvil Cells Up to 100 kbar." *Rev. Sci. Instrum.*, **66** (1995):5636.
- [100] Chandrasekhar, B.S. "The Seebeck Coefficient of Bismuth Single Crystals." *J. Phys Chem. Solids*, **11** (1959):268.
- [101] Ovsyannikov, S.V., Shchennikov, V.V. "Pressure-Tuned Colossal Improvement of Thermoelectric Efficiency of PbTe." *Appl. Phys. Lett.*, **90** (2007):122103.
- [102] Kafalas, J.A., Brebrick, R.F., Strauss, A.J. "Evidence That SnTe is a Semiconductor." *Appl. Phys. Lett.*, **4** (1964):93.
- [103] Kafalas, J.A. "High-Pressure Phase Transition in Tin Telluride." *Science*, **143** (1964):952.
- [104] Littlewood, P.B. "The Crystal Structure of IV-VI Compounds. I. Classification and Description." *J. Phys. C: Solid St. Phys.*, **13** (1980):4855.
- [105] Kapitanov, E.V., Yakovlev, E.N. "Mössbauer Study of Phase Transitions Under High Hydrostatic Pressures. I. The Phase Transition of Mg₂Sn." *Phys. Stat. Sol (a)*, **53.2** (1979):473.

- [106] Zhou, D., Li, Q., Ma, Y., Cui, Q., Chen, C. "Unraveling Convolved Structural Transitions in SnTe at High Pressure." *J. Phys. Chem. C*, **117** (2013):5352.
- [107] Johnsen, S., He, J., Androulakis, J., Dravid, V., Todorov, I., Chung, D.Y., Kanatzidis, M. "Nanostructures Boost the Thermoelectric Performance of PbS." *J. Am. Chem. Soc.*, **133** (2011):3460.
- [108] Androulakis, J., Todorov, I., He, J., Chung, D.Y., Dravid, V., Kanatzidis, M. "Thermoelectrics from Abundant Chemical Elements: High-Performance Nanostructured PbSe-PbS." *J. Am. Chem. Soc.*, **133** (2011):10920.
- [109] Sitter, H., Lischka, K., Heinrich, H. "Structure of the Second Valence Band in PbTe." *Phys. Rev. B*, **16.2** (1977):680.
- [110] Rogers, L.M. "Valence Band Structure of SnTe." *J. Phys. D: Appl. Phys.*, **1** (1968):845.
- [111] Littlewood, P.B., Mihaila, B., Schulze, R.K., Safarik, D.J., Gubernatis, J.E., Bostwick, E., Rotenberg, C., Opeil, C.P., Durakiewicz, T., Smith, J.L., Lashley, J.C. "Band Structure of SnTe Studied by Photoemission Spectroscopy." *Phys. Rev. Lett.* **105** (2010):086404.
- [112] Brebrick, R.F. "Deviations from Stoichiometry and Electrical Properties in SnTe." *J. Phys. Chem. Solids*, **24** (1963):27.
- [113] Zhang, L., Wang, J., Cheng, Z., Sun, Q., Li, Z., Dou, S. "Lead-Free SnTe-Based Thermoelectrics: Enhancement of Thermoelectric Performance by Doping with Gd/Ag." *J. Mater. Chem. A*, **4** (2016):7936.
- [114] Tan, G., Shi, F., Hao, S., Chi, H., Bailey, T., Zhao, L., Uher, C., Wolverton, C., Dravid, V., Kanatzidis, M. "Valence Band Modification and High Thermoelectric Performance in SnTe Heavily Alloyed with MnTe." *J. Am. Chem. Soc.*, **137** (2015):11507.
- [115] Tan, G., Shi, F., Doak, J.W., Sun, H., Zhao, L-D., Wang, P., Uher, C., Wolverton, C., Dravid, V.P., Kanatzidis, M.G. "Extraordinary Role of Hg in Enhancing the Thermoelectric Performance of p-Type SnTe." *Energy Environ. Sci.*, **8** (2015):267.
- [116] Tan, G., Shi, F., Hao, S., Chi, H., Zhao, L-D., Uher, C., Wolverton, C., Dravid, V.P., Kanatzidis, M.G. "Codoping in SnTe: Enhancement of Thermoelectric Performance through Synergy of Resonance Levels and Band Convergence." *J. Am. Chem. Soc.*, **137** (2015):5100.
- [117] Tan, G., Shi, F., Sun, H., Zhao, L-D., Uher, C., Dravid, V.P., Kanatzidis, M.G. "SnTe-AgBiTe₂ as an Efficient Thermoelectric Material with Low Thermal Conductivity." *J. Mater. Chem. A*, **2** (2014):20849.
- [118] Tan, G., Shi, F., Hao, S., Chi, H., Bailey, T.P., Zhao, L.D., Uher, C., Wolverton, C., Dravid, V.P., Kanatzidis, M.G. "Valence Band Modification and High Thermoelectric Performance in SnTe Heavily Alloyed with MnTe." *J. Am. Chem. Soc.*, **137** (2015):11507.

- [119] Zhao, L-D., Hao, S., Lo, S.H., Wu, C.I., Zhou, X., Lee, Y., Li, H., Biswas, K., Hogan, T.P., Uher, C., Wolverton, C., Dravid, V.P., Kanatzidis, M.G. "High Thermoelectric Performance via Hierarchical Compositionally Alloyed Nanostructures." *J. Am. Chem. Soc.*, **135** (2013):7364.
- [120] Rogl, G., Grytsiv, A., Failamani, F., Hohenhofer, M., Bauer, E., Rogl, P. "Attempts to Further Enhance ZT in Skutterdites via Nano-Composites." *J. Alloys Compd.* **695** (2017):682.
- [121] Shi, X., Yang, J., Salvador, J., Chi, M., Cho, J.Y., Wang, H., Bai, S., Yang, J., Zhang, W., Chen, L. "Multiple-Filled Skutterudites: High Thermoelectric Figure of Merit through Separately Optimizing Electrical and Thermal Transports." *J. Am. Chem. Soc.*, **133.20** (2011):7837.
- [122] Pei, Y., Shi, X., LaLonde, A., Wang, H., Chen, L., Snyder, G.J. "Convergence of Electronic Bands for High Performance Bulk Thermoelectrics." *Nature*, **473** (2011):66.
- [123] Pei, Y-L., Liu, Y. "Electrical and Thermal Transport Properties of Pb-Based Chalcogenides: PbTe, PbSe, and PbS." *Journal of Alloys and Compounds*, **514** (2012):40.
- [124] Xu, L., Wang, H-Q., Zheng, J-C. "Thermoelectric Properties of PbTe, SnTe, and GeTe at High Pressure: an *Ab Initio* Study." *J. Electron. Mater.*, **40.5** (2011):641.
- [125] Huang, L., Zhang, Q., Yuan, B., Lai, X., Yan, X., Ren, Z. "Recent Progress in Half-Heusler Thermoelectric Materials." *Materials Research Bulletin*, **76** (2016):107.
- [126] Poon, S.J., Wu, D., Zhu, S., Xie, W., Tritt, T.M., Thomas, P., Venkatasubramanian, R. "Half-Heusler Phases and Nanocomposites as Emerging High-ZT Thermoelectric Materials." *J. Mater. Res.*, **26** (2011):2795.
- [127] Liu, W.S., Yan, X., Chen, G., Ren, Z.F. "Recent Advances in Thermoelectric Nanocomposites." *Nano Energy* **1** (2012):42.
- [128] Xie, W., Weidenkaff, A., Tang, X.F., Zhang, Q.J., Poon, J., Tritt, T.M. "Recent Advances in Nanostructured Thermoelectric Half-Heusler Compounds." *Nanomaterials* **2** (2012):379.
- [129] Chen, S., Ren, Z.F. "Recent Progress of Half-Heusler for Moderate Temperature Thermoelectric Applications." *Mater. Today*, **16.10** (2013):387.
- [130] Tobola, J., Pierre, J., Kaprayk, S., Skolozdra, R.V., Kouacou, M.A. "Crossover from Semiconductor to Magnetic Metal in Semi-Heusler Phases as a Function of Valence Electron Concentration." *J. Phys.: Condens. Matter*, **10** (1998):1013.
- [131] Aliev, F.G., Brandt, N.B., Moshchalkov, V.V., Kozyrkov, V.V., Skolozdra, R.V., Belogorokhov, A.I. "Gap at the Fermi Level in the Intermetallic Vacancy System RBiSn (Ti, Zr, Hf)." *Z. Phys. B* **75** (1989):167.
- [132] Aliev, F.G. "Gap at Fermi Level in Some New d- and f-Electron Intermetallic Compounds." *Physica B* **171** (1991):199.

- [133] Kuentzler, R., Clad, R., Schmerber, G., Dossmann, Y. "Gap at Fermi Level and Magnetism in RMSn Ternary Compounds (R = Ti, Zr, Hf and M = Fe, Co, Ni)." *J. Magn. Mater.* **104–107** (1992):1976.
- [134] Lue, C.S., Kuo, Y.K. "Thermoelectric Properties of the Semimetallic Heusler Compounds $\text{Fe}_{2-x}\text{V}_{1+x}\text{M}$ (M = Al, Ga)." *Phys. Rev. B* **66** (2002):085121.
- [135] Cook, B.A., Harringa, J.L., Tan, Z.S., Jesser, W.A., *Proceedings of the 15th International Conference on Thermoelectrics*, (1996):122.
- [136] Culp, S.R., Simonson, J.W., Poon, S.J., Ponnabalam, V., Edwards, J., Tritt, T.M. "Nanostructure Model of Thermal Conductivity for High Thermoelectric Performance." *Appl. Phys. Lett.*, **93** (2008):022105.
- [137] Culp, S.R., Poon, S.J., Hickman, N., Tritt, T.M., Blumm, J. "Effect of Substitutions on the Thermoelectric Figure of Merit of Half-Heusler Phases at 800 °C." *Appl. Phys. Lett.*, **88** (2006):042106.
- [138] Zhou, M., Feng, C., Chen, L., Huang, X. "Effects of Partial Substitution of Co by Ni on the High-Temperature Thermoelectric Properties of TiCoSb-Based Half-Heusler Compounds." *J. Alloys Compds.*, **391** (2005):194.
- [139] Sekimoto, T., Kurosaki, K., Muta, H., Yamanaka, S. "Thermoelectric Properties of Sn-Doped TiCoSb Half-Heusler Compounds." *J. Alloys Compds.*, **407** (2006):326.
- [140] Xia, Y., Ponnambalam, V., Bhattacharya, S., Pope, A.L., Poon, S.J., Tritt, T.M. "Electrical Transport Properties of TiCoSb Half-Heusler Phases That Exhibit High Resistivity." *J. Phys: Condens. Matter*, **13** (2001):77.
- [141] Wang, L.L., Miao, L., Wang, Z.Y., Wei, W., Xiong, R., Liu, H.J., Shi, J., Tang, X.F. "Thermoelectric Performance of Half-Heusler Compounds TiNiSn and TiCoSb." *J. Appl. Phys.*, **105** (2009):013709.
- [142] Kawaharada, Y., Kurosaki, K., Muta, H., Uno, M., Yamanaka, S. "High Temperature Thermoelectric Properties of CoTiSb Half-Heusler Compounds." *J. Alloys Compds.*, **384** (2004):308.
- [143] Xu, B., Zhang, J., Li, X.F., Yu, G.Q., Ma, S.S., Wang, Y.S., Yi, L. "Electronic Structure and Assessment of Thermoelectric Performance of TiCoSb." *Materials Research Innovations*, **18** (2014):104.
- [144] Jeitschko, W. "Transition Metal Stannides with MgAgAs and MnCu₂Al Type Structure." *Metall. Trans. A* **1** (1970):3159.
- [145] Webster, P., Ziebeck, J. "Magnetic and Chemical Order in Heusler Alloys Containing Cobalt and Titanium." *J. Phys. Chem. Solids*, **34** (1973):1647.
- [146] Stadnyk, Y., Gorelenko, Y., Tkachuk, A., Goryn, A., Davydov, V., Bodak, O. "Electric Transport and Magnetic Properties of $\text{TiCo}_{1-x}\text{Ni}_x\text{Sb}$ Solid Solution." *J. Alloys. Compds.*, **329** (2001):37.

- [147] Bhattacharya, S., Pope, A.L., Littleton IV, R.T., Tritt, T.M. "Effect of Sb Doping on the Thermoelectric Properties of Ti-Based Half-Heusler Compounds, $\text{TiNiSn}_{1-x}\text{Sb}_x$." *Appl. Phys Lett.*, **77.16** (2006):2476.
- [148] Sakurada, S., Shutoh, N. "Effect of Ti Substitution on the Thermoelectric Properties of (Zr,Hf)NiSn Half-Heusler Compounds." *Appl. Phys. Lett.*, **86** (2005):082105.
- [149] Uher, C., Yang, J., Morelli, D.T., Mesiner, G.P. "Transport Properties of Pure and Doped MNiSn ($\text{M}=\text{Zr}, \text{Hf}$)." *Phys. Rev. B*, **59.13** (1999):8615.
- [150] Hohl, H., Ramirez, A.P., Goldmann, C., Ernst, G., Wölfling, B., Bucher, E. "Efficient Dopants for ZrNiSn -Based Thermoelectric Materials." *J. Phys: Condens. Matter*, **11** (1999):1697.
- [151] Kurosaki, K., Maekawa, T., Muta, H., Yamanaka, S. "Effect of Spark Plasma Sintering Temperature on Thermoelectric Properties of (Ti,Zr,Hf)NiSn Half-Heusler Compounds." *J. Alloys Compds.*, **397** (2005):296.
- [152] Hermet, P., Niedziolka, K., Jund, P. "A First-Principles Investigation of the Thermodynamic and Mechanical Properties of Ni-Ti-Sn Heusler and Half-Heusler Materials." *RSC Adv.*, **3** (2013):22176.
- [153] Hohl, H., Ramirez, A.P., Kaefer, W., Fess, K., Thurner, Ch., Kloc, Ch., Bucher, E. "A New Class of Materials with Promising Thermoelectric Properties: MNiSn ($\text{M} = \text{Ti}, \text{Zr}, \text{Hf}$)." *Mater. Res. Soc. Symp. Proc.*, **478** (1997):109.
- [154] Hemley, R.J., Zha, C.S., Jephcoat, A.P., Mao, H.K., Finger, L.W., Cox, D.E. "X-Ray Diffraction and Equation of State of Solid Neon to 110 GPa." *Phys. Rev B*, **39** (1989):11820.

Curriculum Vitae

Jason Baker
University of Nevada, Las Vegas
Department of Physics & Astronomy
4505 S. Maryland Parkway
Las Vegas, NV 89154
(702) – 469 – 7860
bakerj@physics.unlv.edu

Education

University of Nevada, Las Vegas
B.S., Physics, 2008
M.S., Physics, 2012

Internships & Workshops

1. **Internship – Los Alamos National Laboratory,** Summer 2012
2. **Workshop – HPCAT PEC Workshop,** May 2013
3. **Pre-Doctoral Student – Argonne National Laboratory HPCAT,** June 2014

Awards

1. Malcolm F. Nicol Fellowship, 2012 – 2013.
2. “Outstanding Poster Award.” SSAP Symposium, April 2017.

Oral Presentations

1. *In-Situ X-ray Diffraction, Electrical Resistivity, and Thermal Conductivity Measurements Using a Paris-Edinburgh Cell.* **SCCM & AIRAPT**, Seattle, WA, July 2013
2. *High-Pressure Thermoelectric Measurements Using a Paris-Edinburgh Cell.* **APS March Meeting**, Baltimore, MD, March 2016.
3. *High-Pressure Instrumentation: Thermal and Structural Properties of Half-Heusler Compounds.* **SMEC**, Eastern Caribbean, April 2017. **Invited**

Poster Presentations

1. *Thermal and Electrical Measurements Using Custom Cell Assembly in Paris-Edinburgh Cell.* **PEC Workshop**, Argonne National Laboratory, APS, HPCAT May 2013.

2. *High-Pressure Structural, Electrical, and Thermal Measurements of Thermoelectric Compounds. SSAP Symposium*, Sante Fe, NM March 2015.
3. *High-Pressure Seebeck Coefficient and Thermal Property Measurements on Thermoelectrics. SSAP Symposium*, Baltimore, MD February 2016.
4. *High-Pressure Thermoelectric and Structural Behavior of Half-Heusler Compounds. SSAP Symposium*, Chicago, IL, April 2017.

Publications

1. *High-pressure Seebeck coefficients and thermoelectric behaviors of Bi and PbTe measured using a Paris-Edinburgh cell.* **Baker, J.**, Kumar, R., Park, C., Kenney-Benson, C., Cornelius, A. & Velisavljevic, N. *J. Synchrotron Rad.* **23**, 1368-1378, (2016).
2. *Pressure induced structural transitions in CuSbS₂ and CuSbSe₂ thermoelectric compounds.* **Jason Baker**, Ravhi Kumar, Daniel Sneed, Anthony Connolly, Yi Zhang, Nenad Velisavljevic, Jayalakshmi Paladugu, Michael Pravica, Changfeng Chen, Andrew Cornelius, Yusheng Zhao *Journal of Alloys and Compounds* **643**, 186 - 194, (2015).
3. *High pressure transport and structural studies on Nb₃Ga superconductor.* Vahe Mkrtcheyan, Ravhi Kumar, **Jason Baker**, Anthony Connolly, Daniel Antonio, Andrew Cornelius, Yusheng Zhao *Physica B: Condensed Matter* **459**, 21 - 23, (2015).
4. *In-situ x-ray diffraction, electrical resistivity and thermal measurements using a Paris-Edinburgh cell at HPCAT 16BM-B beamline.* **Jason Baker**, Ravhi Kumar, Nenad Velisavljevic, Changyong Park, Curtis Kenney-Benson, Yoshio Kono, Andrew Cornelius, Yusheng Zhao *Journal of Physics: Conference Series* **500**, 142003, (2014).
5. *Effect of pressure and temperature on structural stability of MoS₂.* Nirup Bandaru, Ravhi Kumar, Daniel Sneed, Oliver Tschauner, **Jason Baker**, Daniel Antonio, Sheng-Nian Luo, Thomas Hartmann, Yusheng Zhao, Rama Venkat *Journal of Physical Chemistry C* **118** (6), 3230- 3235, (2014).
6. *Structural stability of WS₂ under high pressure.* Nirup, Bandaru, Ravhi Kumar, **Jason Baker**, Oliver Tschauner, Thomas Hartmann, Yusheng Zhao, Rama Venkat *International Journal of Modern Physics B* **28** (25), 1450168, (2014).
7. *Pressure induced high spin - low spin transition in FeSe superconductor studied by x-ray emission spectroscopy and ab initio calculations.* Ravhi S. Kumar, Yi Zhang, Yuming Xiao, **Jason Baker**, Andrew Cornelius, Sathishkumar Veeramalai, Paul Chow, Changfeng Chen, Yusheng Zhao *Applied Physics Letters* **99**, 061913, (2011).